

1998

# Measurements and modeling of the effects of an orthogonal bias field on properties of isotropic magnetic materials

Ying Bi

*Iowa State University*

Follow this and additional works at: <https://lib.dr.iastate.edu/rtd>

 Part of the [Electrical and Electronics Commons](#), [Electromagnetics and Photonics Commons](#), and the [Physics Commons](#)

## Recommended Citation

Bi, Ying, "Measurements and modeling of the effects of an orthogonal bias field on properties of isotropic magnetic materials " (1998). *Retrospective Theses and Dissertations*. 12191.  
<https://lib.dr.iastate.edu/rtd/12191>

This Dissertation is brought to you for free and open access by the Iowa State University Capstones, Theses and Dissertations at Iowa State University Digital Repository. It has been accepted for inclusion in Retrospective Theses and Dissertations by an authorized administrator of Iowa State University Digital Repository. For more information, please contact [digirep@iastate.edu](mailto:digirep@iastate.edu).

## INFORMATION TO USERS

This manuscript has been reproduced from the microfilm master. UMI films the text directly from the original or copy submitted. Thus, some thesis and dissertation copies are in typewriter face, while others may be from any type of computer printer.

**The quality of this reproduction is dependent upon the quality of the copy submitted.** Broken or indistinct print, colored or poor quality illustrations and photographs, print bleedthrough, substandard margins, and improper alignment can adversely affect reproduction.

In the unlikely event that the author did not send UMI a complete manuscript and there are missing pages, these will be noted. Also, if unauthorized copyright material had to be removed, a note will indicate the deletion.

Oversize materials (e.g., maps, drawings, charts) are reproduced by sectioning the original, beginning at the upper left-hand corner and continuing from left to right in equal sections with small overlaps. Each original is also photographed in one exposure and is included in reduced form at the back of the book.

Photographs included in the original manuscript have been reproduced xerographically in this copy. Higher quality 6" x 9" black and white photographic prints are available for any photographs or illustrations appearing in this copy for an additional charge. Contact UMI directly to order.

**UMI<sup>®</sup>**

Bell & Howell Information and Learning  
300 North Zeeb Road, Ann Arbor, MI 48106-1346 USA  
800-521-0600



Measurements and modeling of the effects of an orthogonal bias field  
on properties of isotropic magnetic materials

by

Ying Bi

A dissertation submitted to the graduate faculty  
in partial fulfillment of the requirements for the degree of  
DOCTOR OF PHILOSOPHY

Major: Electrical Engineering ( Electromagnetics )

Major Professor: David C. Jiles

Iowa State University

Ames, Iowa

1998

**UMI Number: 9941781**

---

**UMI Microform 9941781**  
**Copyright 1999, by UMI Company. All rights reserved.**

**This microform edition is protected against unauthorized  
copying under Title 17, United States Code.**

---

**UMI**  
**300 North Zeeb Road**  
**Ann Arbor, MI 48103**

**Graduate College  
Iowa State University**

**This is to certify that the Doctoral dissertation of**

**Ying Bi**

**has met the dissertation requirements of Iowa State University**

Signature was redacted for privacy.

**Major Professor**

Signature was redacted for privacy.

**For the Major Program**

Signature was redacted for privacy.

**For the ~~the~~ Graduate College**

## TABLE OF CONTENTS

<b>ACKNOWLEDGMENTS</b>	<b>vi</b>
<b>ABSTRACT</b>	<b>vii</b>
<b>1. GENERAL INTRODUCTION</b>	<b>1</b>
<b>1.1 Hysteresis and magnetization processes</b>	<b>1</b>
1.1.1 Hysteresis of magnetic materials	1
1.1.2 Magnetization process	1
1.1.2.1 Rotation of domains	3
1.1.2.2 Motion of domain walls	4
1.1.2.3 Magnetization of magnetic materials	5
<b>1.2 Development of hysteresis theory</b>	<b>7</b>
<b>1.3 Background</b>	<b>12</b>
<b>1.4 Scope of this thesis</b>	<b>16</b>
<b>2. MEASUREMENTS OF THE ORTHOGONAL FIELD EFFECT</b>	<b>18</b>
<b>2.1 Introduction</b>	<b>18</b>
<b>2.2 Measurements on ferrite plate</b>	<b>19</b>
2.2.1 Specimen and experimental method	19
2.2.2 Results and discussion	21
<b>2.3 Measurements on a ferrite toroid</b>	<b>25</b>
2.3.1 Measurements under large magnetic field	26
2.3.2 Measurements under small magnetic field	30
2.3.3 Measurements at high frequency	34
<b>2.4 Measurements on conducting magnetic materials</b>	<b>36</b>
2.4.1 Measurements on M-190 polycrystalline silicon iron plate	38
2.4.1.1 Specimen characterization and preparation	38
2.4.1.2 Instrumentation	39
2.4.1.3 Results and discussion	40
2.4.2 Measurements on Metglas 2605 amorphous ribbon	42
2.4.2.1 Specimen and experimental method	42
2.4.2.2 Results and discussion	43
<b>2.5 Conclusion</b>	<b>45</b>

<b>3. ANISOTROPIC EXTENSION OF HYSTERESIS MODEL</b>	<b>47</b>
<b>3.1 Introduction</b>	<b>47</b>
<b>3.2 The isotropic hysteresis model</b>	<b>48</b>
3.2.1 An hysteretic magnetization	48
3.2.1.1 Langevin theory of paramagnetism	48
3.2.1.2 Weiss mean field theory	50
3.2.2 Hysteresis magnetization	51
<b>3.3 Extension for the orthogonal field effect</b>	<b>56</b>
3.3.1 Anisotropy induced by an orthogonal field	58
3.3.2 Reversible magnetization at the presence of an orthogonal field	62
<b>3.4 Modeling of experimental results</b>	<b>67</b>
3.4.1 Evaluation of the internal orthogonal bias field	68
3.4.2 Modeling and discussion	70
<b>3.5 Conclusion</b>	<b>74</b>
<b>4. APPLICATIONS OF THE ORTHOGONAL FIELD EFFECT</b>	<b>76</b>
<b>4.1 Introduction</b>	<b>76</b>
<b>4.2 Inductor controlled by an orthogonal field</b>	<b>77</b>
4.2.1 Design of closed circuit device	78
4.2.2 Inductance measurements	79
4.2.3 Hysteresis measurements	81
4.2.4 Conclusion	87
<b>4.3 Inductor controlled by selected saturation</b>	<b>88</b>
4.3.1 Design of a non-gapped power inductor	88
4.3.1.1 Energy storage	89
4.3.1.2 Designed variable inductor	90
4.3.1.3 An assembled rectangular button inductor	92
4.3.2 Inductance measurements of a simulated inductor	93
4.3.3 Hysteresis measurements of the rectangular button inductor	96
<b>4.4 Conclusion</b>	<b>98</b>
<b>5. APPLICATIONS OF FINITE ELEMENT MODELING</b>	<b>100</b>
<b>5.1 Introduction</b>	<b>100</b>
5.1.1 Vector Potential Method	101
5.1.2 Generalized Scalar Potential Method	102
5.1.3 The B-H curve for nonlinear finite element modeling	104
<b>5.2 Distribution and evaluation of field</b>	<b>105</b>
5.2.1 Flux distribution of BEFI	105



5.2.2 The internal orthogonal field along the toroid axis	107
5.2.3 Field distribution in the circular button ferrite inductor	109
5.2.3.1 2D linear simulation	110
5.2.3.2 3D nonlinear simulation	112
5.2.4 Field distribution in the prototype variable inductor	116
<b>5.3 Inductance modeling of variable inductor</b>	<b>118</b>
5.3.1 Modeling of inductance	118
5.3.2 Inductance of the orthogonal mode variable inductor	119
5.3.3 Inductance variation of the testing variable inductor	121
<b>5.4 Conclusion</b>	<b>125</b>
<b>6. GENERAL CONCLUSION</b>	<b>127</b>
<b>APPENDIX</b>	<b>131</b>
<b>REFERENCES</b>	<b>151</b>
<b>VITA</b>	<b>154</b>

## ACKNOWLEDGMENTS

This work was supported by Rockwell Collins, Avionics and Communications Division and the United States National Science Foundation through Iowa State University.

First, I would like to express my sincere appreciation to my major professor Dr. David C. Jiles for his guidance, encouragement, support and patience throughout the course of this work. The results of his professional guidance was far beyond this thesis and will be beneficial to my future. Also, I would like to thank Dr. Basart, Dr. Biner, Dr. Udpa and Dr. Weber for dedicating time to serve on the committee of my program of study.

I would also like to thank Mr. Daniel Jankins, Mr. Brent McDonald and Dr. Jian Sun at Rockwell Collins, Avionics and Communications Division, their support and suggestion gave me lots of help. Many thanks to Dr. Pasquale, Dr. Fiorillo and Dr. Basso of the Istituto Elettrotecnico Nazionale Galileo Ferraris at Turin, Italy for their help during my visit to their institute in June, 1998. Special thanks to all members of Magnetics Group of Ames Laboratory. Their advice, thoughts and friendship through the course of study are very helpful.

I would like to dedicate this dissertation to my grandmother and my parents for their love, dream and encouragement, and to my wife for her support, inspiration and patience.

## ABSTRACT

The research performed in this study involved two areas in magnetics. The first one was the investigation of the orthogonal field effect, its modeling and applications. The results of this research will be presented in this thesis. The second one was the investigation of the nondestructive evaluation of materials using magnetic techniques. The results of this part research will be presented in the appendix in the form of published journal papers.

The effects of the orthogonal bias field were investigated systematically in this study. The measurements on various magnetic materials under different experimental conditions showed that the orthogonal bias field clockwise rotated and reduced the area of hysteresis loop. As a result, permeability, hysteresis loss, coercivity and remanence decreased with increasing orthogonal field. The experimental results showed that the orthogonal field reduced hysteresis loss by increasing the component of reversible domain rotation magnetization.

The Jiles-Atherton hysteresis model developed earlier successfully describes hysteresis of isotropic magnetic materials. In the present study, this one-dimensional isotropic model has been expanded to include anisotropy induced by an orthogonal field. Based on the experimental observation, a dynamically variable reversibility coefficient, which models the change of the reversibility coefficient during the magnetization process and is characterized by the irreversible field range, was proposed to include the reversible domain rotation magnetization in the extended hysteresis model. After incorporating the orthogonal field induced anisotropy and the dynamic reversibility coefficient into the model, the hysteresis loops about the orthogonal field effect showed all experimentally

observed features and were consistent with the results of measurements on a ferrite toroid.

According to measurement results on a circular button ferrite inductor developed in this study, a prototype un-gapped variable ferrite inductor, which utilized selected saturation to increase energy storage and was controlled by an orthogonal current, was proposed in this study. The measurements on an assembled prototype rectangular button ferrite inductor based on the above design confirmed the expected behavior. The measured inductance not only was observed to decrease with increasing orthogonal current, but also with an appropriate orthogonal current the inductance can have only a small fluctuation within a designed excitation current range. The hysteresis measurements showed that the core loss can be reduced to a small value with a strong orthogonal current.

In this study two-dimensional linear FEM modeling was used to evaluate the internal orthogonal field along a toroid axis and flux line distribution of magnetic devices. On the other hand, three-dimensional nonlinear FEM modeling was successfully used to identify saturation regions of variable inductors. The modeled inductance, which was based on nonlinear 3D FEM modeling using ANSYS Parametric Design Language, showed the experimental observed variation under various excitation currents and orthogonal currents.

# 1. GENERAL INTRODUCTION

## 1.1 Hysteresis and magnetization processes

### 1.1.1 Hysteresis of magnetic materials

The response of a material to a magnetic field  $H$  can be described by the magnetization  $M$ , or the magnetic induction  $B$  which is the vector sum of the applied field and the magnetization  $\{B = \mu_0 (H + M)\}$ . For a ferromagnetic material, however, the response depends not only on the applied magnetic field but also the magnetization history of the material. The relationship between the applied magnetic field and the magnetization is not single-valued and determined by the microstructure of the magnetic material. If the magnetic field is removed after magnetization, the magnetization does not go back to zero, instead it keeps a remanent value. In order to make the magnetic induction in the ferromagnetic material zero, a reverse magnetic field has to be applied. This hysteresis behavior of a ferromagnetic material can be well characterized by its hysteresis curve as shown in Figure 1-1, since magnetic properties, such as hysteresis loss, initial permeability, differential permeability, remanence, coercivity, saturation magnetization, of a ferromagnetic material can be extracted from the hysteresis loop.

### 1.1.2 Magnetization process

According to the modern theory of magnetism [1], the atoms of ferromagnetic materials have net non-zero magnetic moments, which result from the orbital motion and spin of electrons in atoms. Due to the mutual interaction among magnetic moments, the magnetic moments of all atoms tend to align parallel to each other. However, the

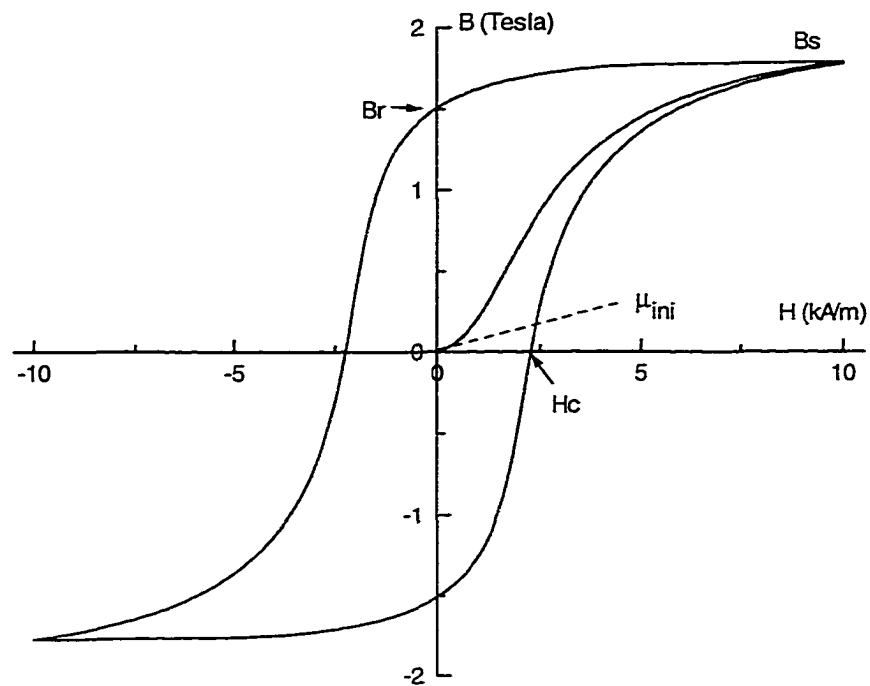


Figure 1-1 A typical hysteresis curve of a ferromagnetic material.

magnetostatic energy tends to randomize this orientation of magnetic moments. As a result, magnetic domains are formed in a magnetic material. Within each domain, which may contain  $10^{12}$  to  $10^{18}$  atoms, the magnetic moments of all atoms are aligned parallel to each other. However, the orientation from domain to domain changes randomly in the demagnetized state and therefore the bulk magnetization of a magnetic material is zero under this condition.

Under the action of a magnetic field, the orientations and sizes of these magnetic domains will change. There are two processes involved. One is the rotation of the domains. The domains which are not in the direction of magnetic field rotate towards the direction of field. Another process is the growth of the domains aligned favorably with respect to the field direction at the expense of the domains aligned unfavorably with respect to the field direction. The interface between two magnetic domains, which is

called the domain wall, will move under the action of a magnetic field. This is known as domain wall motion.

However, the rotation of domains and the motion of domain walls are affected by structural factors, such as anisotropy energy, dislocations, inclusions and second phases, which impede the domain rotation process and domain wall motion process and make the magnetization irreversible. This results in hysteresis.

#### *1.1.2.1 Rotation of domains*

Because of the anisotropy, in zero applied field, the magnetic moments in each domain align along the direction of crystallographic easy axis which corresponds to local energy minimum.

At a low field, the alignment direction of magnetic moments are displaced slightly from the original easy axis direction towards the field direction. This is reversible process and magnetic moments will rotate back to their original directions if the applied field is removed.

At an intermediate field, when the field energy overcomes the anisotropy energy, each magnetic domain rotates from its original easy axis direction towards the field direction, and becomes trapped in an easy axis direction which it last encountered. With increasing magnetic field, magnetic moments will overcome every local anisotropy energy and rotate towards the field direction. They will not rotate back to the original easy axis direction after the field is removed, instead they will align at the last easy axis direction which they had encountered. This part of rotation is irreversible. The larger the

anisotropy energy, the larger external magnetic field energy is needed to overcome the anisotropy energy.

At higher magnetic field strengths, the magnetic moments are rotated further towards the field direction from the easy axis which is closest to the field direction. After removing the magnetic field, the magnetic moments will rotate back to the easy axis closest to the field direction. This is reversible rotation. At a very high field, the angle of precession, which is due to the thermal energy, is reduced. The direction of magnetic moments processes closer to the field direction. This also is a reversible process.

#### *1.1.2.2 Motion of domain walls*

Between two magnetic domains, there is a transition region in which the magnetic moments gradually realign from the direction of one domain to the direction of another domain. The transition layer is called a domain wall, associated with a surface energy which is known as the domain wall energy. Under the action of a magnetic field, because the volume of the domains aligned favorably with respect to the field direction grows at the expense of the domains aligned unfavorably with respect to the field direction, it is as if the interface, the domain wall, moves. The displacement of the domain wall under the action of a magnetic field acts as an elastic membrane under the action of a pressure.

How a domain wall moves is determined by not only the external magnetic field but also domain wall energy and defects in the magnetic material, such as dislocation, grain boundaries, inclusions and voids. Since these defects result in local energy minima when domain walls intersect them, an extra energy is needed for domain walls to



overcome the local energy minimum. When the external magnetic field is removed, the domain wall will rest at the last energy minimum which it has encountered.

If the domain wall energy is very large (compared to the pinning strength), or if the material is free of defects, the domain walls tend to remain planar (because this corresponds to a lower surface energy of domain wall). If the domain wall energy is lower, or the strength of the pinning is stronger, the domain wall tends to bend first under the action of an external magnetic field.

Under the action of a low magnetic field, the high energy domain wall will reversibly translate over a short distance, or the low energy domain wall will reversibly bend first until it encounters another pinning site.

At an intermediate magnetic field, the local energy minimum associated with the pinning site is overcome, the domain wall breaks away from its current pinning site, and moves without further increase of magnetic field, and later becomes pinned by another pinning site. Energy is lost during the irreversible process.

If the magnetic field increases further, the domain wall will continue moving, bending, breaking pinning, pinning, bending, breaking pinning, and so on, until the domain walls move out of the material and the material becomes a single domain. Before becoming a single domain, there are also domain wall coalescence when different domain walls from different domain in the material intersect each other.

### *1.1.2.3 Magnetization of magnetic materials*

Under the action of a magnetic field, however, the magnetization of a magnetic material proceeds by both domain rotation process and domain wall motion process,

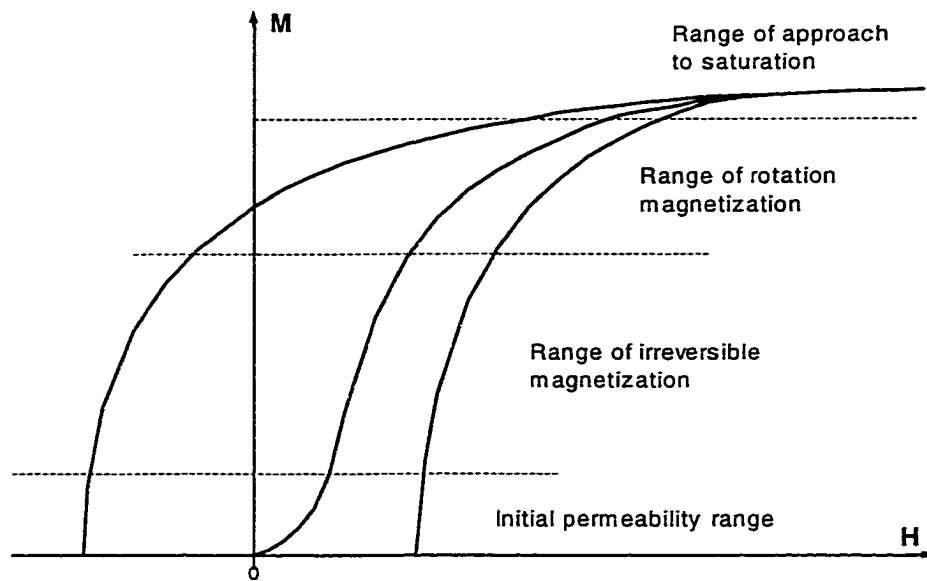


Figure 1-2 Magnetization curve and the classification of magnetization mechanism[2].

although one mechanism might be more pronounced than other in a specific magnetic material. For a soft magnetic material, for example, the domain wall motion is dominant process at a low field and the domain rotation process is dominant mechanism at a fairly high magnetic field.

As shown in Figure 1-2, from the demagnetized state, within a small magnetization range, called the initial permeability range, magnetization changes reversibly. Although both domain rotation and domain wall motion are involved, the domain wall reversible motion, either short range translation or bending, makes a major contribution to the magnetization. Beyond the initial permeability range, a further increase in the magnetic field results in a drastic increase in the intensity of magnetization. The magnetization is mainly completed by the irreversible domain wall motion when a domain wall overcomes the pinning site and moves from one stable position to another. In the range of irreversible magnetization, the contribution of the

irreversible domain wall motion is more significant than the contribution of the irreversible domain rotation in a soft magnetic material. If the magnetic field is further increased beyond the range of irreversible magnetization, since the domain wall motion is finished, domain rotation becomes the dominant mechanism, and this range therefore is called the range of rotation magnetization. Above this range, with increasing magnetic field, the magnetization gradually approaches saturation and becomes more and more reversible. Within this range of approach to saturation, the magnetic field slowly increases the magnetization by aligning all magnetic moments along the field direction against the randomization caused by thermal energy. However, for a fairly hard magnetic material, since domain rotation and domain wall motion occur almost simultaneously[2], a clear-cut discrimination of magnetization process is not always possible.

## **1.2 Development of hysteresis theory**

It was Ewing [3] who first investigated hysteresis systematically, although Warburg [4] first observed the hysteresis behavior of iron. There were many attempts to explain the hysteresis phenomenon of ferromagnetic materials and to devise theoretical descriptions of the hysteresis phenomenon. In the early investigation, there were broadly two categories of explanations of hysteresis phenomenon. One considered the friction type force, which opposes changes in magnetization, as a main cause of hysteresis. The postulation of the existence of a friction resistance to rotation of the “magnetic molecules” [5] gave a quite reasonable explanation to the most obvious effects of magnetic hysteresis.

Another theory suggested [6, 7] that the hysteresis phenomenon was due entirely to the strong mutual interaction between the individual magnetic moments. The essential features of hysteresis could be obtained from the model of the small number of strongly interacting magnetic moments. A form of hysteresis loop can be obtained on the basis of the model, although there are some obvious differences from experimentally measured hysteresis loops. The measured hysteresis loops usually show fairly smooth change in magnetization, whereas the model of only strong interactions of magnetic moments gave a rapid change in magnetization.

In the past, there were many efforts to try to develop an analytic solution or equation which fit actual experiment results of magnetization. Many models had been suggested to describe the behavior of magnetization of ferromagnetic materials.

Williams [8] gave high field magnetization curves of single crystals while Chikazumi [2] gave the high field magnetization curves of polycrystals. Rayleigh [9] suggested low field magnetization curves and hysteresis loops of polycrystalline specimens. Although they fit experiment results pretty well, they can only be used in a narrow range of field, high field or low field.

The empirical curve fitting methods [10,11,12,13,14] had also been exploited to find a way to describe magnetization behavior of ferromagnetic materials. Although in some cases [14] the resultant solution showed good agreement with experimental results, it is difficult from these to find the underlying physical meaning and relate it to the physical mechanism of magnetization and intrinsic properties of magnetic materials.

There were several theoretical approaches which attempted to describe the hysteresis phenomenon. One of them is the Preisach-Néel model [15,16,17], which is

quite widely used in the magnetic recording industry and has been found useful for modeling the magnetic properties of the recording media.

First suggested by Preisach in the 1930s, the essential idea of the Preisach model is that the observed magnetic hysteresis loops of a material are due to a summation of hysteresis loops of more elementary domains with different switching fields (local coercivities).

$$M = M_s \iint_{\alpha \geq \beta} P(\alpha, \beta) d\alpha d\beta$$

The hysteresis loop of the elementary domain, called the elementary hysteresis operator, or hysteron, is an asymmetric rectangular loop with only two states, up or down, at different switching fields. The distribution function of the switching fields, called the Preisach density function, can be used to characterize the hysteresis curve of a magnetic material.

Although it was originated from some plausible hypothesis concerning the physical mechanisms of magnetization, the Preisach model is not limited to the area of magnetics. Actually, Everett [18, 19, 20] independently invented the model and extensively investigate adsorption hysteresis in chemical processes using it. The Preisach model is therefore categorized as a mathematical model and can be applied to any mechanism exhibiting hysteresis, although it is used most extensively in magnetics.

The Preisach model works fairly well for weak interactions between domains such as those that occur in recording media, which are usually aggregates of single-domain particles, and because the magnetic moments within the elongated single-domain particles can only have magnetic moments along one axis leading to a magnetization either parallel

or antiparallel to the long axis of the particles. A comprehensive treatment of the Preisach model can be found in Mayergoyz's book on the modeling of hysteresis[21].

Although the Preisach model can be used to give reasonable mathematical representations of hysteresis curves once the curves are already known, the model really does not give much physical insight into the magnetic properties of materials, being in essence merely a complicated mathematical curve-fitting procedure.

The Globus model [22, 23] was based on the assumption that the motion of domain walls is pinned at the grain boundaries. Under the action of a magnetic field, the domain wall deforms by bending like an elastic membrane. This model gave close agreement with experiment results, but domain walls only pinned by grain boundaries is too narrow a concept to describe general hysteresis loops.

Based on the ideas that under the action of a magnetic field, domain wall motion was impeded by the uniform and isotropic distributed pinning sites, Jiles and Atherton [24] assumed that the energy loss due to the pinning is proportional to the change in magnetization. From the fact that the change of the energy supplied to a magnetic material should be equal to the change of magnetostatic energy plus hysteresis loss due to domain wall pinning, a first order differential equation for the susceptibility can be obtained to model hysteresis curve of ferromagnetic materials. In this model the change in magnetization was considered to be due entirely to uniformly impeded domain wall motion. If both domain wall motion and domain rotation are considered, the proportionality coefficient, or pinning coefficient  $k$ , between the energy loss and magnetization change will not be a constant during magnetization process[25]. Since magnetization should include both irreversible and reversible components, the model was also expanded to include both the irreversible magnetization component and the

reversible magnetization component [26], in which the reversible magnetization was assumed to be proportional to the difference between the irreversible magnetization and anhysteretic magnetization by a constant proportionality coefficient  $c$  which varies from 0, which implies a completely irreversible magnetization, to 1, which implies a completely reversible magnetization.

Based on thermodynamic principles, the Jiles-Atherton model is considered as a physical hysteresis model. Every parameter in the model has a physical meaning and can be determined from experimental hysteresis measurements[27, 28]. Because of the physical characteristic of the Jiles-Atherton model, it is possible to extend the model based on physical consideration and abstraction. For example, based on the assumption that the DC magnetization curve is the equilibrium position for the bulk magnetization and using a second order linear differential equation to describe the damped domain wall motion under the action of a time-varying field, the Jiles-Atherton model was extended to model frequency dependent hysteresis curves in non-conducting magnetic materials [29]. Later the model was also extended to take into account the effects on the hysteresis curves of eddy currents in electrically conducting media [30, 31].

Based on homogeneous pinning site distribution and the isotropic Langevin-Weiss equation, the Jiles-Atherton Model was originally isotropic. Starting from the idea that the presence of crystalline anisotropy changes the global energy equilibrium condition as well as anhysteretic magnetization, Ramesh et al [32] generalized the isotropic Langevin-Weiss model to include the crystal anisotropy to model anhysteretic magnetization of anisotropic material. This generalized anhysteretic model was later included into isotropic Jiles-Atherton model to model the hysteresis of anisotropic magnetic materials[33].

Developed on the basis of the energy balance, The Jiles-Atherton model has advantages on modeling the stress effect on the magnetization process. By introducing an equivalent stress field that is dependent on applied stress and the magnetostriction of magnetic materials, Sablik et al [34, 35] extended the model to describe the hysteresis curves under the action of a uniaxial stress. Later the model was extended to model the hysteresis curves under the application of non-coaxial stress and field [36].

### 1.3 Background

Brandt [37] patented the “Orthogonal-field electrically variable magnetic device” in 1994. As shown in Figure 1-3, it is an electro-magnetic device for use in applications requiring low-profile components. The device includes a magnetic substrate with an arrangement of through-holes in association with a first and second winding, plated and wired, integral to the substrate and wound orthogonal to each other. The first winding comprises the AC inductor/transformer permeability. The second winding in association with an applied DC bias current causes the permeability to vary over a wide controlled operating range [37].

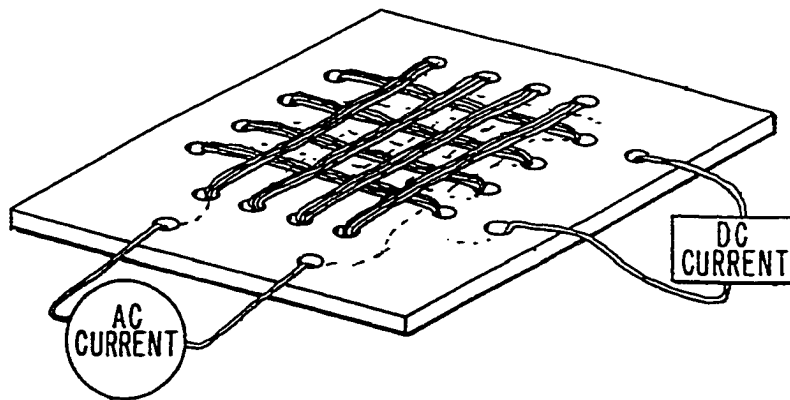


Figure 1-3 The orthogonal-field electrically variable magnetic device [37].



As claimed by the inventor, the permeability (inductance) of the primary winding can be changed over a wide range with increasing orthogonal magnetic field from the orthogonal winding. However, the behavior of the hysteresis loss of this device was not mentioned in this patent. The core loss is a major concern in the design of the power magnetics devices which is the area that this patent applied for. As a matter of fact, according to hysteresis measurements performed in this study, it has been shown that the core loss of this device will have a significant increase in the presence of the orthogonal field.

Although the device was named as orthogonal field electrically variable magnetic device and the two windings were orthogonal to each other, the magnetic fields created by the two coils actually were not everywhere orthogonal to each other within the device. In some regions of the device, the two magnetic fields were actually parallel to each other. It is believed that the inductance (permeability) variation observed by the inventor resulted mainly from the localized saturation created by the parallel fields, instead of the orthogonal field effect. The localized saturation can cause an increase in the core loss of this device.

In another configuration in the same patent, a permanent magnet was attached to the plate. The field created by the permanent magnet was orthogonal to the field created by the primary coil everywhere in the device. However, under these circumstances the inductance of this device can not be varied by the permanent orthogonal field.

Goldberg et al [38] also patented a “magnetically variable inductor for high power audio and radio frequency applications”. As shown in Figure 1-4, the main coil was the single conducting line passing through a long ferrite tube while the control coil was wound on the tube along the axial direction. The main field created by the half-turn main

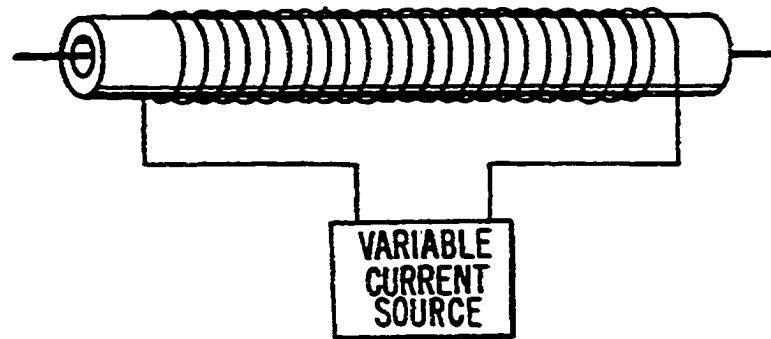


Figure 1-4 The high frequency magnetically variable inductor by Goldberg et al[38].

coil was along the circumferential direction and the field created by the control coil was along the axial direction, the two fields were orthogonal to each other everywhere within the device. Since the main coil had only half turn, the variable inductor can only be used for radio frequency applications, which was the subject of the patent. On the other hand, considering the demagnetizing effect along the axial direction, the length of the tube should be long enough so that the inductor can have a useful control range. This requirement is a disadvantage for the miniaturization of power electronic devices.

The measured susceptibility to a small AC field perpendicular to a DC bias field is called transverse susceptibility which can be used to determine the value of the anisotropy field for a particulate dispersion [39]. It was Aharoni et al [40] who first studied the reversible transverse susceptibility based on the well-known Stoner-Wohlfarth model [41] for single crystals as well as for isotropic polycrystalline materials consisting of identical grains. Elk and Hermann [42, 43] generalized the investigations of transverse susceptibility including textured samples and additional coercivity mechanisms. They showed that measurements of the transverse susceptibility of polycrystals enable one to study some properties of the switching or nucleation fields of the grain. Elk also

investigated the transverse susceptibility curve starting from a thermally demagnetized state [44].

However, the susceptibility is only one of many properties used to characterize the response of a magnetic material under the action of a magnetic field, while the hysteresis loop, which contains the information of susceptibility, permeability, remanence, coercivity and hysteresis loss, can much better characterize a magnetic material. Additionally, the above analysis of the transverse susceptibility was based on the Stoner-Wohlfarth model which is based on the magnetic moment rotation (domain rotation) of isolated, uniaxial single domain particles against the anisotropy field. The Stoner-Wohlfarth model ignored the interaction among magnetic moments and the domain wall motion which is believed to be a major contribution to magnetization in the low field region.

On the other hand, the Jiles-Atherton model includes both domain wall motion and inter-domain coupling and has been reported to work well for modeling hysteresis curves of both soft and hard magnetic materials. Therefore it is more physical to use the Jiles-Atherton model instead to model the hysteresis curve of a magnetic materials under the action of two magnetic fields which are orthogonal to each other.

However, the Jiles-Atherton model basically is a one-dimensional hysteresis model, i.e. the applied magnetic field and magnetization are in the same direction and all variables and parameters in the model are scalar. When two magnetic fields are applied simultaneously, the total magnetic field  $\mathbf{H}$  and magnetization  $\mathbf{M}$  are vectors. Due to nonlinearity and hysteresis of magnetic materials, the superposition principle for a linear system can no longer be used. The magnetization  $\mathbf{M}$  is neither proportional to the magnetic field  $\mathbf{H}$  nor on the same direction of the magnetic field  $\mathbf{H}$ . The modeling

therefore becomes much more complicated. In addition the resultant magnetization is not simply a function of the resultant magnetic field obtained by vector addition because the order of application of the magnetic field components is important.

#### **1.4 Scope of this thesis**

Research performed in this study can be divided into two categories. The first one was the investigation of the orthogonal field effect, its modeling and applications. The results of this research will be presented in this thesis in detail. The second one was the investigation of the nondestructive evaluation of materials using magnetic techniques, which will be presented in appendix in the form of published journal papers.

Beginning with a general introduction, which provides a background for the research into the orthogonal field effect, and ending with a general conclusion in chapter 6, this thesis consists of six chapters.

In this study, the orthogonal field effect has been studied experimentally in different magnetic materials, under different experimental conditions using different hysteresis measurement systems. Chapter 2 will present some results of this investigation along with corresponding analysis and discussion.

After a brief review of a one-dimensional hysteresis model, Chapter 3 will discuss the extension of the isotropic hysteresis model to include the orthogonal field effect. In this study, the orthogonal field effect was treated as an anisotropy in affecting the magnetization of isotropic magnetic materials. The experimentally observed reversible domain rotation under the action of an orthogonal field was also incorporated into the extended hysteresis model by introducing a dynamic reversibility coefficient into the

model. The modeled hysteresis curves will be compared with experimental hysteresis curves in this chapter.

Chapter 4, which includes the design of a variable inductor, will discuss the investigation of developing applications for the orthogonal field effect to increase energy storage and to provide inductance controllability. The inductance and hysteresis measurements on two prototype variable inductors will be presented along with corresponding analysis and discussion.

In this study, the finite element modeling (FEM) has extensively been used as a tool to evaluate magnetic field distribution and simulate the magnetic properties of magnetic devices. Chapter 5 will present some results of these modelings which include 2D flux line distribution, internal field along a toroid axis, 3D induction distribution and the simulation of device inductance.

## **2. MEASUREMENTS OF THE ORTHOGONAL FIELD EFFECT**

### **2.1 Introduction**

The effect of the orthogonal field was investigated experimentally on different magnetic materials, under different measurement conditions. The main objective of these measurements was to investigate hysteresis behavior of isotropic magnetic materials under the action of an orthogonal field. Another objective was to study whether the orthogonal field effect is material dependent. Two properties of interest were hysteresis loss and effective permeability. By effective permeability is meant the measured ratio of induction  $B$  and field  $H$  along the same direction, even in the presence of another orthogonal field.

Since the orthogonal field effect can be visually appreciated through hysteresis curves and properties of magnetic material under the action of an orthogonal bias field can be extracted from the hysteresis loops, hysteresis measurement was the main experimental tool to investigate the orthogonal field effect, although inductance measurements of magnetic devices were also made during this study.

In this chapter, some results of hysteresis measurements made on nonconducting ceramics ferrites, conducting polycrystalline silicon iron and amorphous ribbon under different experimental conditions will be presented. In general it was found that the orthogonal field rotated the hysteresis loop clockwise and reduced the area of the hysteresis loop. As a result, the effective permeability, hysteresis loss, coercivity and remanence decreased with increasing orthogonal field.

## 2.2 Measurements on ferrite plate

### 2.2.1 Specimen and experimental method

The specimen, a circuit board embedded ferrite inductor (BEFI), was provided by Rockwell Collins as shown in Figure 2-1. Overall dimensions of the device were  $25.4 \times 33 \times 2.5$  mm. Originally designed for a low-profile inductor, the coil was printed on the board on both sides and connected through the small holes. For a hysteresis measurement made by AMH-401 hysteresisgraph, it was necessary to have two sets of coils, one for magnetic field excitation and another for magnetic induction measurement.

Considering the fact that the printed coil, which closely contacted with the specimen, had an easily evaluated cross sectional area and could not carry a large current, the printed coil was used as flux pick-up coil in this study. The excitation coil was wound using insulated copper wire through the holes. The orthogonal field was created by an external solenoid along the length direction of the specimen. The magnetic field created by the solenoid was easy to evaluate. However, the real internal orthogonal field inside the specimen was difficult to evaluate due to the demagnetizing effect. As detailed in

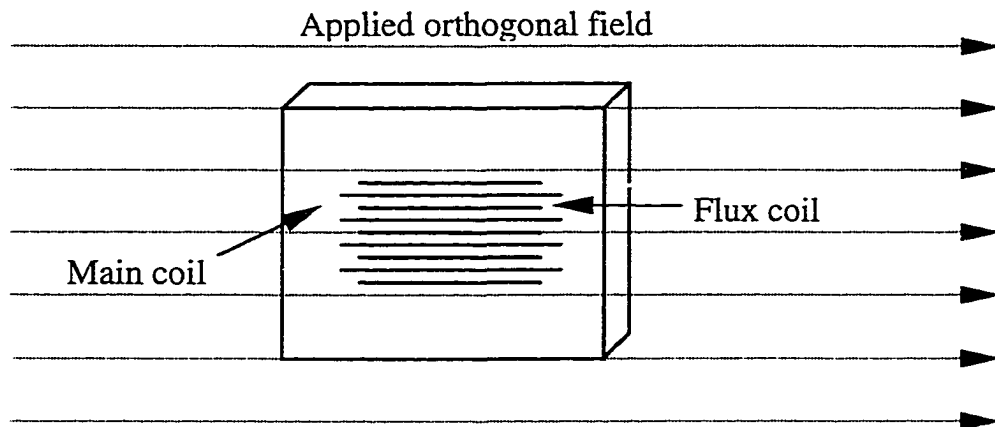


Figure 2-1 The geometry of BEFI and the applied orthogonal field.

chapter 5 by FEM modeling, the magnetic field created by the excitation coil was not uniformly distributed. Additionally, the field created by the excitation coil was not always perpendicular to the orthogonal field created by the solenoid. In some regions of specimen, the two fields were even parallel or anti-parallel to each other. This lead to further complication in analyzing the orthogonal field effect.

Hysteresis measurements were carried out using an AMH-401 Automatic Soft Hysteresisgraph, developed by Walker Scientific, Inc.. This computerized hysteresis measurement system is able to measure the hysteresis response of magnetically soft materials at frequencies ranging from 50 Hz to 1 MHz. It is suited to any method of test in which the magnetizing force (  $H$  ) is directly proportional to the magnetizing current. The main components of this system include specimen pod, high frequency amplifier and a signal generating and digitizing card which resides inside in the computer. Besides the hysteresis loops, this system also displays maximum flux density, permeability, core loss, remanence and coercivity for the characterization of magnetic materials. The magnetization mode can be specified to  $H_{\max}$  (drives to specified maximum field  $H$  value),  $B_{\max}$ (drives to specified maximum induction  $B$  value),  $V_{2\max}$ (drives to specified peak secondary voltage value).

However, there is a limitation for voltage and power output of the high frequency power amplifier. When the excitation frequency was increased, due to the increasing reactance which is proportional to the frequency, higher voltage was needed to apply the same current amplitude. When a measurement was made at high frequency, only minor hysteresis loops can be measured using this system, except for very small inductance devices.



Designed for the toroidal shape of specimen, the applied magnetic field is evaluated by measuring the excitation current using Ampere's circuital law. In a toroidal structure, the magnetic field on any cross-section of toroid can be approximately considered to be uniform if the magnetic field is along the circumferential direction. Because of the uniformity of magnetic field, Ampere's circuital law

$$\oint \vec{H} \cdot d\vec{l} = NI$$

can be used to determine the applied magnetic field:

$$H = \frac{NI}{2\pi R}$$

For a non-toroidal specimen, such as this BEFI plate, however, the magnetic field can not be evaluated in this way. Considering the fact that the flux lines have to circulate within the specimen, the flux path length, which is necessary to evaluate the magnetic field in this system, was estimated as 46 mm using 2D linear FEM modeling so that the product of the path length and the averaged field strength in the region below the main coil was equal to the applied magnetomotive force.

### 2.2.2 Results and discussion

The effects of the orthogonal bias field on hysteresis curves of BEFI specimen are shown in Figure 2-2. The external orthogonal field generated was from zero to 9200 A/m. Due to the demagnetizing effect, the real internal orthogonal field was expected to be less than the external applied field.

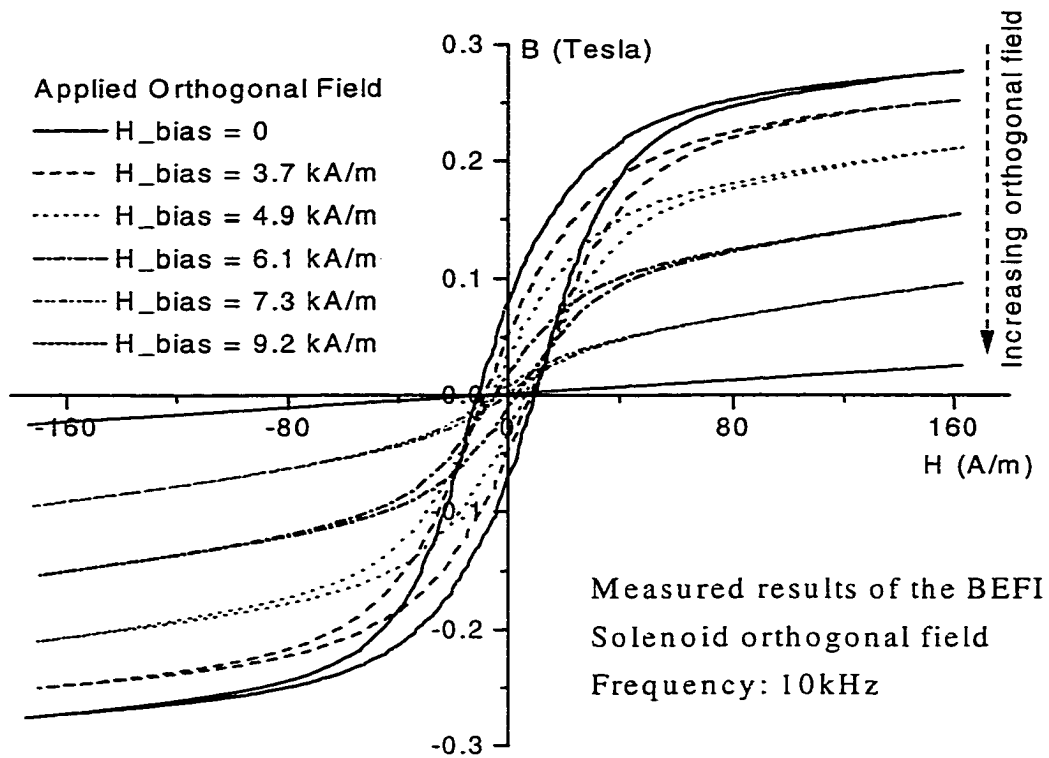


Figure 2-2 The effect of an orthogonal field on hysteresis loops of BEFI.

The measurements showed a decrease in the maximum induction for a given excitation field as the orthogonal bias field was increased. Graphically, the hysteresis loops appeared to be gradually rotated clockwise with increasing orthogonal bias field. The hysteresis loop rotation can be characterized by the change in maximum flux density for a given excitation field as shown in Figure 2-3. As a result, the effective permeability is expected to decrease with increasing orthogonal bias field. From the measurements above, the effective permeability was decreased from 5900 without an orthogonal field to about 120 with an external orthogonal field of 9200A/m. As we know, the inductance of an inductor is proportional to the effective permeability of its core material. Since we can reduce the effective permeability by a factor of 100, it is possible that we can change the inductance of an inductor by the same amount using a variable orthogonal field.

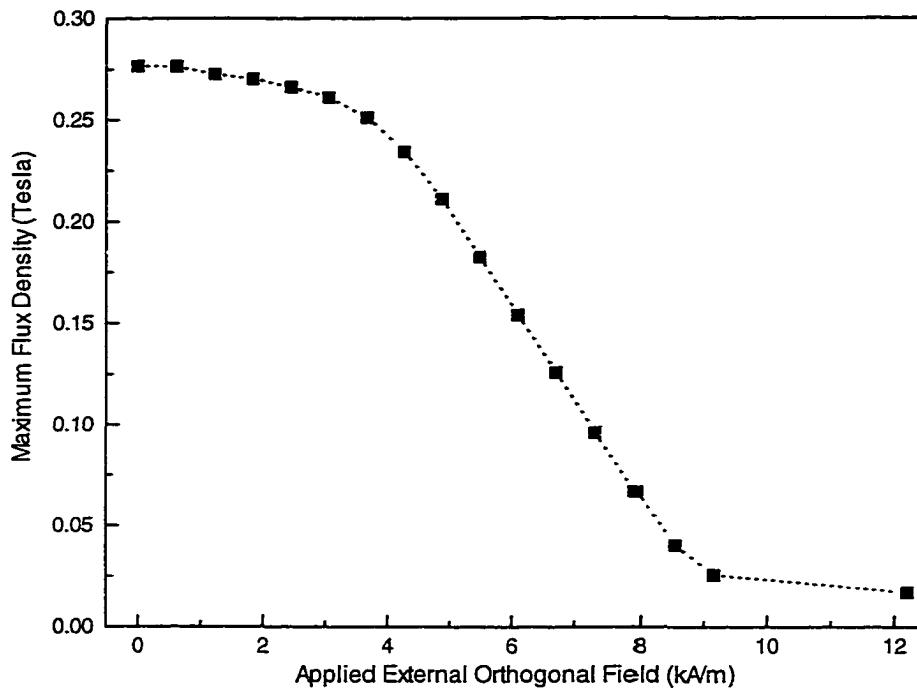


Figure 2-3 The effect of the orthogonal field on maximum induction of BEFI device for an applied excitation field of 165A/m.

At the same time, the increasing orthogonal field reduced the area of the hysteresis loops until they approximated a straight line. This can be characterized by the change in hysteresis loss which is the area of a hysteresis curve under the action of an orthogonal field as shown in Figure 2-4. As a result of the loop shrinkage, the remanence and coercivity are also expected to decrease with increasing orthogonal field. For the device above, core loss was dramatically decreased from  $86 \text{ kW/m}^3$  without an orthogonal field to  $0.36 \text{ kW/m}^3$  with an orthogonal field of  $8.5 \text{ kA/m}$ . The core loss is one of design concerns in power electronics devices. A decrease in core loss means improved energy efficiency or reduced device dimension. The above results indicates that it is possible to reduce the core loss by applying an orthogonal bias field. Of course, this comes at the expense of a decrease in the effective permeability.

It is interesting to note that the reversible magnetization regions, which are regions that upper curve and lower curve of the hysteresis loop overlap each other, gradually increased with increasing orthogonal bias field. Under the action of a magnetic field, magnetization consists of both irreversible and reversible components, and the irreversible magnetization is responsible for the hysteresis loss of magnetic materials. The experimental results above indicate that the orthogonal field reduces the hysteresis loss by increasing the reversible region and decreasing the irreversible region of magnetization.

It should be remembered that the two fields, created by on-board excitation coil and external solenoid respectively, were not everywhere normal to each other within the specimen. The field created by the on-board excitation formed a horizontal “figure of eight” (this will be detailed in chapter 5) while the orthogonal field created by the solenoid was always parallel to the direction of specimen length. Therefore, in some

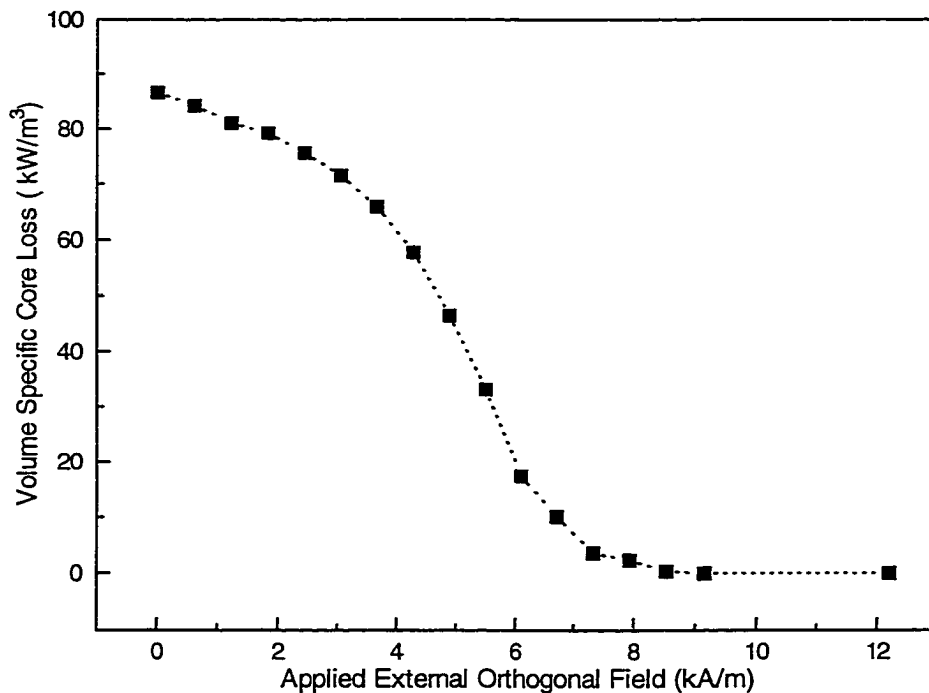


Figure 2-4 The effect of the orthogonal field on hysteresis loss of BEFI device for an applied excitation field of 165 A/m.

regions within the BEFI the two fields were not perpendicular to each other and were even to parallel to each other in some regions, although the two fields were orthogonal to each other in the region under the excitation coil. Additionally, the field created by the excitation coil was not uniformly distributed within the device.

Besides the interest of the research sponsor in low profile, flat plate electronics, one of reasons for studying the effect of the orthogonal field on this BEFI device was its large dimensional ratio so that the demagnetizing effect along the orthogonal direction was not very large, the orthogonal field effect can be fully exhibited. With a moderate strength of an external orthogonal field, the measured hysteresis loop can be fully rotated and shrunk until a straight line. Because of its nonuniform magnetic field distribution and not complete orthogonality between the two fields, the measurement results were only used in the qualitative investigation of the orthogonal field effect.

### **2.3 Measurements on a ferrite toroid**

For a toroidal structure, if one magnetic field is applied along the circumferential direction and another field is applied along the symmetric axial direction of the toroid, the two magnetic fields are perfectly perpendicular to each other everywhere in the toroid. This has some obvious advantages from an analytic perspective. Additionally, the field along the circumferential direction can be approximately considered as uniform and its value can be easily evaluated using the Ampere's circuital law. A disadvantage for toroidal structures is that the demagnetizing effect along the axis direction is strong, specially for a normal shape of toroid. In order to fully exhibit the orthogonal field effect, either a very strong magnetic field has to be applied along the axis direction, or a toroidal

specimen with long dimension along the axis direction should be selected to minimize the demagnetizing effect.

In this study, a long MnZn ferrite toroid was selected for the study of the orthogonal field effect. The geometry of specimen and the applied magnetic fields are shown in Figure 2-5. The outer diameter, inner diameter and length was 14.4 mm, 6.5mm and 28.4 mm, respectively. The main excitation magnetic field which was along the circumferential direction of the toroid was created by a 12-turn coil wound on the toroid in a toroidal manner. The magnetic flux along the circumferential direction was measured by a 10-turn coil wound on the toroid. The orthogonal field along the axis direction of toroid was produced by an external solenoid.

### 2.3.1 Measurements under large magnetic field

Figure 2-6 shows the effect of an orthogonal bias field on the hysteresis loop of long ferrite toroid. The result was similar to that observed with the flat ferrite plate. The orthogonal field rotated and shrank the hysteresis loop.

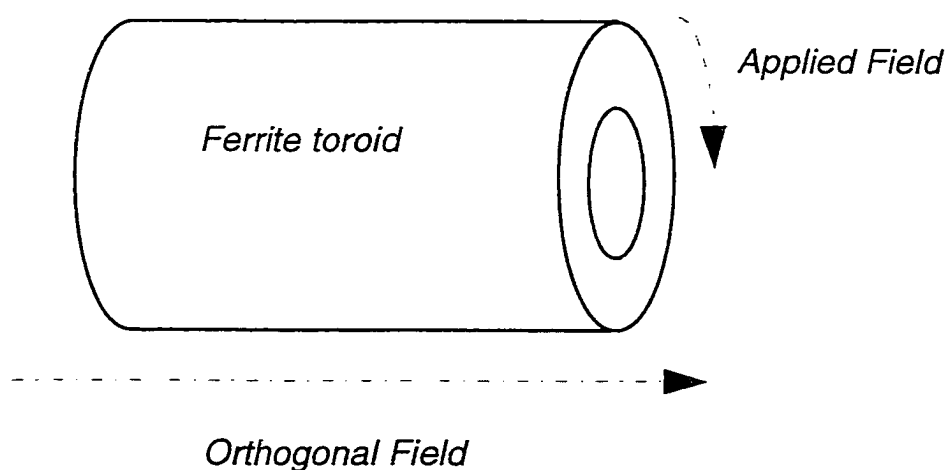


Figure 2-5 Long MnZn ferrite toroid and applied magnetic fields.

It is noted that the hysteresis loop had only very small rotation under the action of a high external orthogonal field. This is believed to be due to the demagnetizing effect along the orthogonal field direction. The magnetic field inside the specimen results from the superposition of the applied field and the demagnetizing field.

$$H_{\text{effective}} = H_{\text{applied}} - NM \approx H_{\text{applied}} - N\chi H_{\text{effective}}$$

$$H_{\text{effective}} = \frac{H_{\text{applied}}}{1 + N\chi}$$

Since the susceptibility of ferrite is very large ( $\sim 3000$ ), the effective magnetic field was only a small fraction of the external field. For a specimen with a demagnetizing factor of 0.01, the effective field inside the specimen is only 3.3% of the external field.

The decrease in the area of hysteresis loop is clearly evident under the action of an orthogonal field. Since the orthogonal field reduced the magnetic induction at the same

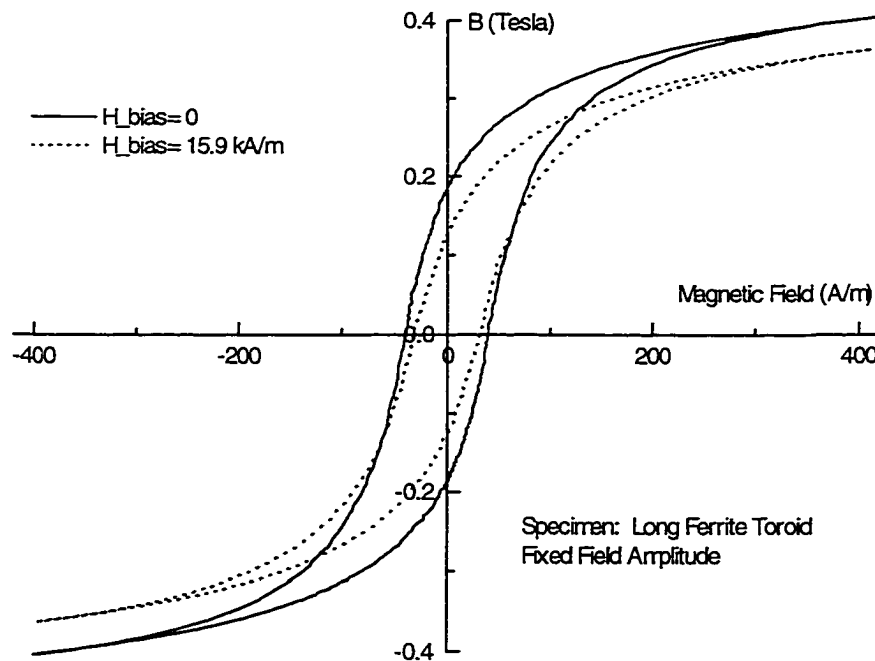


Figure 2-6 The effect of an orthogonal field on hysteresis loop of a long ferrite toroid in fixed field amplitude measurements.

magnetic field and core loss can be decreased simply by reducing the effective magnetic field (for example by inserting an air-gap into the magnetic circuit), the next question is whether the core loss still decreases when the magnetic induction reaches the same level. In order to answer this question, fixed induction amplitude measurements, in which maximum induction was maintained at the same level as without an orthogonal field, were made on the same specimen. In contrast, the measurement, in which maximum applied magnetic field was kept the same under different orthogonal fields, was called the fixed field amplitude measurement.

As shown in Figure 2-7, under the action of an orthogonal field, due to the decrease in the effective permeability, a higher magnetic field  $H$  must necessarily be applied in order to obtain the same level of magnetic induction  $B$ . As a result, the magnetization curve was elongated along the  $H$  axis. However, the fact that two branches of elongated hysteresis curve converged together indicated that the elongation of hysteresis loop was completed by adding reversible magnetization which is hysteresis free. Since the reversible elongation of hysteresis curve did not increase the area of loop, the core loss decreased as observed in the fixed field amplitude measurements. The result is shown in Figure 2-8 where hysteresis loss against the orthogonal field is plotted under two magnetization modes. Under both modes, the hysteresis loss showed a decrease with increasing orthogonal field. The rotation of hysteresis loops under the action of the orthogonal field can be characterized by their changes in effective permeability as shown in Figure 2-9 which shows a gradual decrease in the effective permeability with increasing orthogonal field.



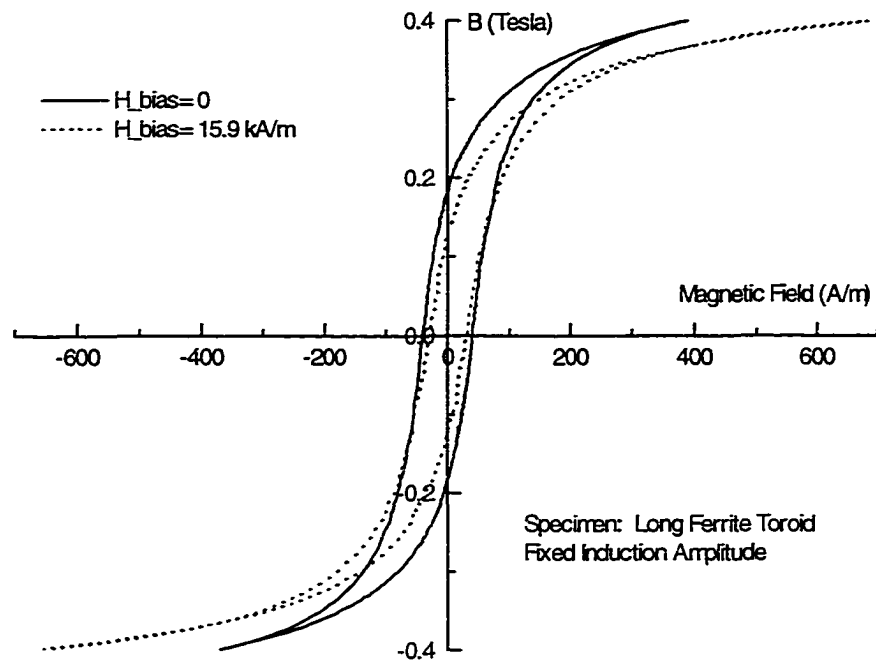


Figure 2-7 The effect of an orthogonal field on hysteresis loop of a long ferrite toroid in fixed induction amplitude measurements.

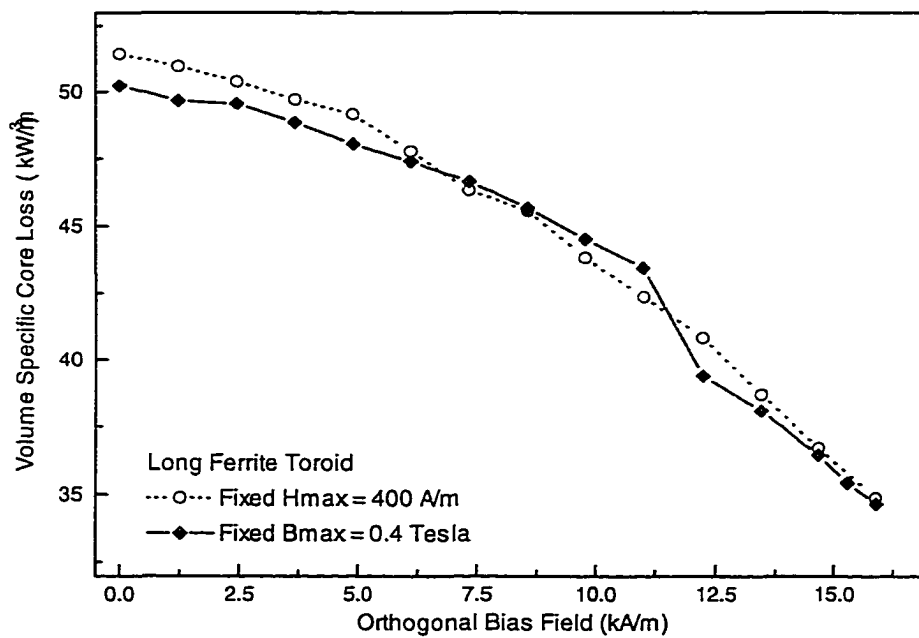


Figure 2-8 The effect of the orthogonal field on hysteresis loss of a long ferrite toroid.

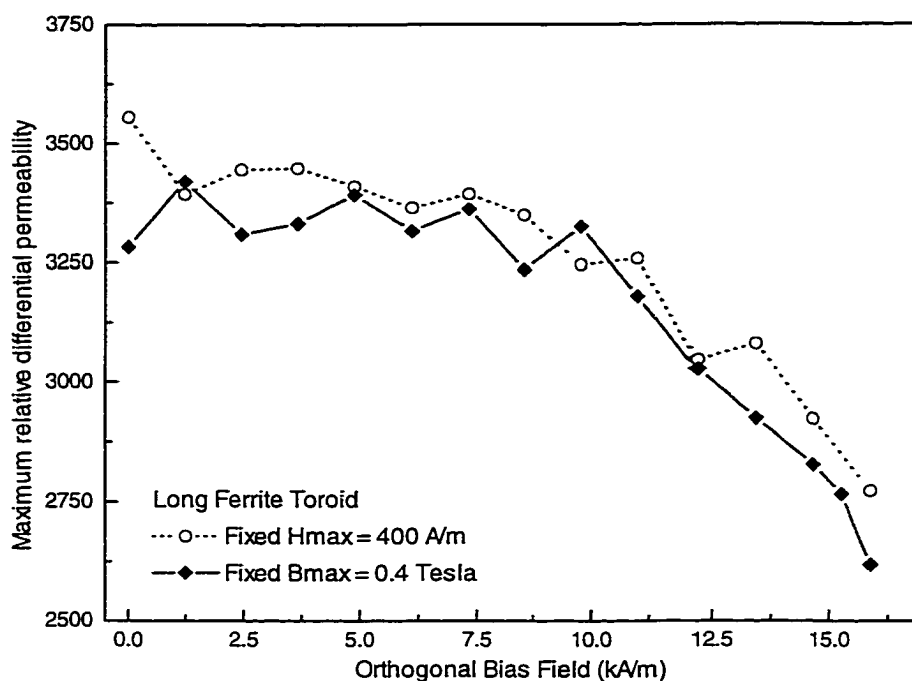


Figure 2-9 The effect of an orthogonal field on the permeability of a long ferrite toroid.

### 2.3.2 Measurements under small magnetic field

For most magnetic devices, the material inside the device is designed to be magnetized to an induction level well below saturation to avoid an excessive core loss. The study of the orthogonal field effect, specially core loss, under low magnetization mode is of great interest for power electronics applications.

Figure 2-10 shows the effect of an orthogonal bias field on the small field amplitude hysteresis of the long ferrite toroid in the fixed field amplitude measurements. As observed before, the hysteresis loop was rotated and the area of hysteresis loop was reduced by the orthogonal field. As a result, the hysteresis loss and effective permeability decreased. The effect of an orthogonal bias field on the small field amplitude hysteresis of

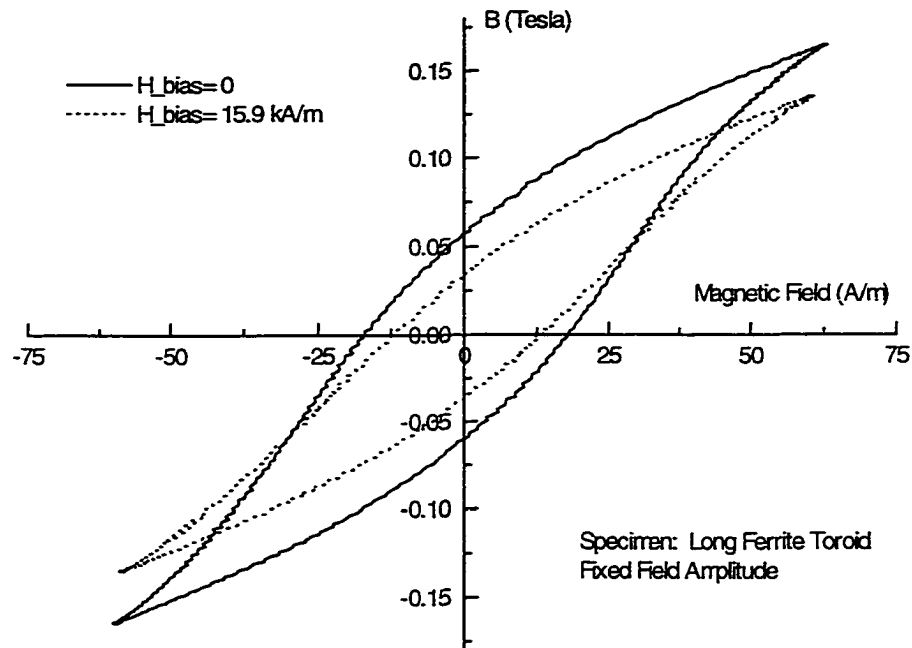


Figure 2-10 The effect of an orthogonal field on the small field hysteresis loop of a long ferrite toroid in fixed field amplitude measurements.

the long ferrite toroid in the fixed induction amplitude measurements is shown in Figure 2-11. A higher magnetic field was needed to obtain the same level of magnetic induction due to the decrease in the effective permeability. However, the fact that two branches of the elongated hysteresis loop did not converge together indicated that the elongation of hysteresis loop was completed by adding irreversible magnetization, instead of adding reversible magnetization as observed in Figure 2-7.

If there is no orthogonal field, then under a weak excitation field, the increase of magnetization is attained mainly by domain wall motion. Due to the domain wall pinning, the magnetization contains both reversible and irreversible magnetization components. For experimental conditions here, both the exciting field and the orthogonal bias field were weak. The reversible domain rotation process, which mainly occurs at high fields

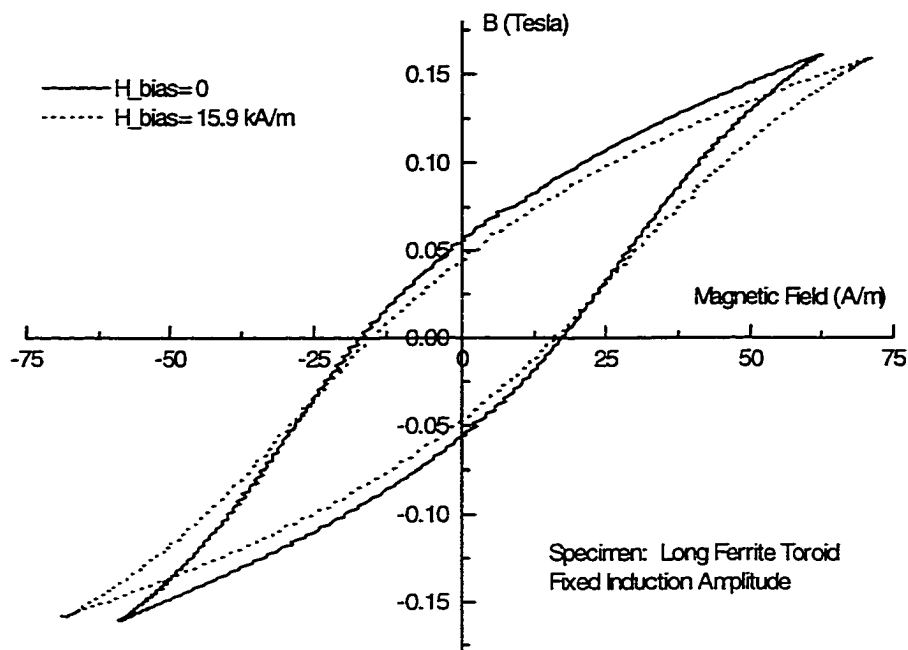


Figure 2-11 The effect of an orthogonal field on the small field hysteresis loop of a long ferrite toroid in fixed induction amplitude measurements.

could not be fully established. Therefore, in order to reach the same magnetic induction, magnetization increased mainly by irreversible domain wall motion. With increasing orthogonal field however, the reversible rotation magnetization component gradually increased. The core loss can therefore be expected to have a slight decrease in the fixed induction amplitude measurements. This is shown in Figure 2-12 where decreases in core loss for both measurement modes are plotted. Figure 2-13 shows the effect of an orthogonal bias field on the effective permeability of the long ferrite toroid which can be considered as a representation of hysteresis loop rotation under the action of an orthogonal field.

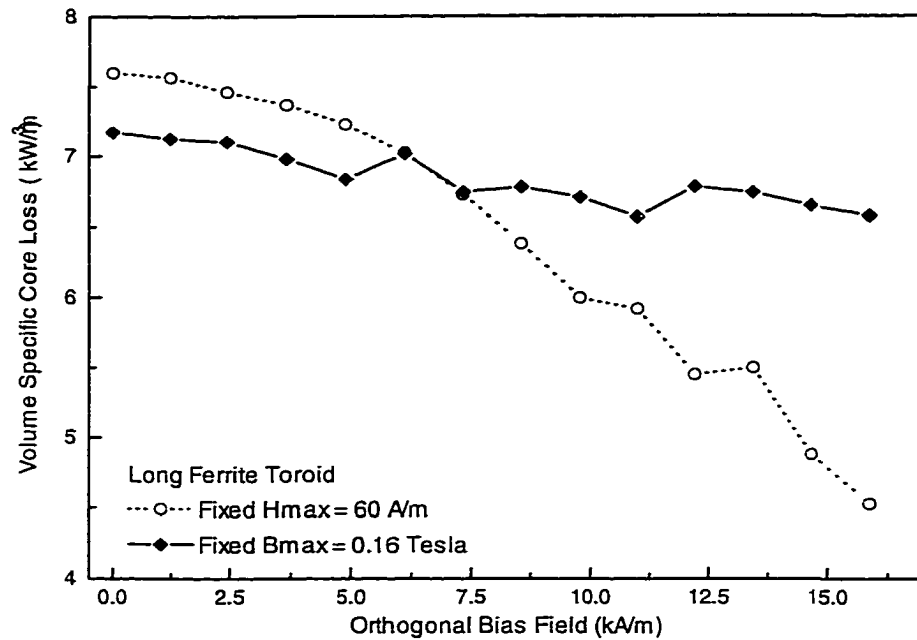


Figure 2-12 The effect of the orthogonal field on the hysteresis loss of a long ferrite toroid in small magnetization measurements.

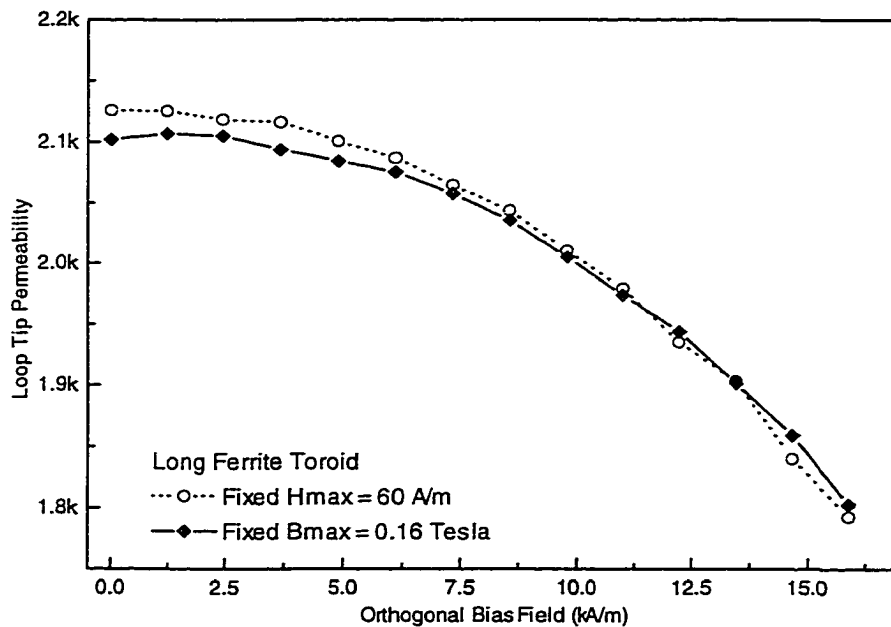


Figure 2-13 The effect of the orthogonal field on the effective permeability of a long ferrite toroid in small magnetization measurements.

### 2.3.3 Measurements at high frequency

For non-conducting ferrite, the classical eddy current loss, which is proportional to the square of frequency, can be ignored. At high excitation frequency, however, the excess loss, which results from domain wall damping under the action of alternating magnetic field and is proportional to the power of 1.5 of frequency, becomes significant. The effect of the orthogonal field was also studied at higher frequency in this study. The objective was to investigate whether the orthogonal field effect is frequency dependent. Due to the power limitation of AMH-401 hysteresisgraph, only low magnetization measurements at frequencies below 80KHz were made during this study.

Figure 2-14 shows the effect of the orthogonal bias field on the hysteresis loop of the long ferrite toroid at the frequency of 80 KHz in the fixed field amplitude

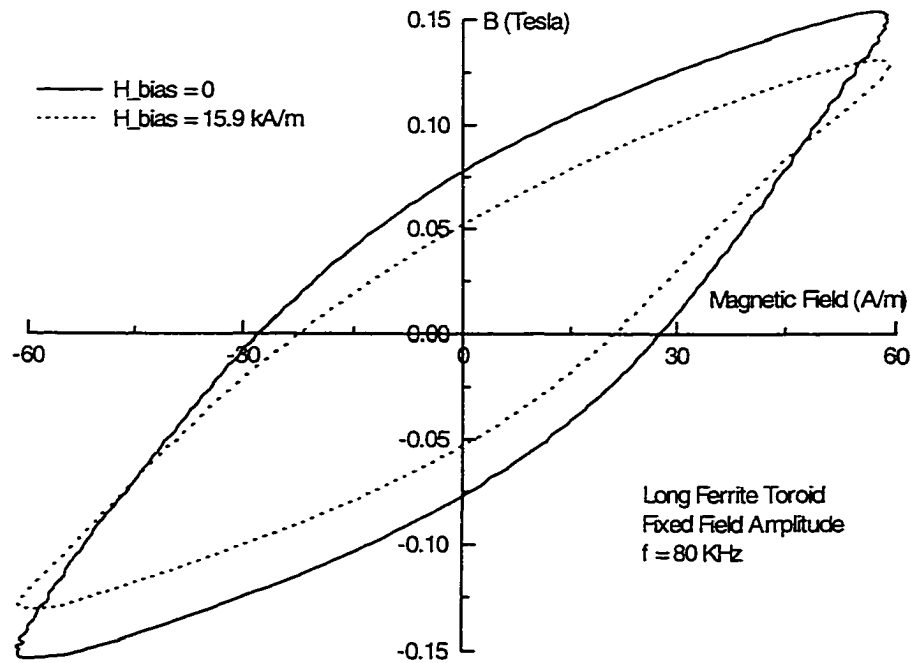


Figure 2-14 The effect of the orthogonal field on hysteresis loop of a long ferrite toroid in fixed field amplitude measurements at 80KHz.

measurements. Both hysteresis loops with and without an orthogonal field showed increase in loop area compared with hysteresis loops measured at 1KHz. As observed before, the orthogonal field rotated the hysteresis loop and reduced the area of the hysteresis loop. As a result, the permeability and hysteresis loss decreased with increasing orthogonal field at the high frequency magnetization.

Figure 2-15 shows the orthogonal field effect on the same ferrite toroid in the fixed induction amplitude measurements. Since both main field and orthogonal field were small, in order to reach the same magnetization under the influence of an orthogonal field, magnetization was increased mainly by irreversible domain wall motion instead of reversible domain rotation. Figure 2-16 shows the effect of orthogonal field on the core loss at a frequency of 80 KHz. In the fixed induction amplitude measurements, the core

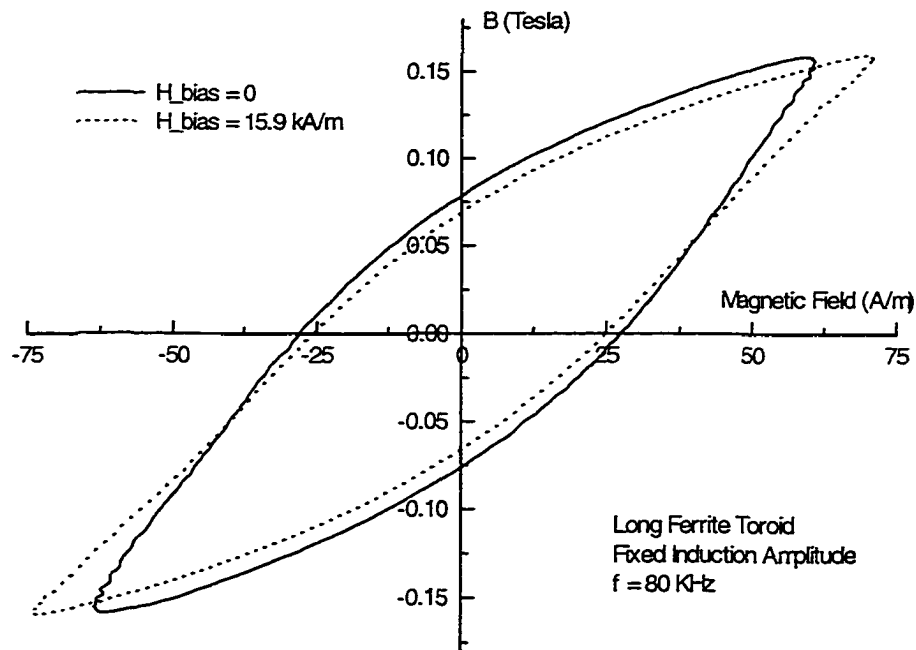


Figure 2-15 The effect of the orthogonal field on hysteresis loop of a long ferrite toroid in fixed induction amplitude measurements at 80KHz.

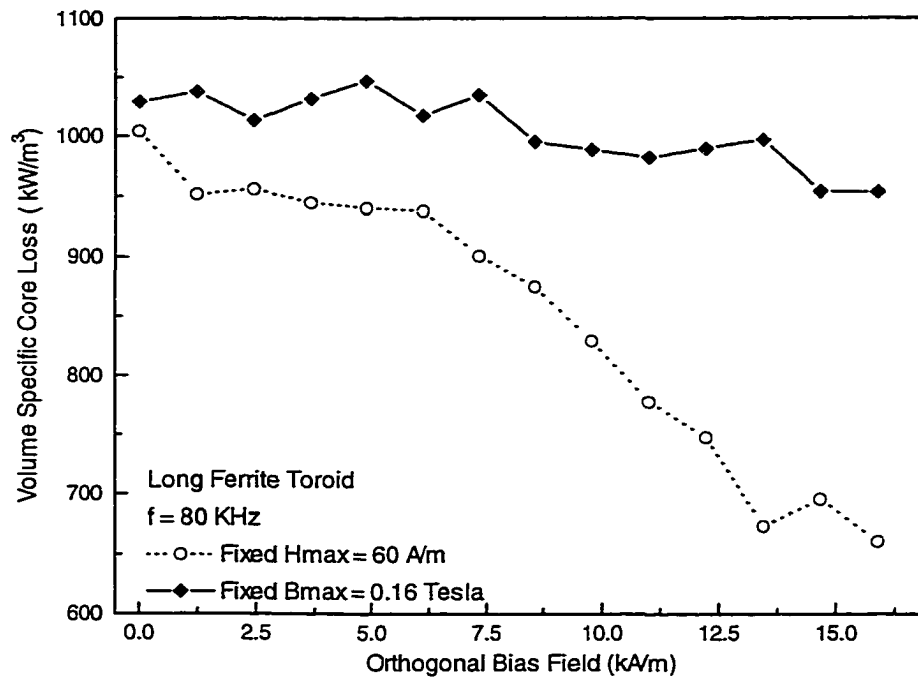


Figure 2-16 The effect of the orthogonal field on hysteresis loss of long ferrite toroid for small magnetization at 80KHz.

loss only showed slight decreases under the action of an orthogonal field. Figure 2-17 shows the effect of different values of orthogonal field on the effective permeability. Both show decreasing trends. The measurement results above indicate that the orthogonal field had a similar effect on the high frequency magnetization as it had on the low frequency magnetization. At high frequency, the orthogonal field rotated the hysteresis loop, reduced the hysteresis loss and the effective permeability, although the magnitude of these effects was frequency dependent.

#### 2.4 Measurements on conducting magnetic materials

As part of an exchange visit to the Istituto Elettrotecnico Nazionale Galileo Ferraris at Turin, Italy, experimental investigations on the orthogonal field effect were



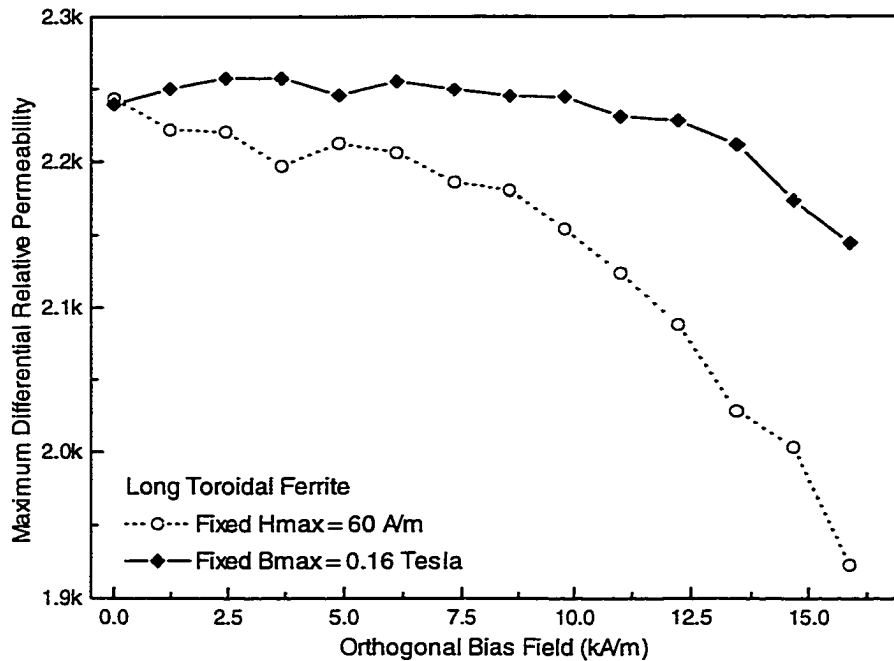


Figure 2-17 The effect of the orthogonal field on effective permeability of long ferrite toroid for small magnetization at 80KHz.

performed. This visit was a part of the collaborative research project sponsored by NATO Scientific Affairs Division. The objectives of this project were (i) to bring together the two major classes of model of hysteresis, the mathematical Preisach model and the physical model based on consideration of domain mechanisms, (ii) to explore the common basis for these two models, and (iii) to integrate the two into a single consistent and coherent theory of magnetic hysteresis which can be used in future as an accepted basis for describing and comparing magnetic materials. One of objectives of this visit was to experimentally investigate the hysteresis of conducting magnetic materials under the action of an orthogonal bias field using the hysteresis measurement systems developed there.

## 2.4.1 Measurements on M-190 polycrystalline silicon iron plate

### *2.4.1.1 Specimen characterization and preparation*

The raw specimen material, M-190 silicon iron plate with a nominal thickness of 0.02 inch, was provided by Ames Laboratory. It was cut and machined into specimens there according to the geometrical requirements of the hysteresis measurement system.

Considering the importance of precise thickness in the flux density measurement, the thickness of specimen was evaluated through the specimen resistivity based on the empirical relationship between resistivity  $\rho_m$  and density  $\rho$  of silicon iron sheet[45].

$$\rho_m = 7.973 \times 10^3 - 89.2 \times 10^3 \rho_m \rho$$

Since both mass  $m$  and resistance  $R$  of a strip specimen depend on the dimensions of the strip, it can be proved that:

$$\rho_m \cdot \rho = \frac{R \cdot m}{L \cdot L_e}$$

where  $L$ , the total length of the strip specimen, and  $L_e$ , the electrical path length, can be measured with good accuracy. Therefore, the thickness of a strip specimen with a width of  $w$  can be obtained by the following expression with better precision:

$$d = \frac{m}{Lw\rho_m} = \frac{m}{Lw(7.973 \times 10^3 - 89.2 \times 10^3 \frac{R \cdot m}{L \cdot L_e})}$$

The thickness evaluated by this method was 0.484mm, density was 7.865 g/cm<sup>3</sup>, resistivity was  $15.34 \times 10^{-8}$  ( $\Omega$  m), the estimated silicon concentration was 0.4 wt%.

In order to ensure uniformity of the demagnetizing field specimens were machined into circular shape with different diameters and stacked together into elliptic

cross-section so that a uniform distribution of demagnetizing field inside the specimen can be obtained.

#### 2.4.1.2 Instrumentation

Hysteresis measurements were made using a computerized 2D rotational field hysteresis system developed by the Istituto Elettrotecnico Nazionale (IEN) Galileo Ferraris. As schematically represented in Figure 2-18, two magnetic fields were created by a set of double yokes, which were made of laminated silicon iron and were positioned normal to each other. This system was originally designed and developed for hysteresis measurements under rotating field. After re-programming the system, it was able to measure hysteresis curves of magnetic materials under the action of a fixed orthogonal bias field.

In this system, both magnetic field  $H$  and magnetic induction  $B$  were measured by the coil method based on the Faraday's law. Magnetic fields inside the specimen in two

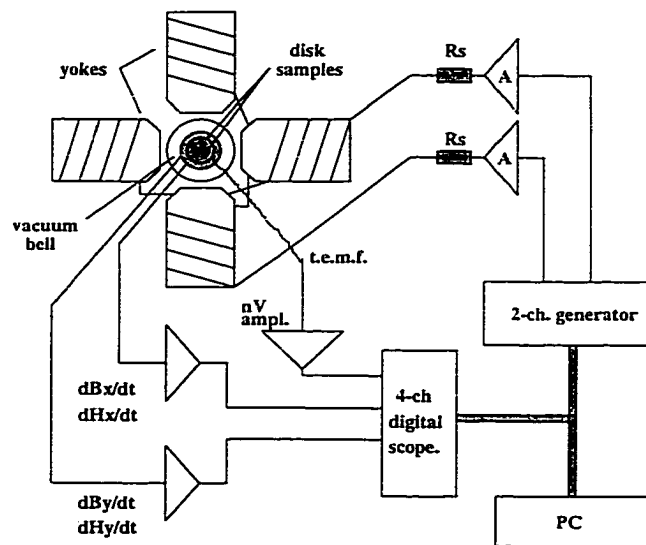


Figure 2-18 Block scheme of the 2D hysteresis measurement system developed by IEN.

directions were measured by a pair of coils, called H-coils, which were assembled into the stacked specimens and were perpendicular to each other. Although the Faraday's law gives magnetic induction  $B$ , magnetic field  $H$  in the air can be evaluated based on the simple linear relationship between magnetic field and magnetic induction. Since the pair of H-coils were close to the specimen surface and the tangential component of magnetic field is continuous across the interface between specimen and H-coil, the magnetic field detected by the coil can be considered to be equal to the field inside the specimen. On the other hand, flux densities in two directions were measured by a pair of flux coils which were wound in the specimen through the small holes on the stacked specimens.

#### *2.4.1.3 Results and discussion*

Figure 2-19 shows the effect of an orthogonal field of 550 A/m on the hysteresis loop of the M-190 silicon iron plate. The solid line was the hysteresis loop without an orthogonal field in which the applied voltage in the main excitation coil was 3.75V. Under the action of an orthogonal field of 550 A/m, as shown with dashed line, a voltage of 2.5V was applied in the main coil to reach the same field strength of 560 A/m. On the other hand, as shown with the dotted line, a voltage of 4.0V was needed to apply in the main coil to reach the same magnetic induction of 1.1 Tesla. In the fixed field amplitude measurement, the orthogonal field rotated the hysteresis loop and reduced its area. As a result of this effect, the effective permeability and core loss decreased with increasing orthogonal current. Under the action of the same orthogonal field, in the fixed induction amplitude measurement, the hysteresis loop was rotated and elongated along the H axis. Only a slight shrinkage at the coercive points was observed in the fixed induction

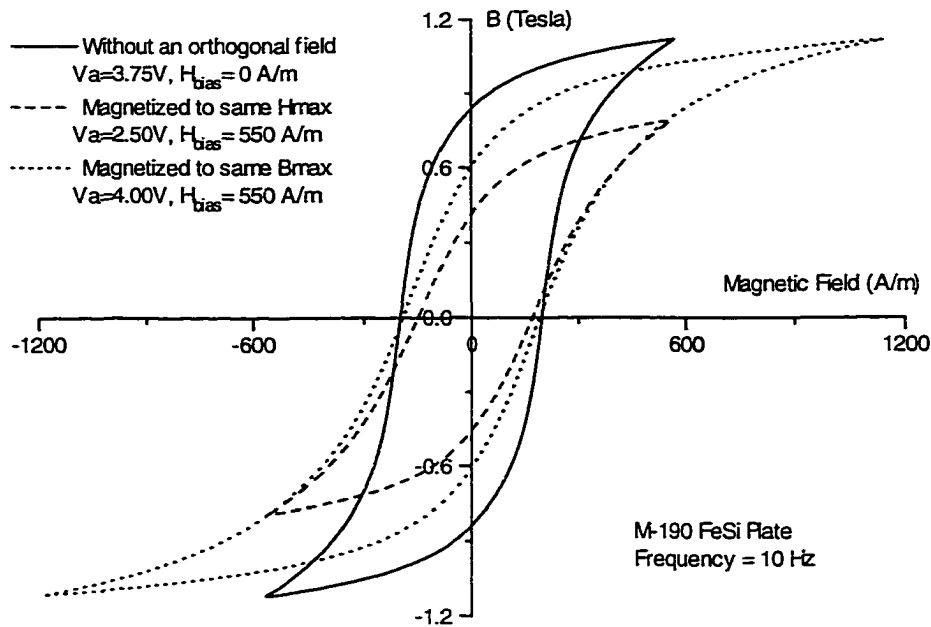


Figure 2-19 The effect of an orthogonal field on an FeSi plate specimen.

amplitude measurement. Considering the fact that the iron had a saturation magnetization of about 2 Tesla, it can be concluded that all these measured loops were low magnetization loops in which the irreversible domain wall motion was dominant magnetization process. The presence of another small orthogonal field reduced the effective permeability. In order to reach the same level of magnetization, magnetization was completed by adding more irreversible domain wall motion. Therefore, no significant decrease in hysteresis loss was observed.

It is interesting to note that with the presence of the orthogonal field, smaller applied voltage needed to reach the same strength of internal magnetic field at the main field direction. This is believed to be due to the directional demagnetizing effect. As discussed in section 2.3.1, the demagnetizing field is approximately proportional to the permeability along the field direction. The larger the permeability is, the stronger

demagnetizing field inside the specimen. When two magnetic fields which are perpendicular to each other are applied simultaneously, due to the fixed magnetic moment amplitude per atom, (or per unit volume in a domain), the effective permeability along one direction is smaller than the permeability when only one field is applied. Due to the decrease in the effective permeability along the main field direction, the demagnetizing field inside the specimen is smaller. The external field needed to reach the same internal magnetic field, therefore, decreased with the presence of an orthogonal field. This observation will be discussed again in the next chapter.

## 2.4.2 Measurements on Metglas 2605 amorphous ribbon

### *2.4.2.1 Specimen and experimental method*

Metglas 2605 amorphous ribbon, provided by Allied Signal Corporation, has a composition of  $\text{Fe}_{80}\text{B}_{12}\text{Si}_8$ , and a nominal thickness of 0.020 mm. However, the evaluated thickness based on the material density provided by the vendor and strip mass was 0.0225mm. The ribbon was cut into long strips with dimension 170 x 5 mm. The main magnetic field was applied along the direction of the length and the orthogonal field was applied along the direction of width.

Hysteresis measurements were made using a hysteresis measurement system developed by the Istituto Elettrotecnico Nazionale Galileo Ferraris. In this system, the magnetic field was created by a solenoid and the value of magnetic field was evaluated by computer based on the relationship between current and magnetic field of a solenoid. The magnetic induction was measured through a flux pick-up coil based on Faraday's law. In order to overcome the problem which resulted from the difference between the real cross-

sectional area of specimen and the cross-sectional area of pickup coil, a second identical coil was connected in series with opposite connection so that the cross-sectional area difference can be canceled out. The electromotive force generated in the flux coil was converted into corresponding magnetic induction through the data acquisition board. Specialized for the hysteresis measurement of ribbon, this computerized hysteresis measurement system is one dimensional. In order to evaluate the hysteresis behavior of Metglas ribbon under the action of an orthogonal bias field, an extra orthogonal field was applied during the measurements using an electromagnet.

#### *2.4.2.2 Results and discussion*

Figure 2-20 shows the effect of the orthogonal field on hysteresis loops of an amorphous ribbon measured under fixed applied field amplitude, while Figure 2-21 shows the orthogonal field effect on the same specimen measured under fixed induction amplitude. As observed before, with increasing orthogonal field, the hysteresis loops were rotated, so that the effective permeability ( $B / H_a$ ) decreased as the orthogonal field was increased. Since both orthogonal field and excitation field were strong in this measurement, an increase in the reversible magnetization region where the two branches of a hysteresis curve overlap to each other was observed again. With a strong orthogonal field which magnetized the specimen near saturation along the orthogonal field direction, the increase in magnetization along the main field direction was completed mainly by the reversible domain rotation process which rotated the magnetic moments away from the orthogonal field direction. Therefore, under the action of the strong orthogonal field, a decrease in core loss was expected and was observed as shown in Figure 2-22.

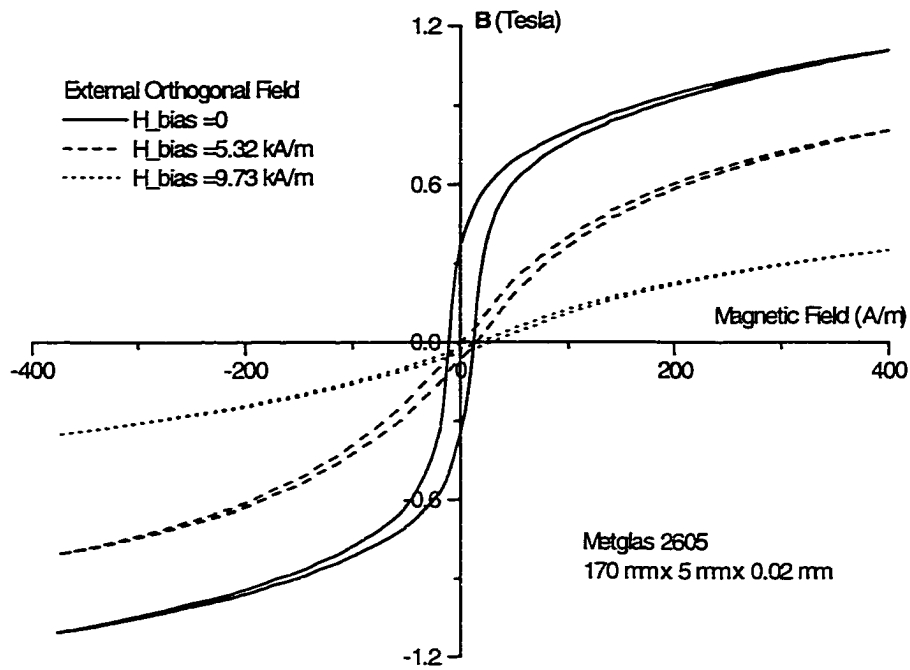


Figure 2-20 The effect of an orthogonal field on hysteresis of an amorphous ribbon in fixed field amplitude measurements.

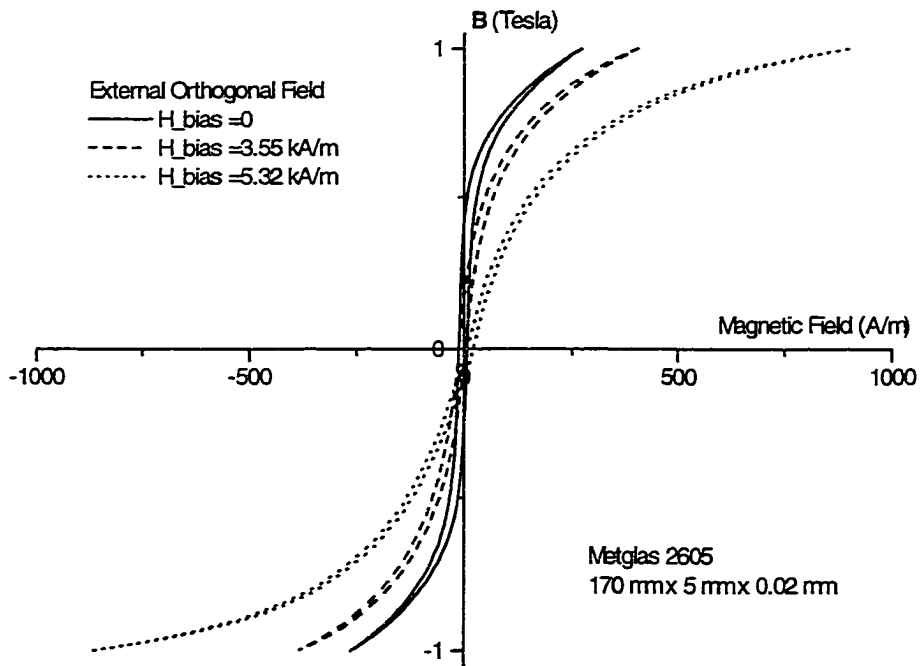


Figure 2-21 The effect of an orthogonal field on hysteresis of an amorphous ribbon in fixed induction amplitude measurements.



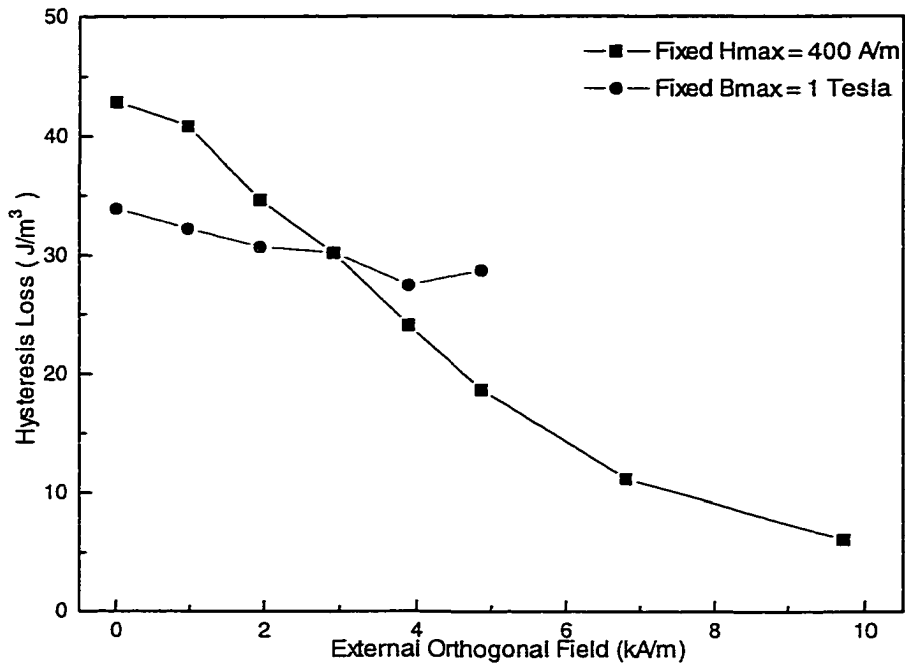


Figure 2-22 The effect of an orthogonal field on hysteresis loss of an amorphous ribbon.

Because of its amorphous microstructure, Metglas 2605 has high permeability, high resistivity and low core loss. The results presented here showed a method for further decreasing core loss of amorphous magnetic materials.

The fact that the orthogonal field effect was observed in conducting magnetic materials indicated that the orthogonal field effect is not unique to the nonconducting ferrite. It appears from the results of this work that it is a general property of isotropic magnetic materials under the action of bi-axial magnetic fields.

## 2.5 Conclusion

In this study, the effect of the orthogonal field was investigated experimentally on different magnetic materials, under different measurement conditions. Hysteresis measurements showed that an orthogonal field rotated the hysteresis loop and reduced the

enclosed area. As a result, the hysteresis loss and the effective permeability along the field direction decreased with increasing orthogonal field. The experimental results on ferrite devices indicated that the orthogonal field reduced the hysteresis loss by increasing the reversible rotation magnetization region. The effect was more pronounced as both excitation field and orthogonal field were increased. The fact that the orthogonal field effect was observed in non-conducting ferrite, conducting polycrystalline silicon iron sheet and conducting amorphous Fe-Si-B ribbon indicated that an orthogonal field effect is a general effect of magnetic materials under the action of bi-axial fields.

### 3. ANISOTROPIC EXTENSION OF HYSTERESIS MODEL

#### 3.1 Introduction

It would be very useful to be able to describe hysteresis mathematically in order to model magnetic properties of ferromagnetic materials. Several classes of hysteresis models have been proposed; these include the Preisach model [15] which is widely used in the magnetic recording industry for describing the magnetization characteristics of recording media, and the Stoner-Wohlfarth model [41] of rotational hysteresis, which only applies to single-domain particle, but has been used for modeling properties of hard magnetic materials. In this study, another class of hysteresis model [26], which is based on energy dissipation, was used as a tool to theoretically investigate the orthogonal field effect. Since it was first proposed in 1984, the hysteresis model has been extended to include stress effects[34, 36, 46], frequency dependence of hysteresis curves on non-conducting magnetic materials[29] and conducting magnetic materials[31], and the hysteresis of anisotropic magnetic materials[33].

Based on the assumption that the orthogonal field introduces anisotropy in isotropic magnetic materials, and the observed fact that the orthogonal field reduced the core loss by increasing the reversible components of magnetization, the classical Jiles-Atherton hysteresis model was extended in this study to model the hysteresis of isotropic magnetic materials under the action of an orthogonal field. The predictions of the extended model agreed well with the experimental results. In this chapter, the development of the orthogonal field extension of the hysteresis model will be discussed.

The comparison between the experimental curves on a ferrite toroid and the modeled curves will be presented.

## 3.2 The isotropic hysteresis model

### 3.2.1 Anhysteretic magnetization

#### 3.2.1.1 *Langevin theory of paramagnetism*

In paramagnetic materials, due to the unpaired electrons there is a net permanent magnetic moment  $m$  per atom, which is the vector sum of the electron spin magnetic moment  $m_s$  and the electron orbit magnetic moment  $m_o$ .

$$m = m_s + m_o.$$

Under the action of a magnetic field, the magnetic moment will align along the direction of field since the direction of field is the energy minimum direction. The energy  $E$  of a magnetic moment  $m$  in the magnetic field  $H$  is:

$$E = -\mu_0 m \cdot H$$

Thermal energy tends to randomize the alignment of the magnetic moment. Under the assumption that there is no interaction among magnetic moments in paramagnetic materials, Langevin[47] used the classical Boltzmann statistics to evaluate the probability  $p$  of any given electron occupying an energy state  $E$  at a temperature  $T$ , which is given by:

$$p(E) = e^{-\frac{E}{k_B T}}$$

The number of magnetic moments lying between angles  $\theta$  and  $\theta + d\theta$  therefore is

$$dn = \frac{N \sin \theta \exp\left(\frac{\mu_0 m H \cos \theta}{k_B T}\right) d\theta}{\int_0^\pi \sin \theta \exp\left(\frac{\mu_0 m H \cos \theta}{k_B T}\right) d\theta}$$

The magnetization  $M$  is the summation of the projection of all these magnetic moments along the direction of magnetic field  $H$ :

$$M = \int_0^N m \cos \theta dn$$

$$M = \frac{Nm \int_0^\pi \cos \theta \sin \theta \exp\left(\frac{\mu_0 m H \cos \theta}{k_B T}\right) d\theta}{\int_0^\pi \sin \theta \exp\left(\frac{\mu_0 m H \cos \theta}{k_B T}\right) d\theta}$$

The integration of above expression gives magnetization of a paramagnetic material as a function of magnetic field and temperature,

$$M = Nm \left[ \coth\left(\frac{\mu_0 m H}{k_B T}\right) - \left(\frac{k_B T}{\mu_0 m H}\right) \right]$$

or

$$M = Nm L\left(\frac{\mu_0 m H}{k_B T}\right) = M_s L\left(\frac{\mu_0 m H}{k_B T}\right)$$

where the  $L(x)$  is Langevin Function.

$$L(x) = \coth(x) - \frac{1}{x}$$

The Langevin model establishes an one-to-one relationship between magnetic field  $H$  and magnetization  $M$  for a paramagnetic material. For  $x \ll 1$ ,

$$L(x) \cong \frac{x}{3}$$

At high temperatures,  $\frac{\mu_0 m H}{k_B T} \ll 1$ , resulting in

$$M = \frac{N \mu_0 m^2 H}{3 k_B T}$$

$$\chi = \frac{M}{H} = \frac{N \mu_0 m^2}{3 k_B T} = \frac{C}{T}$$

This is the Curie law, which states that a paramagnetic susceptibility  $\chi$  varies inversely with the temperature, and has been proven by experiments on paramagnetic materials.

### 3.2.1.2 Weiss mean field theory

For ferromagnetic materials, however, there is coupling among magnetic moments. This coupling, acting as a strong magnetic field, aligns the magnetic moments in a domain parallel to each other. This coupling can be expressed by the Weiss mean field  $H_{weiss}$ , which is proportional to the bulk magnetization  $M$ .

$$H_{weiss} = \alpha M$$

The  $\alpha$ , coupling coefficient, is used to characterize the strength of the coupling among magnetic moments. Under the action of an external magnetic field  $H$ , the effective magnetic field that an individual magnetic moment experienced is:

$$H_e = H + \alpha M$$

where both the effective magnetic field  $H_e$  and magnetization  $M$  are along the direction of the applied field. By replacing the magnetic field  $H$  with the effective magnetic field  $H_e$  in the Langevin model of paramagnetism, the Langevin-Weiss Model, which describes the anhysteretic magnetization of a ferromagnetic material, can be obtained.

$$M = M_s L\left(\frac{\mu_0 m(H + \alpha M)}{k_B T}\right)$$

where the  $M_s$  is the saturation magnetization. Although it is an implicit function, the Langevin-Weiss model also is a single-valued relation between magnetic field  $H$  and magnetization  $M$  for certain values of  $\alpha$  ( $\alpha \leq 3k_B T/\mu_0 M_s$ ) as shown in Figure 3-1 where

$$a = \frac{k_B T}{\mu_0 m}.$$

### 3.2.2 Hysteresis magnetization

Instead of considering the individual magnetic moments in magnetic materials, Jiles and Atherton studied the motion of magnetic domain walls under the action of a magnetic field [26]. This leads to a model for hysteresis which is based on energy

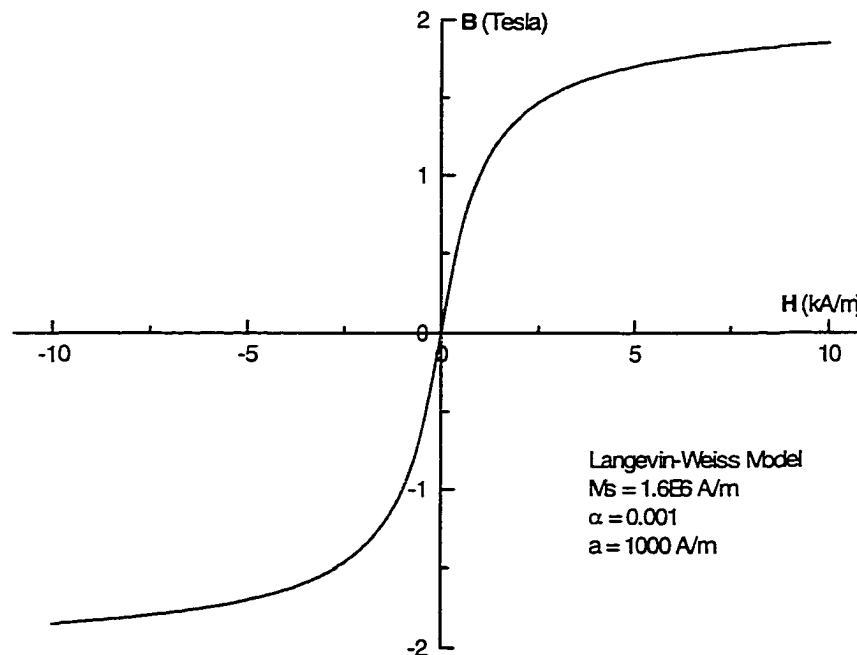


Figure 3-1 Anhyseretic magnetization curve modeled by Langevin-Weiss model.

dissipation. Inside a ferromagnetic material, there is interdomain coupling which can be represented by the mean field parameter  $\alpha$ . The effective magnetic field which each magnetic domain experiences is

$$H_e = H + \alpha M$$

Under the action of a magnetic field, domain walls will move so that the volume of domains aligned favorably with respect to the field direction increases at the expense of the domains aligned unfavorably with respect to the field direction. If a  $180^\circ$  domain wall of area  $A$  moves through a distance  $dx$ , the change in magnetization due to the movement is:

$$dM = 2M_s A dx$$

where  $M_s$  is spontaneous magnetization within a domain. For non- $180^\circ$  domain walls, the change in magnetization is

$$dM = M_s (1 - \cos \theta) A dx$$

But the motion of domain walls is impeded by the pinning sites which result from the imperfection of magnetic materials, such as grain boundaries, dislocations, inclusions and second phases. These defects induce local energy minima when domain walls intersect them. Extra energy is needed for domain walls to overcome the local energy minimum, which results in hysteresis loss. The model assumed that there is homogeneous and isotropic distribution of the pinning sites with pinning site density  $n$  and every pinning site has the same average pinning energy  $\mu_0 \varepsilon_\pi$ . If the domain wall moves a distance  $dx$ , the energy loss due to the domain wall pinning is:

$$dE_{loss} = n \mu_0 \varepsilon_\pi A dx$$

For non- $180^\circ$  domain wall, the energy loss is



$$dE_{loss} = \frac{1}{2} n \mu_0 \epsilon_\pi (1 - \cos\theta) A dx$$

Therefore:

$$dE_{loss} = \frac{\mu_0 n \epsilon_\pi dM}{2M_s}$$

replacing  $(n\epsilon_\pi/2M_s)$  by the constant  $k$  gives

$$dE_{loss} = \mu_0 k dM$$

The equation implies that the energy loss by moving a domain wall is proportional to the changes in magnetization.

In the absence of pinning sites, all energy supplied to the material is equal to the change in magnetostatic energy in the material. This is anhysteretic magnetization. In case of hysteresis, the energy supplied to the material equals the magnetostatic energy plus hysteresis loss. The magnetostatic energy in the material is the energy difference between input energy, which is equal to the anhysteretic energy without pinning, minus the energy loss due to the domain wall pinning.

$$\mu_0 \int M(H_e) dH_e = \mu_0 \int M_{an}(H_e) dH_e - \mu_0 \int k \left( \frac{dM}{dH_e} \right) dH_e$$

Differentiating the integral equation gives,

$$M(H_e) = M_{an}(H_e) - k \left( \frac{dM}{dH_e} \right)$$

Rearranging the above equation yields the form for the susceptibility

$$\frac{dM}{dH_e} = \frac{M_{an} - M}{k}$$

Expressing the effective field  $H_e$  in terms of  $H$  and  $\alpha M$  results in

$$\frac{dM}{dH} = \frac{M_{an} - M}{\delta k - \alpha(M_{an} - M)}$$

where the parameter  $\delta$  takes the value +1 when  $H$  increases in the positive direction,  $dH/dt > 0$ , and -1 when  $H$  increase in the negative direction,  $dH/dt < 0$ , ensuring that the pinning always opposes change in magnetization.

The above differential equation implies that apart from the perturbation due to the coupling of magnetization, expressed through the coefficient  $\alpha$ , the rate of change of magnetization  $M$  with field is proportional to the displacement from the anhysteretic,  $M_{an} - M$ .

It should be noted that the above differential equation represents only the irreversible component of magnetization. The above equation can be rewritten as:

$$\frac{dM_{irr}}{dH} = \frac{M_{an} - M_{irr}}{\delta k - \alpha(M_{an} - M_{irr})}$$

During magnetization, there is also a reversible component of magnetization, which could be reversible domain wall bowing, reversible translation of domain walls or reversible domain rotation. The reversible component  $M_{rev}$  of magnetization was assumed to be proportional to the difference between the anhysteretic magnetization  $M_{an}$  and irreversible magnetization  $M_{irr}$  with a constant proportionality which is called reversibility coefficient  $c$ .

$$M_{rev} = c (M_{an} - M_{irr})$$

The total magnetization  $M$  is the sum of reversible magnetization and irreversible magnetization.

$$M = M_{rev} + M_{irr} = (1 - c) M_{irr} + c M_{an}$$

where the constant coefficient  $c$  ranges from 0 (completely irreversible magnetization) to 1 (completely reversible magnetization). The Jiles-Atherton model which includes both irreversible and reversible magnetization can be expressed alternatively as

$$\frac{dM}{dH} = (1-c) \frac{(M_{an} - M)}{\delta k - \alpha(M_{an} - M)} + c \frac{dM_{an}}{dH}$$

After solving the first order differential equation numerically, a sigmoid-shaped hysteresis loop can be obtained. Through changing the parameters, this model is able to model the magnetization of soft magnetic materials, hard magnetic materials and anhysteretic magnetization. Figure 3-2 shows three typical modeled hysteresis curves.

One of the basic foundations of the Jiles-Atherton model was that the energy loss is proportional to the change in magnetization. Although it was derived from the domain wall motion under the action of a magnetic field, it does not have to be limited the

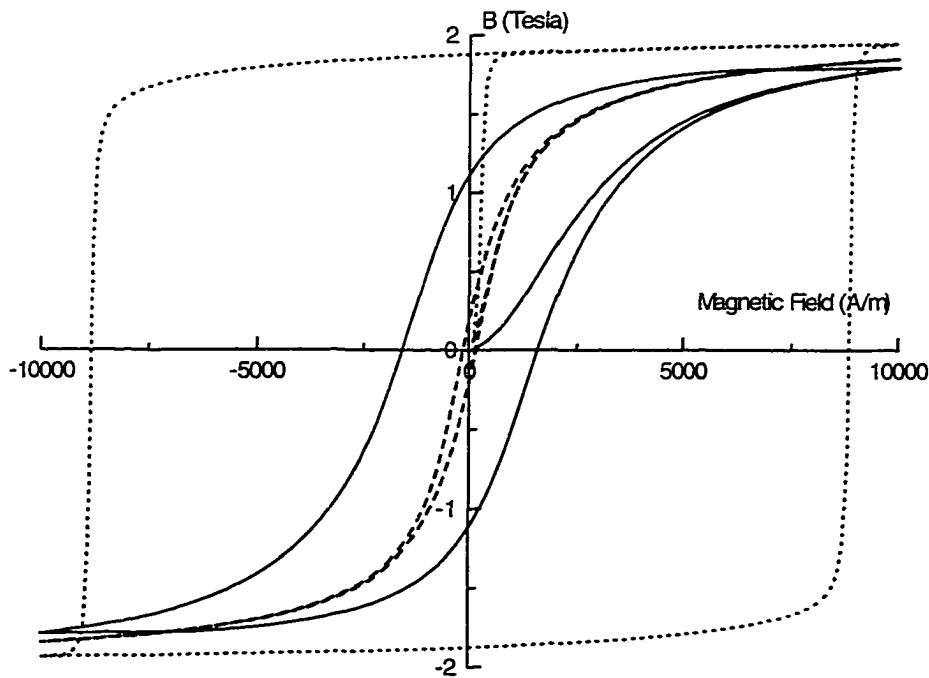


Figure 3-2 Hysteresis curves modeled by the Jiles-Atherton model.

domain wall motion magnetization and therefore the model applies to any situation in which the energy loss is proportional to change in magnetization as could occur also under domain rotation.

Although Jiles-Atherton model is based on the anhysteretic magnetization which is determined as the global energy equilibrium under the action of a magnetic field, it does not limit the form of the anhysteretic magnetization curve to that given by the Langevin-Weiss equation. Any model of the anhysteretic magnetization can be incorporated into the general hysteresis model. It is this point which provides scope for extension of the hysteresis model to different magnetic materials, such as crystal anisotropy magnetic materials[33], and to the orthogonal field effect.

### **3.3 Extension for the orthogonal field effect**

In this thesis, the magnetization, under which magnetic field and magnetic induction are in the same direction, is called one-dimensional magnetization. For isotropic magnetic materials, if only one field is applied beginning from demagnetizing state, magnetization is always along the field direction. The magnetization state in which magnetization and magnetic field are antiparallel, is still considered as one-dimensional magnetization since we can think the antiparallel magnetization as negative parallel magnetization.

In one-dimensional magnetization, the magnetization depends on not only the applied magnetic field but also on the history of field exposure. But the direction of the magnetization is known. With an appropriate scalar hysteresis model, such as Jiles-Atherton model, we can evaluate magnetization at different magnetic field strengths.

On the other hand, the magnetization, under which a magnetic material experiences two magnetic fields which are not in the same direction but are in the same plane, is called two-dimensional magnetization in this thesis. Due to the nonlinearity of magnetic materials the vector superposition principle for linear system is no longer valid in a two-dimensional magnetization. The total magnetization is no longer proportional to the vector sum of two magnetic fields. Additionally due to the hysteresis of magnetic materials, the magnetization is even no longer along the direction of the vector sum of the two magnetic fields. From the perspective of hysteresis modeling, the uncertainty on the direction of magnetization significantly increases the difficulty of modeling. The common method, which simply scales a scalar model to two or three dimensions based on the superposition principle of a linear system, can not be used in two-dimensional magnetization problem due to both nonlinearity and hysteresis of a ferromagnetic system.

The energy of a magnetic moment in a magnetic field can be expressed by the following expression:

$$E = -\mu_0 m \cdot H$$

In the presence of two magnetic fields, considering the coupling between magnetic moments, the energy of a magnetic moment in a ferromagnetic material can be written as:

$$E = -\mu_0 m \cdot (H_1 + \alpha M + H_2)$$

The magnetization  $M$  is a vector which has magnitude and direction. As discussed in the Langevin-Weiss model, the magnetization is determined by the energy. However, the energy is also affected by the magnetization. For the one-dimension magnetization case, since we know the direction of magnetization, we can overcome this inter-linking by an iterative method. For the two-dimensional magnetization, however, we have two

unknowns which are also dependent on each other in a nonlinear and hysteretic way. The modeling of two-dimensional magnetization for ferromagnetic materials is therefore very difficult.

### 3.3.1 Anisotropy induced by an orthogonal field

Although the measurements on the orthogonal field effect performed in this study also involved two magnetic fields in two directions, the magnetization was only measured along the direction of the excitation field, while the orthogonal bias field was fixed and normal to the direction of excitation field. At the absence of the excitation field, the orthogonal field magnetizes the isotropic magnetic material along the orthogonal field direction. For one who is in another direction, the magnetic moments in the isotropic specimen is found to have a preferred orientation along the orthogonal field direction. The anisotropic orientation of course is the system response to the orthogonal field. Clearly, the anisotropy energy associated with the orthogonal orientation of magnetic moments is the energy of a magnetic moment in the orthogonal field  $H_{\perp}$ .

$$E_{anisotropy} = -\mu_0 \mathbf{m} \cdot \mathbf{H}_{\perp}$$

This anisotropy energy will alter the anhysteretic magnetization as well as hysteresis of isotropic magnetic materials. Considering the coupling between magnetic moments in a ferromagnetic material, the energy of a magnetic moment in the two fields is:

$$E = -\mu_0 \mathbf{m} \cdot (\mathbf{H}_{\parallel} + \alpha \mathbf{M} + \mathbf{H}_{\perp})$$

The magnetization  $\mathbf{M}$  is a vector which has the parallel component  $\mathbf{M}_{\parallel}$  along excitation field direction and the orthogonal component  $\mathbf{M}_{\perp}$ , along the orthogonal field direction, respectively.

$$E = -\mu_0 \mathbf{m} \cdot (\mathbf{H}_{\parallel} + \alpha \mathbf{M}_{\parallel} + \mathbf{H}_{\perp} + \alpha \mathbf{M}_{\perp})$$

The two components are also dependent on each other since a magnetic material ultimately has a limit on the magnitude of the total magnetic moment given by the saturation magnetization,  $M_S = N m$ , where the  $m$  is the magnitude of each magnetic moment and the  $N$  is the number density of magnetic moments. If one of two magnetic fields is strong and the saturation is reached, we can have the following equation.

$$|\mathbf{M}_{\parallel} + \mathbf{M}_{\perp}|_{H \rightarrow \infty} = M_S$$

However, considering the fact that what was measured and what we are concerned with was the magnetization components along the excitation field direction, for a small orthogonal field, we can approximately consider the orthogonal magnetization  $\mathbf{M}_{\perp}$  independent on the parallel magnetization  $\mathbf{M}_{\parallel}$ , and treat the orthogonal field  $\mathbf{H}_{\perp}$  and the associated magnetization  $\mathbf{M}_{\perp}$  as an anisotropy in a magnetic material. The corresponding anisotropy energy is

$$E_{orthogonal} = -\mu_0 \mathbf{m} \cdot (\mathbf{H}_{\perp} + \alpha \mathbf{M}_{\perp})$$

The total energy of a magnetic moment in a ferromagnetic material can be expressed as,

$$E = -\mu_0 \mathbf{m} \cdot (\mathbf{H}_{\parallel} + \alpha \mathbf{M}_{\parallel}) + E_{orthogonal} = -\mu_0 \mathbf{m} \cdot (\mathbf{H}_{\parallel} + \alpha \mathbf{M}_{\parallel} + \mathbf{H}_{\perp}^e)$$

where  $\mathbf{H}_{\perp}^e$  is called the effective orthogonal field analogous to that used in the Langevin-Weiss model and the classical Jiles-Atherton model. After treating the magnetization resulting from the orthogonal field as an independent anisotropy, we degrade the two-dimensional magnetization to one-dimensional problem, so that we can solve the relationship between the applied excitation field  $\mathbf{H}_{\parallel}$  and the magnetization  $\mathbf{M}_{\parallel}$  along the field direction using an one dimensional hysteresis model, such as Jiles-Atherton model.

The orthogonal field now acts as an anisotropy in affecting the magnetization in the direction of the excitation field.

In one-dimensional magnetization of isotropic magnetic materials, due to symmetry, the integral about the magnetic moment distribution can be evaluated analytically. After introducing the orthogonal anisotropy, however, the two dimensional integral is no longer analytically integrable. In order to determine the anhysteretic magnetization, a spatial summation was made in this study as formulated in the following equation[32].

$$M_{an} = M_S \frac{\sum_{\text{all moments}} e^{\frac{-E}{k_B T}} \times \cos\theta}{\sum_{\text{all moments}} e^{\frac{-E}{k_B T}}}$$

After obtaining the anhysteretic magnetization which is affected by the orthogonal field, the Jiles-Atherton model can be used to model the hysteresis curve of isotropic magnetic materials under the action of an orthogonal field.

$$\frac{dM}{dH} = (1-c) \frac{(M_{an} - M)}{\delta k - \alpha(M_{an} - M)} + c \frac{dM_{an}}{dH}$$

Figure 3-3 shows modeled hysteresis curves which treat the orthogonal field as an anisotropy energy affecting hysteresis of isotropic magnetic materials.  $H_{\text{bias}}$  is the effective orthogonal field. For comparison, a hysteresis loop with the same parameters without an orthogonal field was also plotted. As observed in the experimental results, the modeled loop also rotated clockwise with increasing effective orthogonal field. As a result, the permeability extracted from the modeled curve is expected to decrease with increasing orthogonal field. Since the orthogonal anisotropy has its easy axis in the orthogonal field direction, it was difficult to magnetize the material along a direction



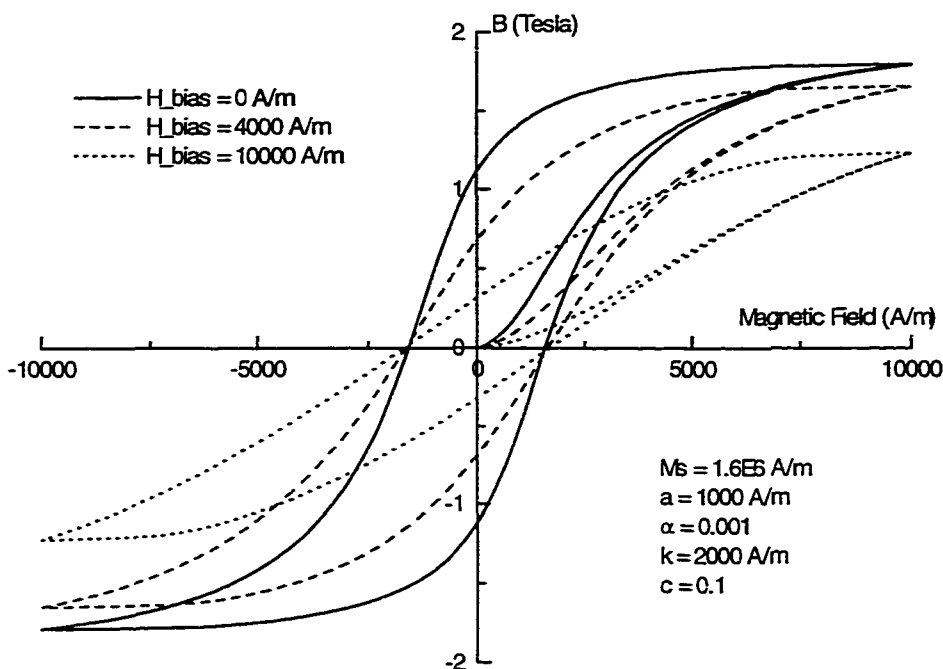


Figure 3-3 Modeled hysteresis loops under the action of an orthogonal field.

normal to the easy axis. The hysteresis loops were, therefore, apparently rotated clockwise. However, the modeled hysteresis loop failed to predict the shrinkage of hysteresis loop at the coercivity points under the action of an orthogonal field as observed in experimental results.

Although the extended hysteresis model successfully modeled the rotation of hysteresis loop under the action of an orthogonal field, the fact that the modeled hysteresis loop failed to predict the shrinkage of hysteresis loop at the coercivity points indicated that for modeling orthogonal field effect, only introducing the orthogonal anisotropy energy into a domain wall motion model was not sufficient to characterize the complete orthogonal field effect of isotropic magnetic materials.

### 3.3.2 Reversible magnetization at the presence of an orthogonal field

The hysteresis loop plotted in Figure 3-3 was modeled by the extended Jiles-Atherton model. The extension was implemented by incorporating the anisotropy energy into the classical model. In the classical model, the reversible magnetization was assumed to be proportional to the difference between irreversible magnetization and anhysteretic magnetization. The coefficient of proportionality is constant and is called domain wall reversibility coefficient  $c$ .

$$M_{\text{rev}} = c (M_{\text{an}} - M_{\text{irr}})$$

The total magnetization is the sum of reversible magnetization and irreversible magnetization.

$$M = M_{\text{rev}} + M_{\text{irr}} = (1-c) M_{\text{irr}} + c M_{\text{an}}$$

Since  $c$  is a constant, the above expression implies a constant fraction of the difference between anhysteretic magnetization and total magnetization. If one only incorporates the orthogonal anisotropy into the model, this implies that the orthogonal field has no effect on the ratio between irreversible and reversible magnetization. This is believed to be the reason that the modeled hysteresis curve failed to show the decrease in coercivity observed in experimental results.

As discussed in Chapter 2, experimental results on the orthogonal field effect showed that the orthogonal field reduced hysteresis loss by increasing the reversible domain rotation magnetization region. This result indicated that the portion of reversible magnetization increase with increasing orthogonal field. In fact, measurements by Atherton and Schonbachler [48] on the reversible magnetization components showed that

the ratio of reversible differential permeability to the total differential permeability increased monotonically with the magnetization.

Considering the above facts, in this study, the reversibility coefficient  $c$  was assumed to change with magnetic field in the following form, which is derived from a normal or Gaussian distribution curve,

$$c_{re} = c + (1-c)(1 - e^{-\left(\frac{H}{\Delta H}\right)^2})$$

where the  $\Delta H$  was called the irreversible field range in this study. The applicability of this form was then tested against experimental results in this study.

It should be noted that there is no clear distinction between reversible magnetization and irreversible magnetization. It is believed that with increasing magnetic field, the irreversible magnetization gradually decreased while the reversible magnetization gradually increased until complete reversible magnetization occurs at high fields. The increase in reversible magnetization was assumed to be in the form of a Gaussian function according to the above equation. The reversibility coefficient  $c_{re}$  varies from  $c$  to 1 depending on the magnetic field  $H$  and the width of the irreversible field range  $\Delta H$  as shown in Figure 3-4.

If the irreversible field range  $\Delta H$  is smaller, with increasing magnetic field, the irreversible magnetization disappears faster and complete reversible magnetization is achieved faster. Correspondingly the reversibility coefficient  $c_{re}$  increased to 1 quicker. On the other hand, if the irreversible field range  $\Delta H$  is large, the reversible component of total magnetization slowly increases and the reversibility coefficient  $c_{re}$  might not increase to 1 within the range of applied magnetic field. The limiting case is that the

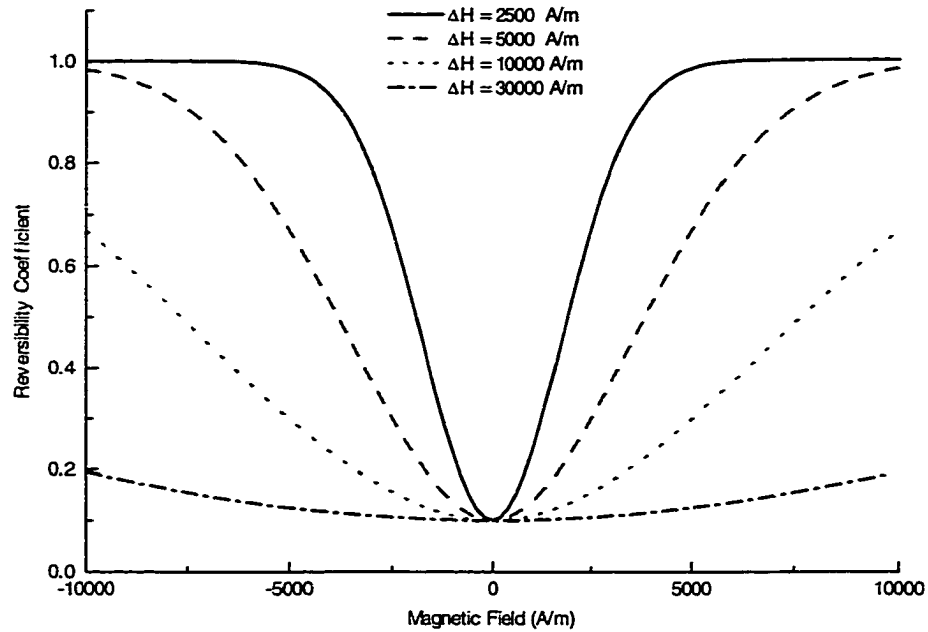


Figure 3-4 The reversibility coefficient under various irreversible field ranges.

irreversible field range is infinite, the reversibility coefficient  $c_{re}$  will then remain constant as proposed in the classical Jiles-Atherton model.

Figure 3-5 shows the effect of the irreversible field range on a hysteresis curve without an orthogonal field. Generally speaking, compared with the hysteresis loop with constant reversibility, the width of the hysteresis loop in the high field region is reduced since the reversible component of total magnetization dynamically increases during the magnetization process.

In the presence of an orthogonal field, the magnetic field experienced by a magnetic material is the vector sum of two magnetic fields. Although the orthogonal field was only considered as an anisotropy in using the extended Jiles-Atherton model, the vector sum of two magnetic fields should be incorporated in evaluating the reversibility coefficient  $c_{re}$ , because the experimental results showed that the orthogonal field reduced

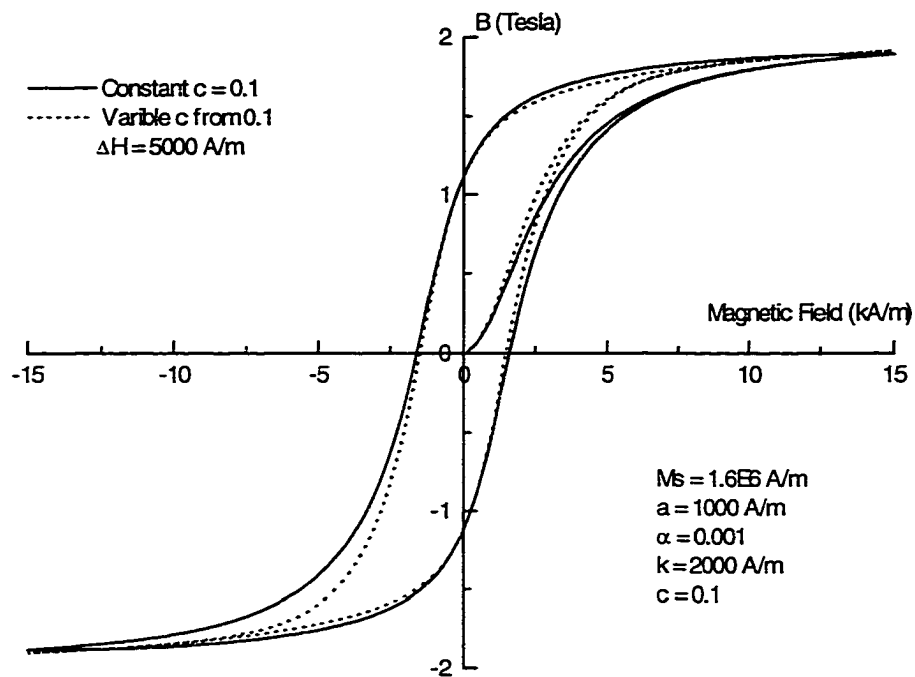


Figure 3-5 The effect of a dynamic reversibility coefficient on a hysteresis curve.

the hysteresis loss by increasing the range of reversible domain rotation. Figure 3-6 shows the modeled hysteresis loops under the action of an orthogonal fields after incorporating the dynamic reversibility coefficient  $c_{re}$ . Compared with the experimental results shown in Figure 2-2, all features experimentally observed are exhibited in the modeled hysteresis curves. With increasing orthogonal field, the hysteresis loops were rotated clockwise and the area of hysteresis loop was decreased until it became a straight line.

Figure 3-7 shows the modeled hysteresis loop under the action of an orthogonal field of 6000A/m when a magnetic material was magnetized to the same magnetic induction level. The hysteresis loop is elongated along the H axis with reversible magnetization. This phenomenon was actually observed in the experiments performed on the long ferrite toroid device as shown in Figure 2-7.

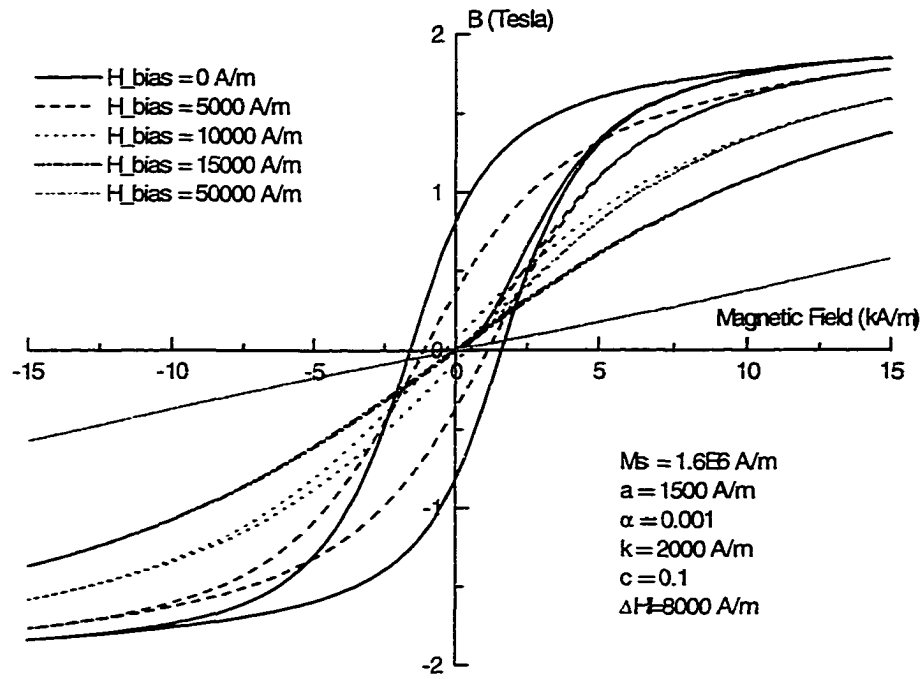


Figure 3-6 Modeled hysteresis curves under the action of orthogonal fields.

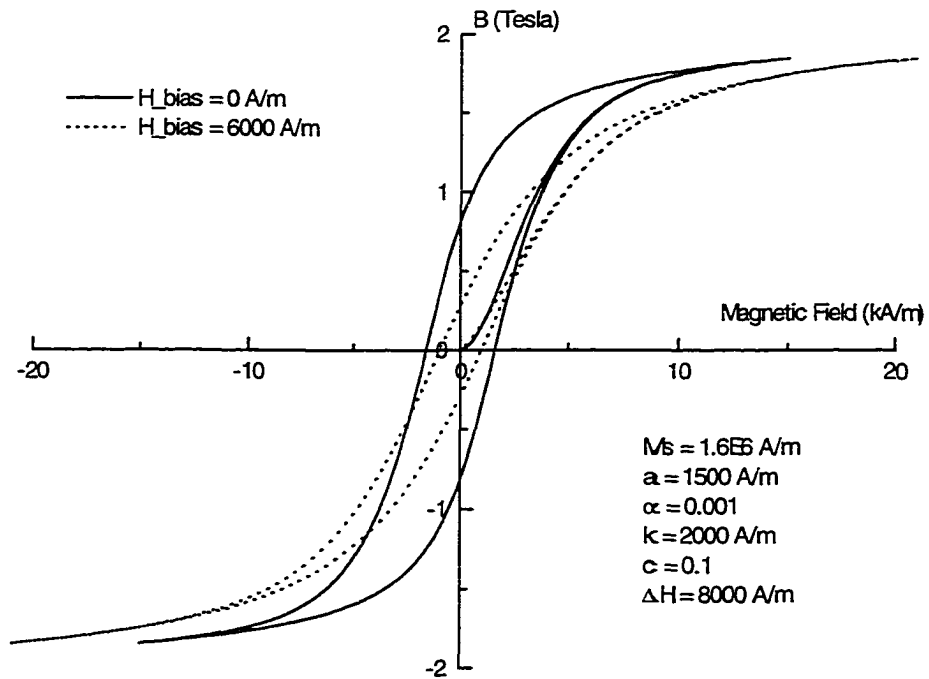


Figure 3-7 Modeled hysteresis loop under the action of an orthogonal field.

In summary, by introducing a dynamically increasing reversibility coefficient  $c_{re}$ , which can be characterized by its irreversible field range, into the extended Jiles-Atherton model, reversible domain rotation mechanism under the action of an orthogonal field can be incorporated into the model. Therefore, the extended Jiles-Atherton model can describe both domain wall motion and domain rotation resulting from the action of an orthogonal field, and has been used to successfully model changes of hysteresis curves under the action of an orthogonal field.

### **3.4 Modeling of experimental results**

As discussed in Chapter 2, for a toroidal structure, if the excitation field is applied along the circumferential direction and the orthogonal field is applied along the axis direction, two magnetic fields will be perfectly orthogonal to each other. Therefore a toroid is an ideal specimen geometry for the experimental and theoretical study of the orthogonal field effect.

For the modeling of the orthogonal field effect, it is necessary to determine the values of two magnetic fields and the magnetic induction along the circumferential direction. For toroidal structures, magnetic induction along the circumferential direction can be measured by a flux coil and the excitation field along the circumferential direction can be evaluated from the excitation current as discussed in chapter 2. The orthogonal field along the toroid axis direction, however, was difficult to evaluate due to the demagnetizing effect.

### 3.4.1 Evaluation of the internal orthogonal bias field

Due to the demagnetizing effect which is associated with the magnetization of a specimen with a finite length along the field direction, the actual orthogonal field experienced magnetic material inside the specimen is less than the external applied magnetic field.

$$H_{\perp} = H_{\perp a} - N_d M_{\perp}$$

where  $N_d$  is demagnetizing factor along the orthogonal field direction. Except for elliptic specimens whose demagnetizing factor can be obtained analytically, the demagnetizing factors of most specimens have to be determined numerically. Considering the relationship between magnetic field and magnetization, the internal orthogonal field can also be expressed as

$$H_{\perp} = H_{\perp a} - N_d \chi_{\perp} H_{\perp}$$

rearranging the equation gives the relation between the applied orthogonal field and the internal orthogonal field,

$$H_{\perp} = \frac{H_{\perp a}}{1 + N_d(\mu_{\perp} - 1)} \approx \frac{H_{\perp a}}{N_d \mu_{\perp}}$$

This equation indicates that the internal orthogonal field is inversely proportional to the permeability. Since the ferrite materials usually have a relative permeability of a few thousands, the internal orthogonal field is only a small fraction of the external applied orthogonal field.

For two-dimensional magnetization, however, the permeability in one direction itself is dependent on the magnetization in another direction since magnetic materials have an upper limit to their magnetic moments. In the presence of two magnetic fields,



magnetization will point at a direction somewhere between directions of two applied magnetic fields. Magnetization in one direction is the projection of the total magnetization along the direction. Since the permeability is the ratio of magnetic induction to magnetic field, the component of permeability along one direction is also the projection of the total permeability. The permeability along the orthogonal field direction can therefore be expressed by[49],

$$\mu_{\perp} = \frac{\mu_{R0}}{\sqrt{1 + \left(\frac{H}{H_{\perp}}\right)^2}}$$

where the  $\mu_{R0}$  is the relative permeability of the magnetic material when only one magnetic field is present. The above expression indicates that the orthogonal permeability is dependent on both excitation field and orthogonal field. As a result, the orthogonal permeability, and the internal orthogonal field will change during the magnetization process even with a fixed external orthogonal field. Solving the above equation with the internal orthogonal field gives

$$H_{\perp} \approx \sqrt{\frac{H_{\perp 0}^2 + \sqrt{H_{\perp 0}^4 + 4H_{\perp 0}^2 H^2}}{2}} = H_{\perp 0} \sqrt{\frac{1 + \sqrt{1 + 4H^2/H_{\perp 0}^2}}{2}}$$

where

$$H_{\perp 0} = \frac{H_{\perp a}}{N_d \mu_{R0}}$$

is called the initial internal orthogonal field which is the internal orthogonal field when the excitation field is zero.

This shows that the internal orthogonal field inside the specimen is not a constant. Instead, it dynamically increased from an initial internal orthogonal field with increasing

excitation field. Since the orthogonal field rotates the hysteresis loops clockwise and the internal orthogonal field inside the specimen increased during magnetization process, it is expected that the portion of hysteresis loop at high field region has larger rotation than that at low field region. Since the proposed reversibility coefficient increased with both excitation field and orthogonal field, the increase in the internal orthogonal field due to the coupled demagnetizing effect will further increase the reversibility coefficient. The width of hysteresis loop under the action of an orthogonal field is expected to be reduced further due to the coupled demagnetizing effect.

The  $H_{10}$ , the internal orthogonal field at zero excitation field, has to be determined numerically. In this study, considering the axial symmetry of the toroid, 2D finite element modeling was used to evaluate the  $H_{10}$ . As discussed in Chapter 5, inside the specimen, the  $H_{10}$  was actually not uniformly distributed. For the purpose of hysteresis modeling, a spatial averaging was taken to represent the internal orthogonal field along the axial direction of the toroid. According to the linear FEM analysis on the long ferrite toroid with a relative permeability of 2100, at the absence of the excitation field, an external orthogonal field of 15.9A/m corresponds to an internal orthogonal field of 59A/m.

### 3.4.2 Modeling and discussion

First, the extended Jiles-Atherton model was used to characterize the experimental hysteresis loop, as shown in Figure 2-6, of a long ferrite toroid without an orthogonal field through the curve fitting. As shown in Figure 3-8, the solid line was the experimental hysteresis curve on the long ferrite toroid while the dotted line was the modeled hysteresis curve using the extended Jiles-Atherton model.

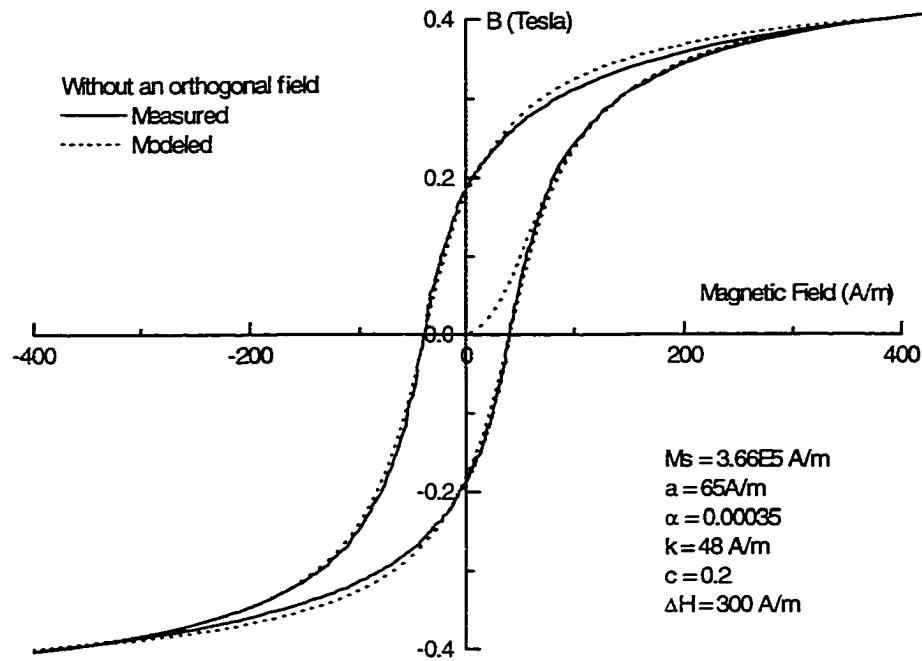


Figure 3-8 Hysteresis modeling without an orthogonal field.

Considering the facts that the internal orthogonal field was small and the applied orthogonal field was constant, a linear relationship between the orthogonal magnetization component and the internal orthogonal field was approximately assumed, so that the effective orthogonal field can be expressed by the internal orthogonal field.

$$H_{\perp}^e = H_{\perp} + \alpha M_{\perp} = H_{\perp}(1 + \alpha\chi)$$

Where the susceptibility  $\chi = 2100$  which was obtained from the experimental data on the long ferrite toroid specimen. Considering the directional demagnetizing effect, the effective orthogonal field for the modeling of orthogonal field effect was

$$H_{\perp}^e = H_{\perp 0}(1 + \alpha\chi) \sqrt{\frac{1 + \sqrt{1 + 4H^2/H_{\perp 0}^2}}{2}}$$

After introducing an initial internal orthogonal field  $H_{L0}$  of 69 A/m into the extended Jiles-Atherton model, the modeled hysteresis loop with an orthogonal field successfully fitted the experimental hysteresis loop under the action of an external orthogonal field of 15.9 KA/m as shown in Figure 3-9.

As presented in Chapter 2, hysteresis measurements were also made so that the long ferrite toroid specimen under the action of an orthogonal field was magnetized to the same magnetic induction level as shown in Figure 2-7 The experimental results showed that the orthogonal field effect reduced by extending reversible magnetization region. As shown in Figure 3-10, the extended Jiles-Atherton model also exhibited this feature.

In order to visualize the orthogonal field effect on the modeled hysteresis curves, two hysteresis curves, with and without the initial orthogonal field of 69A/m, are plotted again in Figure 3-11. Compared the experimental curves in Figure 2-6 to the modeled

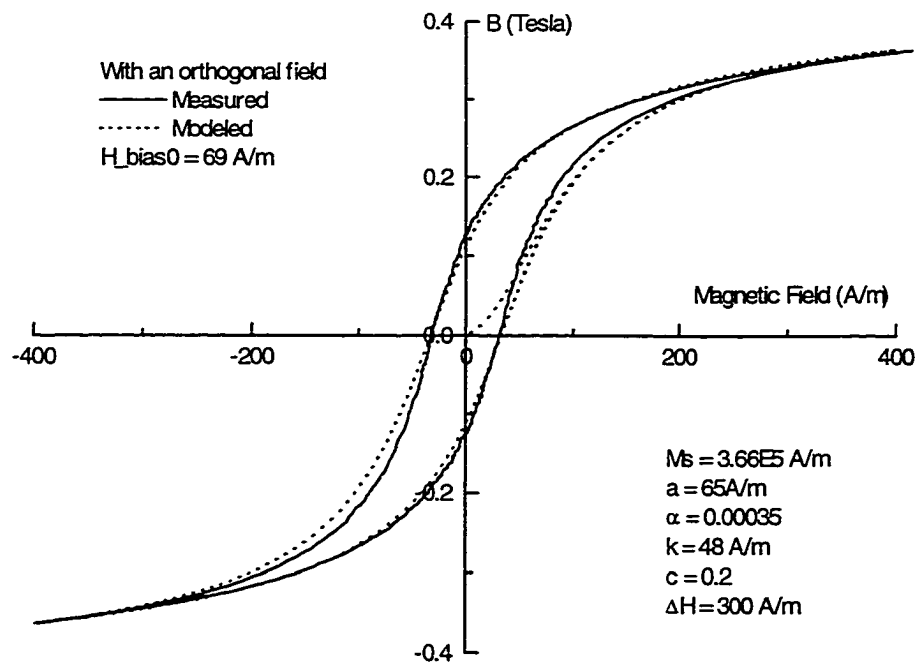


Figure 3-9 Hysteresis modeling with an internal orthogonal field of 69 A/m.

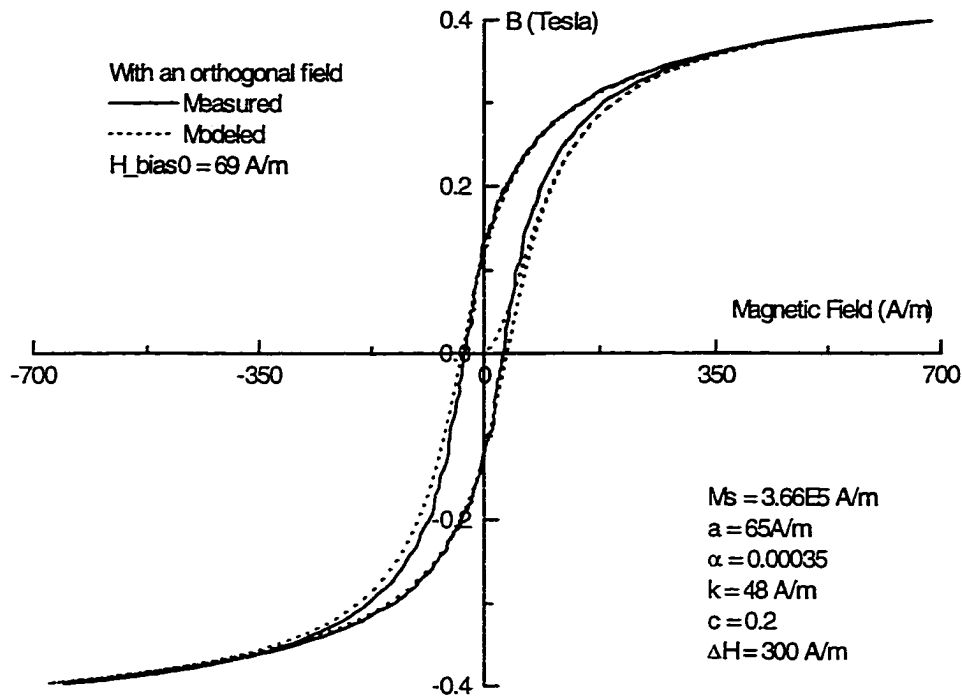


Figure 3-10 Hysteresis modeling with an orthogonal field.

hysteresis curves in Figure 3-11, the difference is indistinguishable.

However, the initial internal orthogonal field evaluated by the 2D linear FEM was 59 A/m, instead of 69 A/m in the hysteresis modeling. The difference is believed to result from the following facts:

1. The orthogonal magnetization  $M_{\perp}$  was assumed to be a fixed orthogonal anisotropy and independent of the parallel magnetization  $M_{\parallel}$ . This approximation was good only when orthogonal field was small and the excitation field was not very strong.
2. The distribution of the internal orthogonal field along the direction of the toroid axis was not uniform as shown in Figure 5-2. The non-uniform field distribution was replaced by a spatial mean value for the propose of hysteresis modeling.

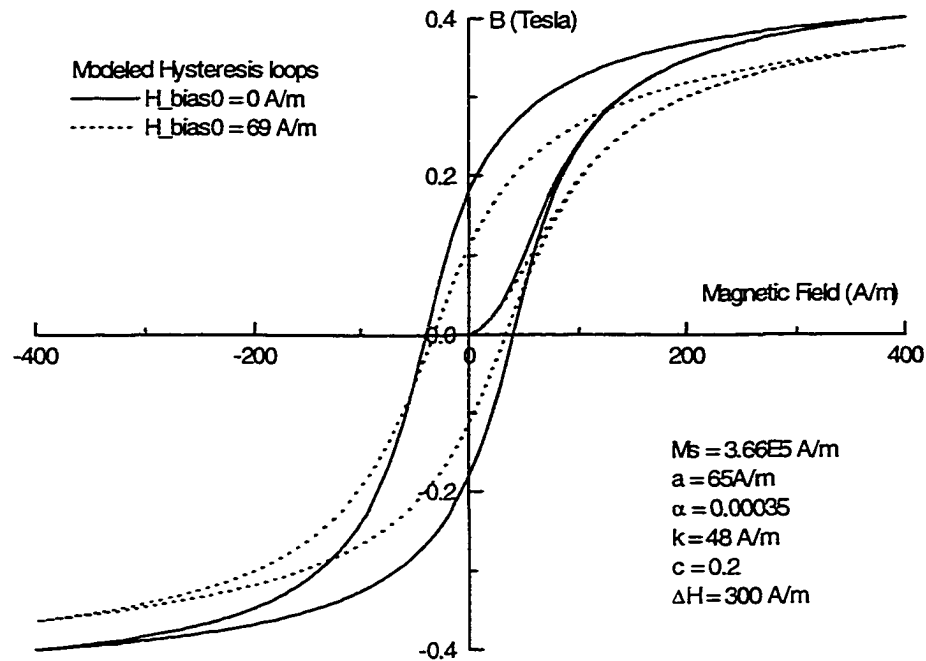


Figure 3-11 Modeled hysteresis curves with and without an orthogonal field.

### 3.5 Conclusion

Derived from the domain wall motion of magnetization and based on isotropic Langevin-Weiss anhysteretic magnetization model, the Jiles-Atherton model has previously been used to successfully model hysteresis in both soft and hard magnetic materials.

In the present work, the extension of this one-dimensional isotropic model to quasi-two-dimension magnetization has been investigated. The orthogonal field was considered as an anisotropy in affecting one-dimension anhysteretic magnetization so that the well developed one-dimension Jiles-Atherton model can be used to model the orthogonal field effect. Although the modeled hysteresis loops successfully modeled the

experimentally observed loop rotation under the action of an orthogonal field, the fact that the modeled hysteresis loop failed to show the observed decrease in hysteresis loss and coercivity indicated that the dynamically increased reversible domain rotation should also be incorporated into the extended Jiles-Atherton model.

Based on these experimental observations, a dynamically variable reversibility coefficient, which models the change in reversibility coefficient  $c$  during the magnetization process and is characterized by the irreversible field range, was proposed to take into account the reversible domain rotation magnetization. After incorporating the variable reversibility coefficient into the extended Jiles-Atherton model, the modeled hysteresis loops under the action of an orthogonal field effect showed all the experimentally observed features.

Due to the strong demagnetizing effect, the internal orthogonal field inside a ferrite toroid along the axial direction was only a small fraction of the external orthogonal field. Also with the fixed magnitude of magnetic moments in magnetic materials, the coupled demagnetizing effect caused the internal orthogonal field to dynamically increase with increasing excitation field. After incorporating the increased internal orthogonal field into the extended Jiles-Atherton model, the modeled hysteresis curves showed agreement with experimental results.

## **4. APPLICATIONS OF THE ORTHOGONAL FIELD EFFECT**

In this chapter, measurements and discussion of two prototype magnetic devices will be presented. This work was a part of verification study for the research sponsor, Rockwell Collins, Avionics and Communications Division.

### **4.1 Introduction**

While there has been rapid advancement in the data storage and signal processing sides of the microelectronics industry, the power supply side had lagged far behind so that power supply technology in use in computers today is hardly different from that used in the 1970's. One of key factors is the size and energy conversion efficiency of devices, such as transformers, inductors or motors. With the development of various technologies, all devices in electronics systems are being rapidly miniaturized, except the inductive devices which are the last and most difficult for miniaturization. The reason is the energy storage density of a magnetic device. In industrial applications, core loss is one of the key factors in the design of a magnetic power device. In order to avoid the excessive core loss of a magnetic device, the maximum magnetic induction in a magnetic circuit should be well below the saturation level. As a result, either the overall dimensions have to be increased to transfer or store more power, or the capacity of the power storage has to be compromised. Since the experimental results on various magnetic materials showed that core loss was reduced under the action of an orthogonal field, the orthogonal field effect could be used to improve the energy efficiency, or the energy storage density of a magnetic device.



In an electronics system, it is desirable that characteristic properties of devices can be adjusted electrically to cope with the change in load or environments. Nowadays, with the development of semiconductors, two of three classes of major passive electronic devices are already electronically variable. Such as electronic variable resistor and electronically variable capacitance diode, which actually are semiconductor devices. The inductive device, such as inductor and transformer, is the only major type which is not electronically controllable. This type of device has to be very carefully designed and manufactured before being assembled on the circuit board. Once assembled on the board, its performance can only be adjusted either mechanically, such as changing the location of a part of the magnetic circuit, or indirectly, such as change the capacitance of a capacitor in some resonant circuits.

However the experimental results on the orthogonal field effect showed the effective permeability of a magnetic device can be tailored by changing the current which creates the orthogonal field. It is therefore possible to change the inductance of an inductor by varying the orthogonal field.

#### **4.2 Inductor controlled by an orthogonal field**

As discussed in chapter 2, due to strong demagnetizing effect, the internal orthogonal field along the axial direction of long toroid is only a small fraction of the external orthogonal field. As a result of the demagnetizing effect, only slight hysteresis loop rotation and shrinkage were observed in the measurements on the long ferrite toroid. In order to enhance the orthogonal field effect, a device with a small demagnetizing effect

along the orthogonal field direction is desirable. The best option is to have a closed magnetic circuit along the orthogonal field.

For the results presented in Chapter 2, the orthogonal field was produced by a separate device, an external solenoid or a magnet. For a practical power electronics application, it is also desirable to have both of magnetic fields created by coils on one magnetic device. One way to implement this is to wind a set of coil outside the long ferrite toroid along the axis direction. Due to the demagnetizing effect, the effective orthogonal field inside the toroid would not be sufficiently high. To avoid the demagnetizing effect, a closed magnetic circuit should be provided for the orthogonal field.

#### 4.2.1 Design of closed circuit device

Based on the idea of providing closed magnetic circuit for both main field and orthogonal field in order to avoid the demagnetizing effect so that a high orthogonal field can be obtained, a circular button shape device was proposed as shown in Figure 4-1.

After fabrication by Rockwell Collins, main coil, orthogonal coil and flux coil were wound on the button device as shown in Figure 4-1. For inductance measurements, the main coil consisted of two 8-turn coils connected in series on the arms of the horizontal path, while the orthogonal coil consisted of two 8-turn coils connected in series on the arms of the vertical path. For hysteresis measurements, the main coil was re-wound so that the main coil consisted of two 4-turn coils and the flux coil, which consisted of two 3-turn coils connected in series, was added. In the center region of the device, the main field and orthogonal field were orthogonal to each other. The

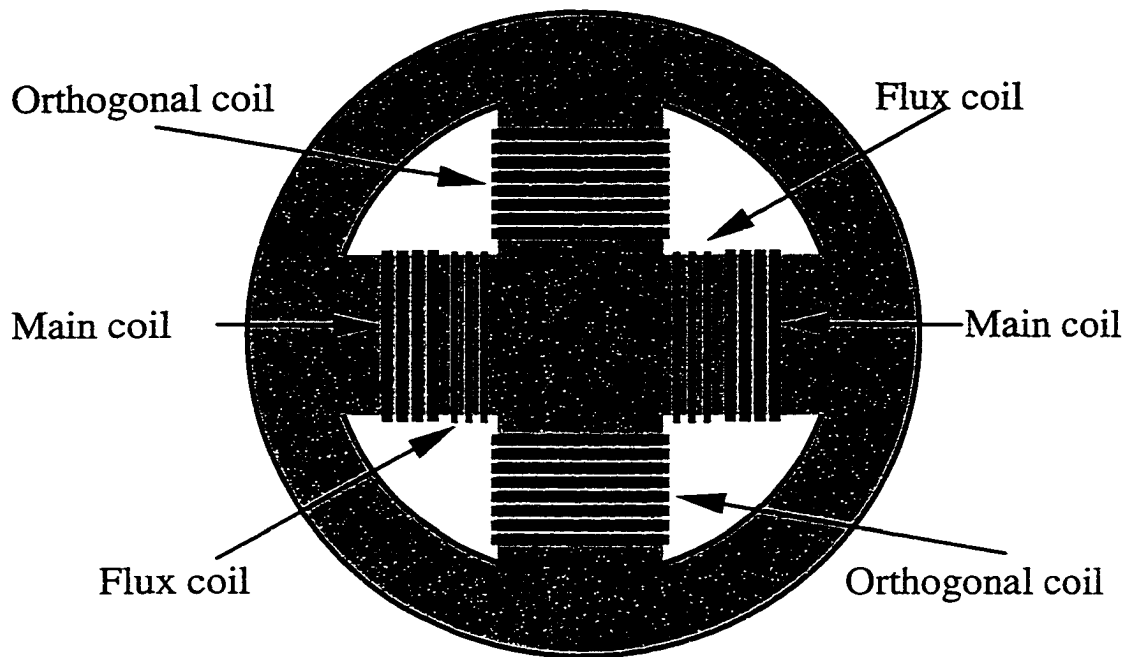


Figure 4-1 New design of circular button ferrite inductor provided by Rockwell Collins.

circumferential path provided the closed flux path for both magnetic fields so that there was no demagnetizing effect for either magnetic field.

#### 4.2.2 Inductance measurements

In this study, the terminal inductance of the main coil of this circular button ferrite device was measured under different orthogonal currents at different frequencies using HP 4275A multi-frequency LCR meter. Figure 4-2 shows the effect of the orthogonal current on the measured inductance of the circular button ferrite device. At a frequency of 20KHz, the measured inductance was decreased from 2.4 mH at zero orthogonal current to 0.24mH at an orthogonal current of 1A. The effective inductance was reduced by a factor of 10. The results showed that although there was difference in initial inductance (the inductance without an orthogonal current) at different frequencies, with an orthogonal

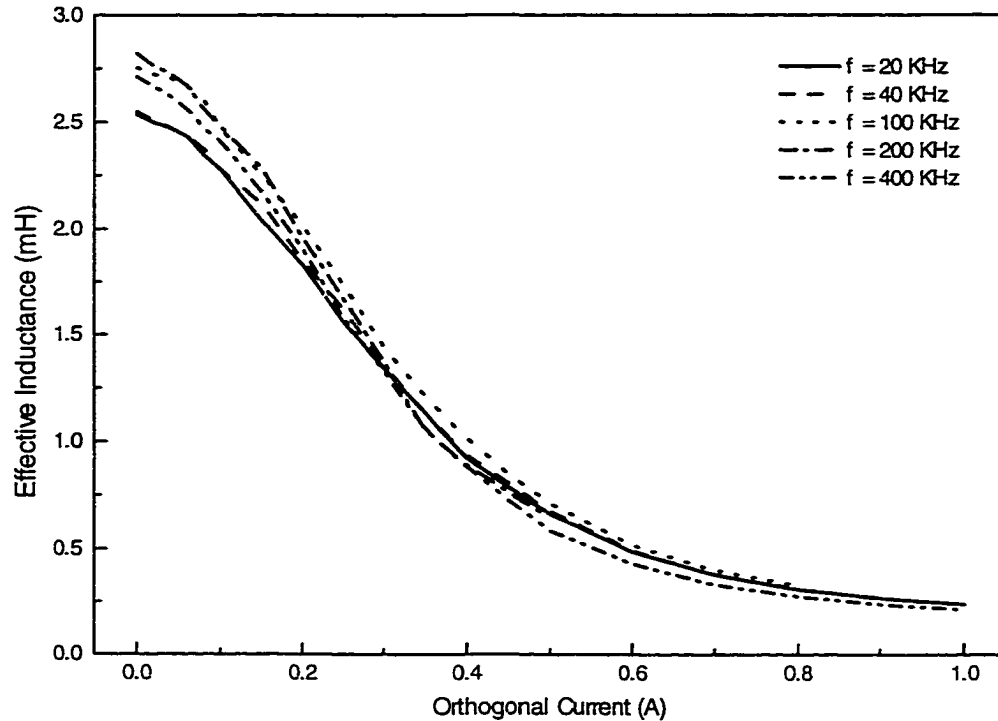


Figure 4-2 The effect of orthogonal current on measured inductance of the circular button inductor at different frequencies.

current of 0.9A, the measured inductance at different frequencies approached approximately the same value. The results of the measurements indicated that the inductance of this ferrite device can be adjusted electrically by changing the orthogonal current.

It is noted that the inductance measured by HP4275A multi-frequency LCR meter was only small current inductance. For a power inductor, a strong current in the main coil is expected. In fact, measurements performed at Rockwell Collins showed that the inductance could be reduced by a factor of 10 if the main current is increased to 1A. This fact indicated that the decrease in measured inductance was mainly due to saturation in the magnetic circuit instead of the orthogonal field effect.

As shown in chapter 5, two dimensional magnetic finite element modeling of the flux distribution in the circular button inductor showed that only in the center region of the button device, were the two magnetic fields orthogonal to each other. Around the circumferential flux path, magnetic fluxes created by the two magnetic fields were actually in the same direction in two quarter edge paths, and in the opposite direction in the other two quarter edge paths. It was the summation of two fluxes in the same direction which resulted in the saturation in a part of magnetic circuit. Additionally, due to the closed magnetic circuit and high permeability of ferrite, an MMF of 8 Ampere-turns was enough to saturate the magnetic circuit. Once the material was saturated, its effective permeability dropped significantly and this resulted in a decrease in the measured inductance. For general power inductors, saturation should be avoided. The common method is to add an air gap in the magnetic circuit to reduce the effective permeability and stabilize the performance of the magnetic device.

The saturation can be visualized by 3D nonlinear finite element modeling which will be discussed in Chapter 5. The saturation was also observed indirectly in hysteresis measurements of the same ferrite device as discussed in next section.

#### 4.2.3 Hysteresis measurements

In order to make hysteresis measurements using AMH-401 hysteresisgraph, the flux coil which was consisted of two 3-turn coil on each arm of main path, was wound on the ferrite button device. In the AMH-401 hysteresisgraph system, the magnetic field is not directly measured, instead the magnetic field was evaluated through the applied current based on Ampere's circuital law. Considering the fact that the width of

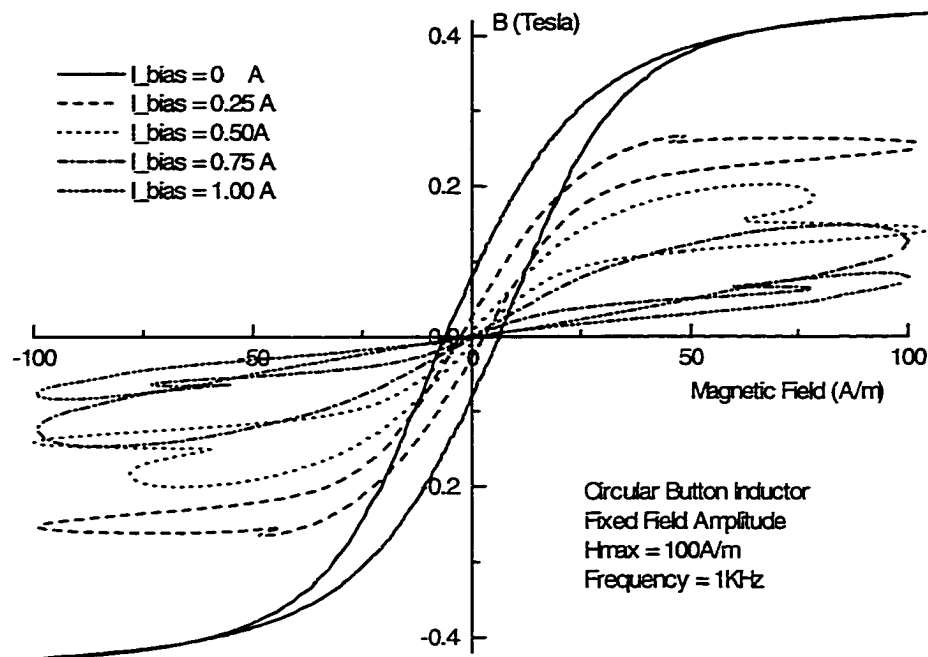


Figure 4-3 The hysteresis loops of the circular button inductor under the action of orthogonal currents.

circumferential path of the button was half of the width of the main path and magnetic flux branches along two circumferential paths after leaving main path, in this measurement, the path length which was needed to evaluate the magnetic field, was taken as 12.9 cm which is the sum of the length of inner main path and the length of the semicircular circumferential path.

Figure 4-3 shows the effect of the orthogonal current on hysteresis loops of the circular button inductor at an excitation frequency of 1KHz. As observed in other magnetic materials, the hysteresis loops were rotated clockwise with increasing orthogonal current. However, hysteresis loss rapidly increased with increasing orthogonal current in this measurement. This deterioration in hysteresis loss is believed to result from saturation in the magnetic device.

Without an orthogonal current, a typical hysteresis loop was observed. When the applied magnetic field was larger than 50 A/m, corresponding to an MMF of 6.5 Ampere-turn in the main coil, the magnetization approached saturation. The orthogonal current also created flux in the circular button inductor. Since the orthogonal coil had a total of 16 turns, an orthogonal current of 0.25A had already begun to saturate the magnetic circuit. According to the geometry of the configuration, in two quarter paths two fluxes canceled each other, while in other two edge paths, two fluxes were along the same direction. It is the cancellation of two fluxes which is believed to result in the increase in hysteresis loss.

When a magnetic field changes in a material that is in a deep saturation region of magnetization, the change in magnetization is caused by reversible domain rotation. There is no hysteresis loss for reversible magnetization. With an orthogonal current of 0.5A, the device, particularly in the circumferential paths, was magnetized to saturation. With increasing main current, however, due to the cancellation of two fluxes, magnetization decreased in two edge paths, was pulled out of saturation region, and moved into the irreversible magnetization region. It was the irreversible magnetization which resulted in the significant increase in hysteresis loss. However, with increasing orthogonal current which magnetized the specimen to a deeper and deeper saturation, a moderate main magnetic field could not pull magnetization out of reversible saturation, hysteresis loss can be expected to decrease from its maximum. This was actually observed in Figure 4-3, where the loop area of hysteresis loop with 1.0A orthogonal current was less than the area of hysteresis loop with 0.75A orthogonal current.

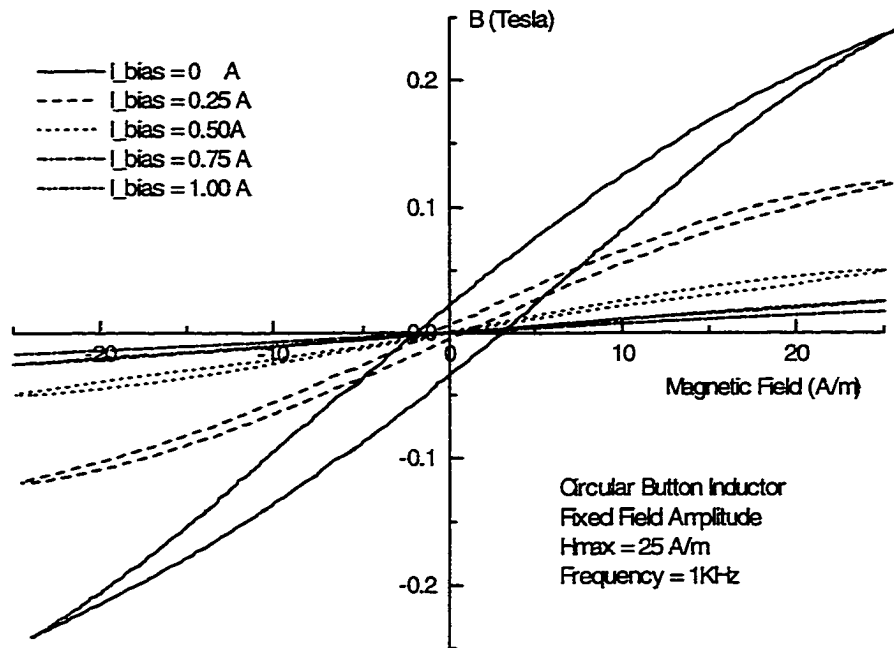


Figure 4-4 The small field hysteresis loops of the circular button inductor under the action of orthogonal current.

If the applied main field is small enough so that the cancellation of two fluxes can not pull magnetization out of reversible saturation region, hysteresis loss can be expected to decrease with increasing orthogonal current because the increasing orthogonal current magnetized the specimen to deeper and deeper saturation. Figure 4-4 shows the hysteresis loops at lower main field amplitude under the action of the orthogonal current. Not only the hysteresis loop rotated with increasing orthogonal current, but also the area of hysteresis loop decreased with increasing orthogonal current. The squares in Figure 4-5 show relative permeability calculated from the data in Figure 4-4. The fact that inductance and permeability followed the same variation indicated that the change in inductance measured by HP 4275 LCR meter resulted from the change in the small field permeability under the action of an orthogonal bias field.



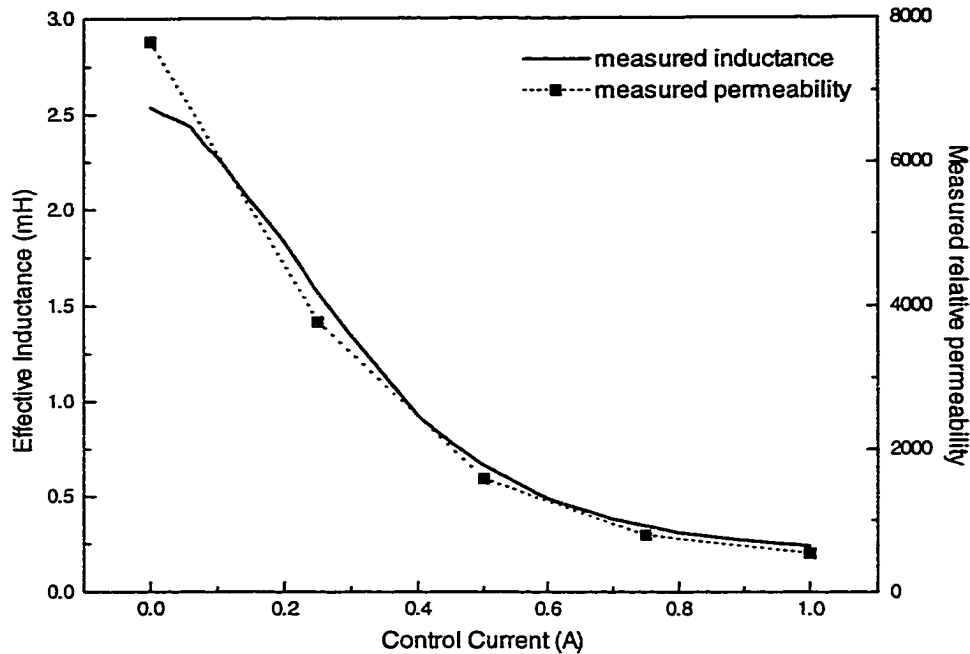


Figure 4-5 The relationship between small current inductance and small field permeability under the action of orthogonal currents.

Figure 4-6 shows that the effect of orthogonal current on the hysteresis loops when the specimen was magnetized to the same magnetic induction of 0.05 Tesla. In the presence of an orthogonal field, the hysteresis loss increased in order to reach the same magnetic induction. However, with increasing orthogonal current, the range over which main magnetization can reversibly fluctuate increased. The increasing orthogonal current magnetized the specimen to deeper saturation, consequently a larger magnetic field was needed to pull the magnetization out of the reversible magnetization regime.

In these measurements, an unusual shape of hysteresis loops was observed as shown in Figure 4-3. With the presence of an orthogonal current, when the magnetic field was increased from zero to 100A/m, the applied magnetic field suddenly decreased and then increased to reach the control value of  $H_{max}$ .

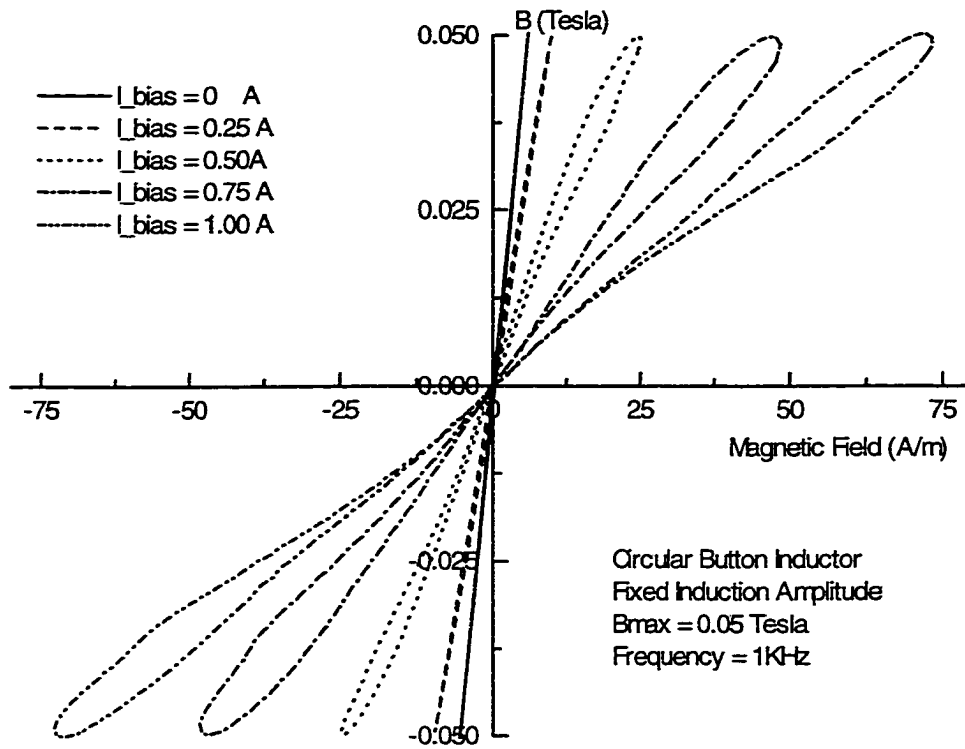


Figure 4-6 The effect of orthogonal currents on hysteresis loops of the circular button inductor.

Since magnetic field was externally applied, it should not suddenly decrease during its increasing process. This unphysical phenomenon is not believed to result from the orthogonal field effect, but may be related to the ferrite button device. The feedback system of the AMH 401 hysteresisgraph can not properly handle the system response (due to the interaction between two magnetic fields), and therefore sends out an incorrect wave shape of excitation current. Hysteresis measurements were made again under the same experimental conditions except at a low frequency of 100Hz, as shown in Figure 4-7. In this case, the phenomenon disappeared. This confirmed that the unphysical hysteresis curve came from the anomalous system response of the AMH-401 hysteresisgraph instead of the orthogonal field effect.

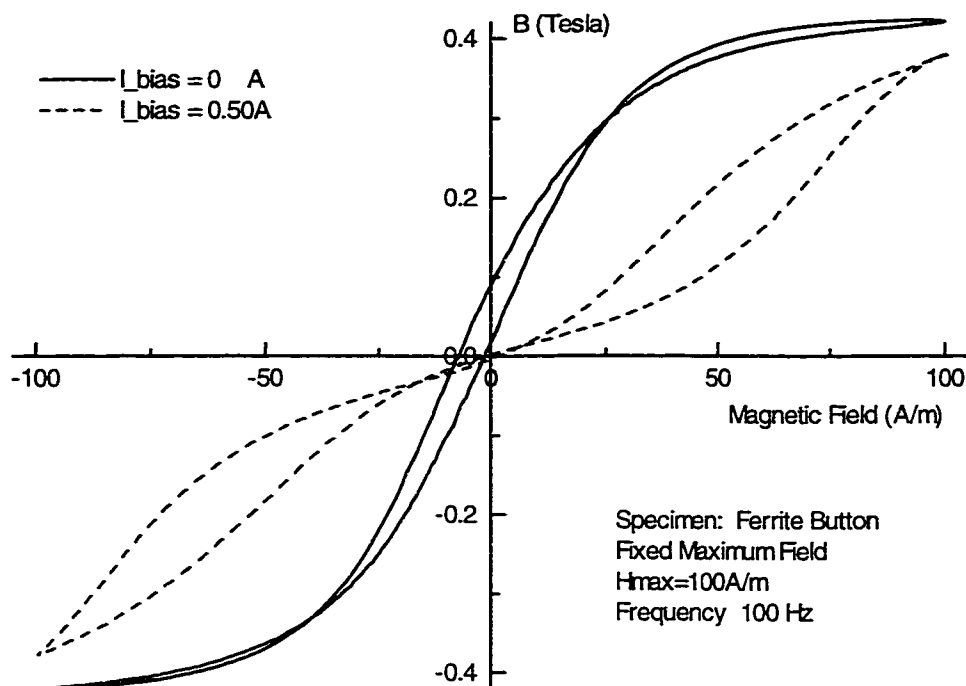


Figure 4-7 Hysteresis measurements on a circular ferrite button at 100Hz.

#### 4.2.4 Conclusion

The inductance measurements on the circular button inductor showed that the measured small current inductance can be reduced by a factor of 10 by changing the orthogonal current. Measurements on the small field permeability were consistent with these results. On the other hand, hysteresis measurements indicated that the decrease in the inductance resulted from the saturation of a part of the magnetic circuit.

Hysteresis measurements on the circular button ferrite inductor showed an increase in hysteresis loss with the presence of an orthogonal field. It is believed to result from the cancellation of fluxes created by two magnetic fields. It was the cancellation that pulled magnetization out of the reversible region into the irreversible magnetization

region. Stronger orthogonal current or smaller main magnetic field can be used to improve ( i.e. reduce ) the hysteresis loss.

From the FEM analysis, the two magnetic fields were perpendicular to each other only in the region of the center of the device. Strictly speaking, therefore, this ferrite device did not work entirely in an orthogonal field mode. It was the saturation in the part of the device which gave rise to the large change in inductance.

### **4.3 Inductor controlled by selected saturation**

#### **4.3.1 Design of a non-gapped power inductor**

During this study, the design of a prototype un-gapped power inductor was requested by the sponsor as a part of verification study of research project. The general specifications for the device were a 50  $\mu\text{H}$  non-gapped inductor with a 2A working current range. Within the 2A working current range, the inductance should remain approximately constant. In the design, the optimization of energy storage, inductance change and overall dimension should be included. The major goal of this verification study was to investigate whether the orthogonal field effect allowed implementation an un-gapped power inductor that can store useful amounts of energy without paying an appreciable penalty in size, weight, and energy efficiency when compared to a traditional gapped ferrite inductor.

Gapped power inductors are well known. In a gapped inductor, an air gap is intentionally added in a magnetic circuit to set the inductance of the inductor, to increase the energy storage density and to stabilize its performance. For an un-gapped structure,

however, other methods have to be applied to reduce the high permeability of ferrite devices so that energy storage density can be increased.

#### *4.3.1.1 Energy storage*

The energy stored in a magnetic device can be mathematically expressed by the following equation,

$$E = \frac{1}{2} \int B \cdot HdV$$

Due to the saturation of magnetic materials, the maximum magnetic induction  $B$  is limited. As a matter of fact, in a real power inductor application, in order to limit the core loss, the maximum magnetic induction is usually designed to be well below the level of saturation. The way to increase energy storage or energy density is to increase the applied magnetic field. Considering the relationship between magnetic field and magnetic induction, the way to increase the energy storage is to decrease the effective permeability so that a higher magnetic field can be applied without exceeding the magnetic induction limit. An air-gap is commonly used to reduce the effective permeability, thereby increasing energy storage, of the inductor because an air-gap which is assembled in series in the magnetic circuit has only unit relative permeability.

Experimental results showed that an orthogonal field can reduce the effective permeability of a magnetic material. Although the orthogonal field effect is a promising way to increase the energy storage, it was difficult to implement a device in which the main magnetic field and orthogonal field are completely orthogonal to each other without compromising on the size and complexity of the assembly.

On the other hand, when a magnetic specimen is magnetized to saturation, its permeability will drop to a very small value. If the specimen is connected to other magnetic material in series, the overall effective permeability will also drop because the saturated specimen acts as an effective air gap to reduce overall permeability of the device. However, it is well known that if a specimen is magnetized to saturation, the hysteresis loss will increase significantly. That is why in a power inductor, the maximum magnetic induction is usually designed to a level well below saturation magnetization. On the other hand, if the applied magnetic field is only cycled within the saturation region, because magnetization in the saturation region is reversible domain rotation, there is no hysteresis loss associated with the magnetization.

#### *4.3.1.2 Designed variable inductor*

Considering the fact that the first concern was energy storage density for an ungapped inductor, a design which employed selected saturation was proposed. The basic idea behind the design was that using a strong orthogonal magnetomotive force to saturate all edge paths, then the main magnetic path will no longer seem like a closed magnetic circuit. Strong demagnetizing effects reduce effective permeability significantly. Therefore, the energy storage capacity will increase. The saturation region can be considered as a virtual air gap since it has very low permeability compared with a normal ferrite.

The geometry of this device is shown in Figure 4-8. During the design process, the following facts or factors had been considered:

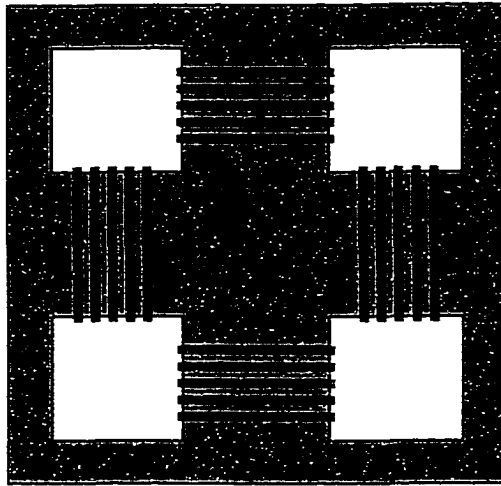


Figure 4-8 Designed variable square button ferrite inductor based on selected saturation.

(i) The device should have a narrow circumferential path so that it can be easily magnetized to saturation. The width of edge path should be less than half of the width of orthogonal path. With a strong enough orthogonal magnetomotive force, all circumferential paths will be removed magnetically. The main flux path will then no longer have characteristics of a closed magnetic circuit. The strong demagnetizing effect reduces the effective permeability ( inductance) to a very small value. Therefore, the energy storage can be increased.

(ii) The desired  $50 \mu\text{H}$  inductance should be obtained when all circumferential paths are in deep saturation. When the magnetic flux in the main path is cycled, due to the cancellation and summation of fluxes created by two coils in the circumferential path, the saturation permeability will fluctuate. Only under a deep saturation in the circumferential region will the permeability fluctuation be small enough so that it will not significantly affect the overall effective permeability. As a result, the device should have a high initial inductance without the orthogonal current. A high permeability magnetic material such as ferrite is therefore desirable.

(iii) Considering the fact that in two quarter edge paths, fluxes created by the main coil and orthogonal field cancel each other, then in order to avoid the magnetization in the two paths being pulled out saturation when the current in main coil reaches its 2A maximum, a large magnetomotive force in the orthogonal path should be applied.

(iv) The selection of other geometrical parameters, such as cross sectional area of main path, thickness of the device was based on a traditional gapped inductor design which has a similar inductance and energy storage.

#### 4.3.1.3 An assembled rectangular button inductor

A variable button inductor was constructed from commercially available ferrite material as shown in Figure 4-9 in order to perform experimental tests on this new technology. The objective was to find whether the saturation mode button is workable from the viewpoint of energy storage. The desired characteristic was that under the action of the orthogonal current, there was a large enough main current range in which the inductance has only allowable small change.

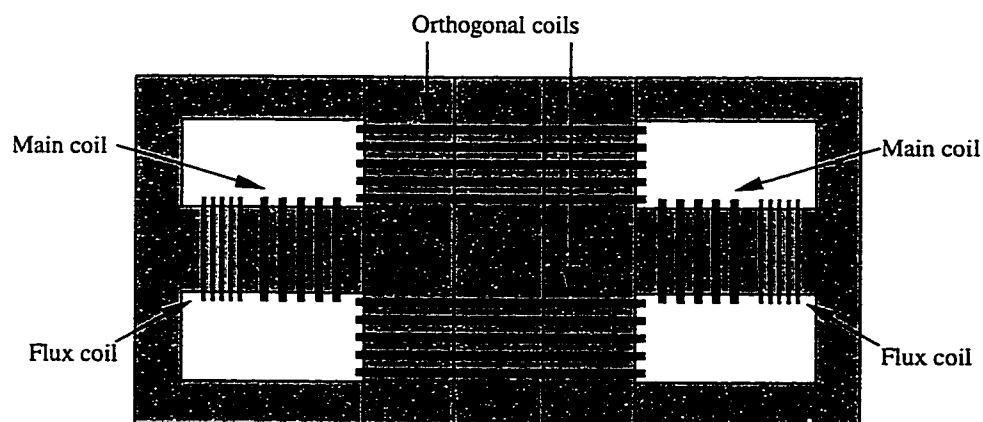


Figure 4-9 The geometry of the assembled rectangular button inductor.



This rectangular button inductor consisted of two “E” cores and three “T” cores which were ordered by Rockwell Collins from Magnetics, Inc. The raw materials were P-type manganese-zinc ferrite with a nominal permeability of 2500 and a saturation of 0.5Tesla. The main coils consisted of two 5-turn coils in each winding window. The orthogonal coils consisted of two 20-turn coils in each winding window.

#### 4.3.2 Inductance measurements of a simulated inductor

The measurements of inductance with DC bias current were made by Rockwell Collins. Figure 4-10 shows the effective inductance of the rectangular button inductor against the current in the main coil under different orthogonal currents.

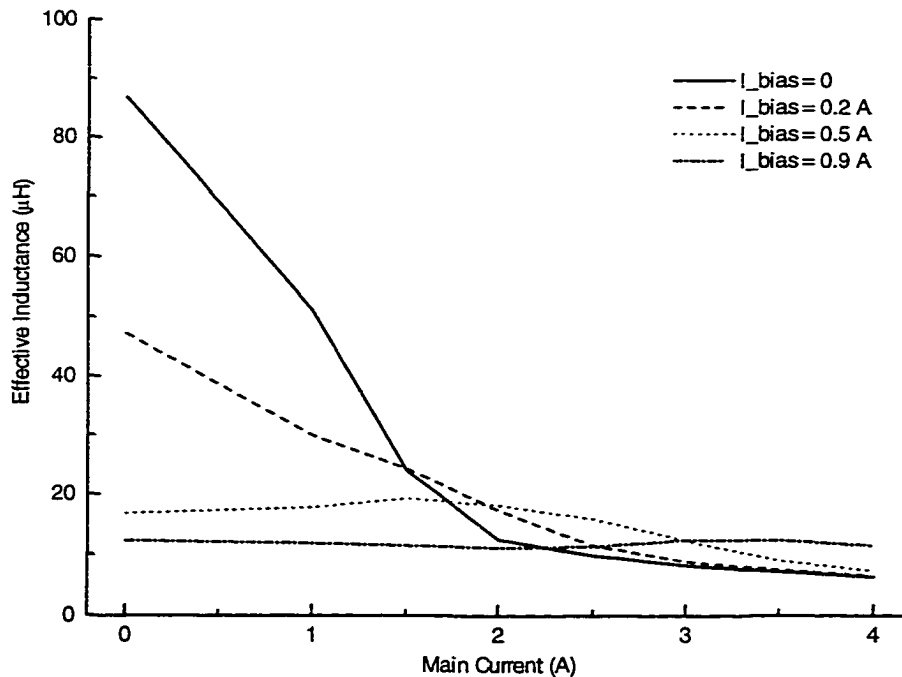


Figure 4-10 The inductance of the rectangular button inductor under the action of orthogonal currents.

Without the presence of the orthogonal current, the initial inductance of this inductor was 87  $\mu\text{H}$ . With increasing main current the inductance decreased from its initial 87  $\mu\text{H}$  to a value of 6  $\mu\text{H}$ . This is due to the saturation of portion of the magnetic circuit as observed on the circular ferrite button device. Considering its high permeability of 2500, without an air gap the magnetic circuit can be magnetized to saturation with only a moderate amount of current.

With the presence of the orthogonal current, the small current inductance decreased with increasing orthogonal current as shown in Figure 4-11. The decrease in inductance was also due to the saturation. However, this time the saturation resulted from the action of orthogonal current instead of main current and occurred in the circumferential region and orthogonal path instead of main path. With a strong orthogonal magnetomotive force, all circumferential paths were magnetized to saturation and can be

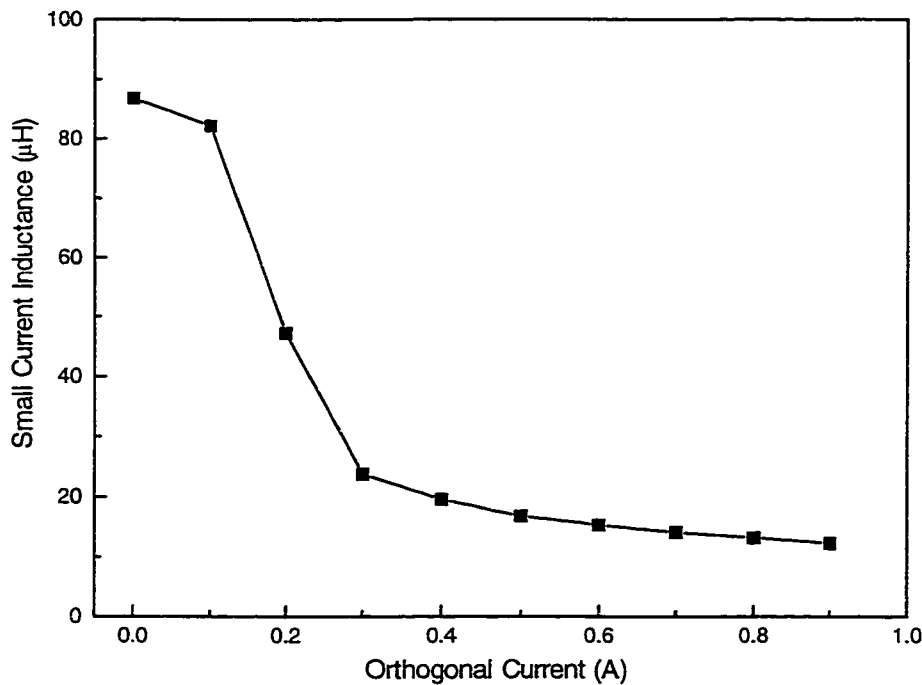


Figure 4-11 Small current inductance of the rectangular button inductor under the action of an orthogonal current.

considered to be magnetically equivalent to air having a relative permeability of 1. Without a closed magnetic circuit, the demagnetizing effect reduced the effective permeability to a very small value. The inductance therefore decreased with increasing orthogonal current.

It is interesting to note that when the orthogonal current was 0.9A, as shown in Figure 4-12 within a 4A main current range, the inductance only had a small variation of less than 10% around 12  $\mu\text{H}$ . This was what was desired. If the orthogonal current is decreased, the inductance plateau will be shifted up. However, the width of inductance plateau shrank with decreasing orthogonal current.

The goal of this design of the un-gapped inductor was to maximize the energy storage, to provide inductance controllability and to maintain the inductance constant within a specified current range. Since the effective permeability was reduced

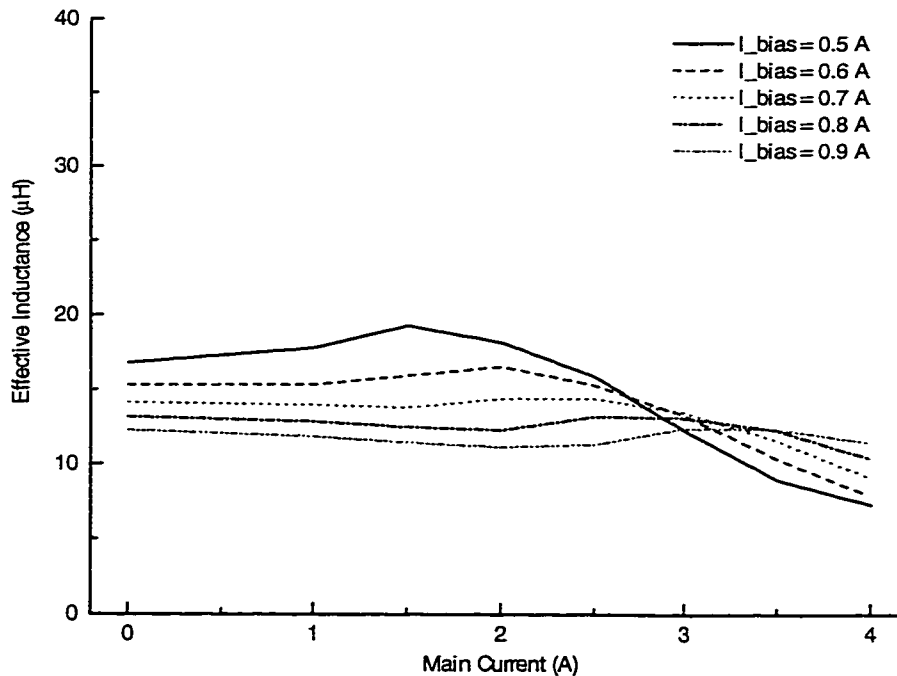


Figure 4-12 The inductance of the rectangular button inductor under the action of large orthogonal currents.

dramatically, the energy storage was increased. Since an inductance plateau in which the measured inductance only had a small fluctuation was observed, the inductance can remain constant. Since the height of the inductance plateau can be adjusted by the orthogonal current, inductance can be controlled electrically. The design goal was therefore achieved.

#### 4.3.3 Hysteresis measurements of the rectangular button inductor

During the study, an identical rectangular button ferrite inductor was also assembled at Iowa State University using the same ferrite cores and wound with the same number of turns of excitation coil and orthogonal coil. In order to measure the flux density, an extra set of flux coils, one 5-turn coil on each center leg of the “E” cores, were added as shown in Figure 4-9.

Hysteresis measurements were made using the AMH-401 hysteresisgraph under different measurement modes at different frequency. The measured hysteresis curves under the action of the orthogonal current were found to be similar to the hysteresis curves obtained in the circular button inductor as shown in Figures 4-4, 4-5 and 4-6 since these two inductors have the same topology.

However, it would be interesting to discuss the hysteresis curves which were obtained in the fixed induction amplitude measurements as shown in Figure 4-13. As observed before, the hysteresis loops rotated clockwise as the effective permeability decreased with increasing orthogonal current. This is consistent with the experimental results of the effective inductance which was determined by the effective permeability.

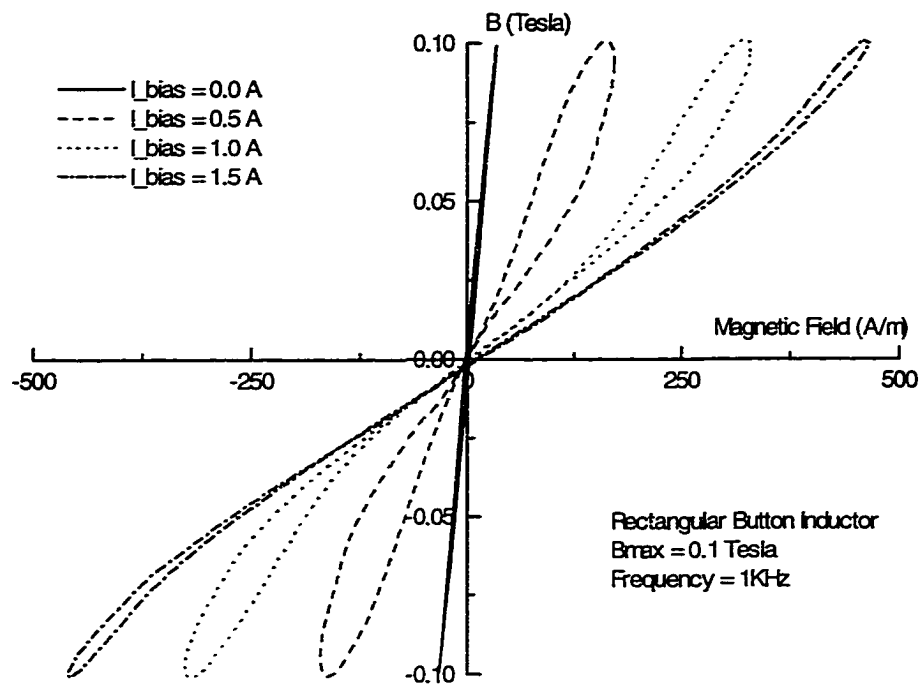


Figure 4-13 The hysteresis curves of the rectangular button inductor under the action of the orthogonal current.

On the other hand, the loop area, or hysteresis loss, first increased with increasing orthogonal current. With an orthogonal current of about 0.6A, the area of the hysteresis loop reached its maximum. After that, the width of the hysteresis curve began to decrease with increasing orthogonal current. With a strong enough orthogonal MMF, the two branches of the hysteresis curve can therefore be expected to overlap to each other and become a single line.

Figure 4-14 shows the effect of the orthogonal current on the core loss of the assembled rectangular button inductor. With increasing orthogonal current, the core loss first increased. After passing its maximum at an orthogonal current of 0.6A, the core loss began to drop. Following the trend, with a strong enough orthogonal current, the core loss can be reduced to a value close to the initial core loss without an orthogonal current.

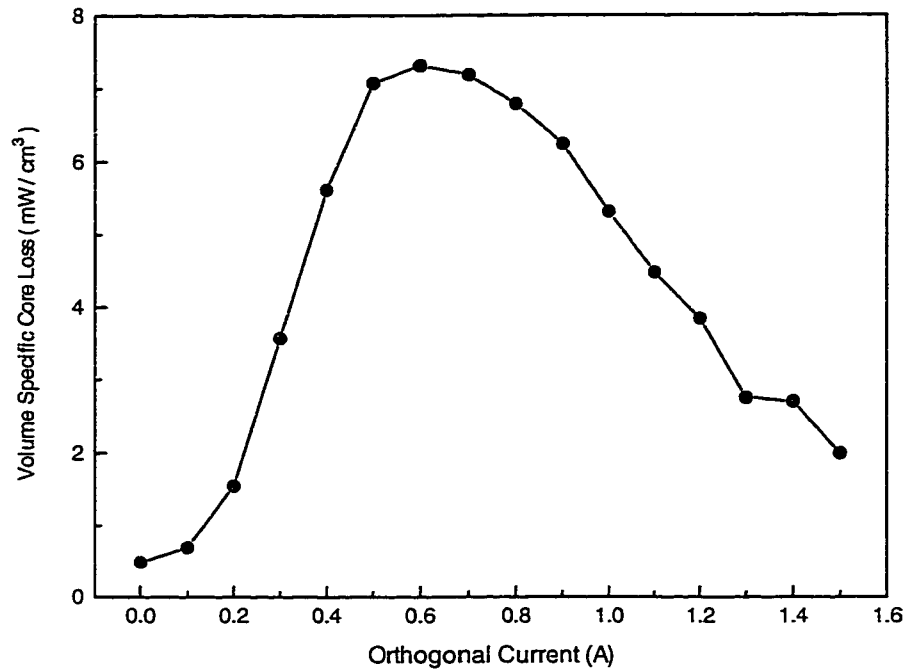


Figure 4-14 The effect of the orthogonal current on the hysteresis loss of the rectangular button inductor in the fixed induction amplitude measurements at 1KHz.

As discussed in the last section, the inductance measurements showed that the design goal of a variable inductor can be achieved. The results of hysteresis measurements showed that the price paid in core loss can be minimized with a strong enough orthogonal current.

#### 4.4 Conclusion

The inductance measurements on the circular button ferrite inductor showed that due to the saturation resulting from orthogonal current, the measured small current inductance can be reduced by a factor of 10 by changing the orthogonal current. Measurements of the small field permeability were consistent with the results. Hysteresis

measurements on the circular ferrite button device showed an increase in hysteresis loss with the presence of an orthogonal field. This is believed to result from the cancellation of two fluxes created by two magnetic fields. The flux cancellation pulled magnetization out of reversible saturation region into an irreversible magnetization region and resulted in increased hysteresis loss. Stronger orthogonal current or smaller main magnetic field could be used to improve the hysteresis loss.

Utilizing the selected saturation, a prototypic un-gapped ferrite inductor was proposed, in which a strong orthogonal magnetomotive force was applied to magnetize the circumferential path into deep saturation and to magnetically remove the circumferential paths so that a strong demagnetizing effect reduced the inductance significantly. The inductance measurements on an assembled rectangular button inductor based on the above design confirmed the expected behavior. The inductance of the inductor not only was observed to decrease with increasing orthogonal current, but also an inductance plateau, where the effective inductance only had small fluctuation with the main current, was observed. The hysteresis measurements on an assembled rectangular button inductor showed that with a strong enough orthogonal current, the core loss can be reduced to a small value.

## 5. APPLICATIONS OF FINITE ELEMENT MODELING

In this study, the finite element modeling was extensively used to numerically analyze and solve some problems, such as demagnetizing field inside a specimen, distribution of magnetic field and flux, inductance of a magnetic device, which were otherwise very difficult to solve. Depending on the problems involved, either linear or nonlinear, either two-dimensional or three-dimensional analysis was performed using a commercial finite element modeling software package, ANSYS®. In this chapter, some results of the finite element modeling performed in this study will be presented with corresponding discussion.

### 5.1 Introduction

Electromagnetic fields are governed by the Maxwell's Equations.

$$\nabla \times \mathbf{H} = \mathbf{J} + \frac{\partial \mathbf{D}}{\partial t}$$

$$\nabla \times \mathbf{E} = -\frac{\partial \mathbf{B}}{\partial t}$$

$$\nabla \cdot \mathbf{B} = 0$$

$$\nabla \cdot \mathbf{D} = \rho$$

For magnetostatic analysis, only the following two equations are needed to describe the magnetic field:

$$\nabla \times \mathbf{H} = \mathbf{J}$$

$$\nabla \cdot \mathbf{B} = 0$$

The above field equations are supplemented by the constitutive relation that describes the behavior of electromagnetic materials.



$$\mathbf{B} = \bar{\mu} \mathbf{H}$$

where  $\bar{\mu}$  is a permeability tensor in general cases. For homogeneous and isotropic materials involved in this study, the magnetic field is in the same direction as the applied magnetic field, and therefore the tensor can be replaced by a scalar permeability. As discussed before, the permeability is neither constant nor single-valued due to the hysteresis of ferromagnetic materials. However, the finite element software package, ANSYS<sup>®</sup>, used in this research, is unable to solve magnetic problems with hysteresis. Either a constant permeability, which corresponds to linear finite element modeling, or a single-valued permeability function of magnetic field, which corresponds to nonlinear finite element modeling, has to be assumed.

Although the above equations provide the theoretical foundation for solving any magnetic problem, most of the magnetic problems are indirectly solved by the potential method, using either the vector potential method or the scalar potential method.

### 5.1.1 Vector Potential Method

Derived from the divergence-free postulate of magnetic induction, magnetic induction can be expressed by the magnetic vector potential  $\mathbf{A}$ :

$$\mathbf{B} = \nabla \times \mathbf{A}$$

In order to ensure uniqueness of the vector potential, the Coulomb Gauge condition can be employed.

$$\nabla \cdot \mathbf{A} = 0$$

The differential form of Ampere's circuital law can then be transformed into the Vector Poisson's equation, which establishes the relationship between the vector current density

$J$  and vector potential  $A$ ,

$$\nabla^2 A = -\mu_0 J$$

Except for a few simplified problems, this second order vector differential equation has to be solved numerically. The finite element method is one of the most widely used numerical methods. In a finite element method, such as ANSYS, the problem is discretized into finite-sized elements using a element type provided by the software. In ANSYS, PLANE13, PLANE53 was implemented using the vector potential method for 2D magnetic field analysis, while SOLID97 was implemented using the vector potential formulation for 3D magnetic field analysis. However, for models containing materials with different permeability, the 3D vector potential formulation is not recommended by ANSYS. The solution has been found to be incorrect when the normal component of the vector potential is significant at the interface between elements of different permeability[50].

### 5.1.2 Generalized Scalar Potential Method

In a current-free region where the curl of field is zero, the magnetic field can be expressed by a scalar potential  $\phi$  alone.

$$H = -\nabla\phi$$

In current carrying regions, however, the magnetic field should be decomposed into two terms[51],

$$H = H_g - \nabla\phi$$

where  $H_g$  is a seed value of magnetic field and  $\phi$  is the generalized scalar potential. Since the composed magnetic field should still satisfy the Ampere's law, the initial seed value

of field  $H$  must satisfy the Ampere's law. Additionally, in order to avoid difficulties with cancellation errors [51], the absolute value of  $H_g$  must be greater than that of  $\nabla\phi$ .

The selection of  $H_g$  is essential to the development of any of the scalar potential formulation. Since a field evaluated by the Biot-Savart law satisfies the Ampere's law,:

$$H_{BS} = \frac{1}{4\pi} \int \frac{J \times r}{r^3} dV$$

$H_{BS}$  give a good approximation about the initial seed value of field  $H_g$ . After the transformation, magnetic induction should still be divergence-free.

$$\nabla \cdot \mu (H_{BS} - \nabla\phi) = 0$$

Depending on the characteristic of the problem involved, ANSYS provide three different solution strategies, Reduced Scalar Potential strategy, Difference Scalar Potential strategy and General Scalar Potential strategy. When both multiply connected magnetic materials and non-zero current source are in the problem region, the General Scalar Potential formulation is applicable[51]. The General Scalar Potential strategy uses a three-step solution procedure. The first step performs a solution only in the region of the magnetic material with the seed magnetic field  $H_g$  evaluated by the current source and subjects the solution to the boundary condition about the normal component of magnetic induction at the interface. The second step performs a solution only in the region of the air with the seed magnetic field evaluated by the same current source and subjects the solution to the boundary condition about the tangential component of magnetic field at the interfaces. The third step solves the problem using the fields evaluated on the first two steps as the seed fields for material regions and air regions respectively.

In ANSYS, the element type SOLID5, SOLID96 and SOLID98 were implemented using the scalar potential formulation for 3D magnetic field analysis. All three element

types are capable of performing the Reduced Scalar Potential strategy, Difference Scalar Potential strategy or General Scalar Potential strategy. In this study, considering the configuration of problems involved, the SOLID98 element, a 10-node tetrahedral element implemented by the Generalized Scalar Potential strategy, was used in 3D finite element modeling.

### 5.1.3 The B-H curve for nonlinear finite element modeling

The ANSYS finite element software so far is unable to handle hysteresis in its magnetic modeling, instead a single-valued  $B-H$  curve is used to characterize the material response under the action of a magnetic field. The permeability and saturation magnetization are the two most important properties needed to characterize a ferrite. Generally, the vendor of a ferrite device provides the initial permeability and flux density measured at a high magnetic field.

A constant permeability represents a straight line through the origin of a  $M-H$  plot, and saturation magnetization at a high field can be described by a horizontal line in the  $M-H$  plot. Based on the idea that a magnetization curve should gradually change from the constant permeability straight line to the horizontal line, in this study, the two straight lines were inter-connected by the following model,

$$M = M_s \tanh\left(\frac{H}{a}\right)$$

where the  $a$  can be determined by the initial permeability  $\mu_{ini}$  and the  $M_s$  can be evaluated by the flux density  $B_s$  at a certain field  $H_s$ . This model can actually be derived by the quantum theory of ferromagnetism[52] if we assume that the orientation of magnetic moments can only have two directions, spin up and spin down and the probability of a

magnetic moment in the direction of either spin up and spin down is governed by Boltzmann statistics.

The B-H curve for the finite element modeling was:

$$B = \mu_0(H + M_s \tanh(\frac{H}{a}))$$

$$M_s = \frac{B_s}{\mu_0} - H_s$$

$$a = \frac{M_s}{\mu_{ini} - 1}$$

In principle, the Langevin-Weiss model as discussed in chapter 2 can also be a representation for the magnetization of ferrite materials. However, considering the difficulty in determining the three parameters of the Langevin-Weiss model from the parameters provided by the manufacturer, the above B-H curve model was used instead in the finite element modeling.

## 5.2 Distribution and evaluation of field

### 5.2.1 Flux distribution of BEFI

The original objective of this FEM modeling was to investigate the interaction of two magnetic fields produced by two on-board coils, the excitation coil and the orthogonal coil of the BEFI inductor through the magnetic flux distribution. In this thesis, only the flux which was created by the excitation coil is presented to illustrate the orientation relation between the excitation field inside the BEFI and the orthogonal field created by an external solenoid along the length direction of the BEFI.

Considering the fact that the thickness of BEFI was much less than the length and the width of the BEFI, 2D linear finite element modeling using the PLANE53 element of

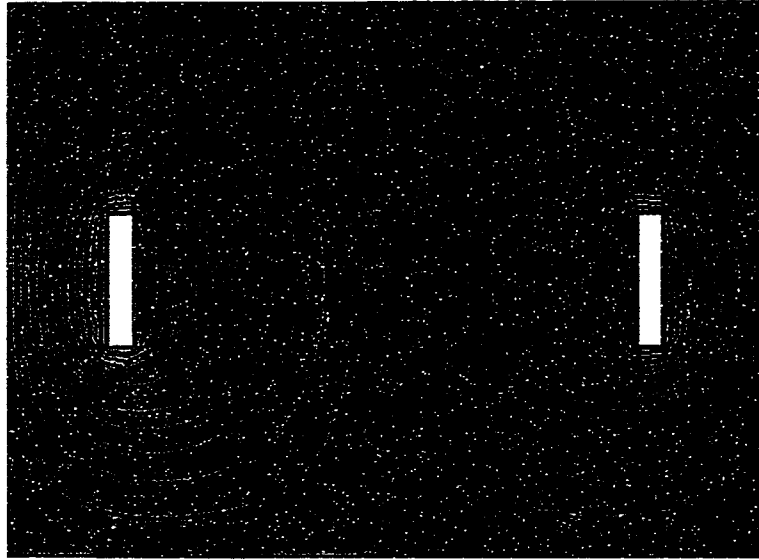


Figure 5-1 The flux lines of circuit board embedded ferrite inductor created by the on-board excitation coil.

ANSYS was performed. The PLANE53 element was a 8-node quadratic edge plane element and implemented by the vector potential formulation. Since the ferrite has much higher permeability than the relative permeability of air, the flux leakage out of the BEFI was ignored for simplicity in this modeling.

Figure 5-1 shows the magnetic flux distribution of BEFI device created by an on-board excitation coil. As expected, the magnetic fluxes formed closed loops inside the specimen in the shape of a horizontal figure of eight. For linear analysis, the magnetic field is always in the same direction of the magnetic flux. Since the orthogonal field created by an external solenoid was along the horizontal direction, the orthogonal field was not orthogonal to the excitation field direction everywhere. In some regions within the specimen, the flux lines created by the two fields were even parallel or anti-parallel to each other. However, considering the symmetry of flux lines about the vertical center line, for any location at which the orthogonal field was parallel to the excitation field, one

always can find a symmetry location at which the orthogonal field was anti-parallel to the excitation field. The effect of parallel fields can therefore be ignored for the qualitative analysis of the orthogonal field effects. It was also evident that the magnetic field  $H$  and magnetic induction  $B$  were not uniformly distributed. Along the horizontal center line, the flux density at the center of the device was smaller than the flux density outside the excitation coil.

### 5.2.2 The internal orthogonal field along the toroid axis

As discussed in chapter 3, due to the strong demagnetizing effect, the internal orthogonal field along the axis of a ferrite toroid was expected to be only a small fraction of the external orthogonal field. Because of the non-elliptic geometry, it was difficult to analytically calculate the internal orthogonal field without a numerical simulation. The objective of this finite element modeling was to evaluate the orthogonal field inside the specimen along the toroid axis. The finite element modeling performed here showed that the internal orthogonal field was only a small fraction of the external orthogonal field and was even not uniformly distributed.

The finite element modeling simulated the experimental set up, a long ferrite toroid positioned at the center of a solenoid which created a magnetic field along the axial direction of the toroid. However, Considering the axial symmetry of this experimental set up, 2D finite element modeling was performed on a cross-section using the element PLANE53 of ANSYS with axial symmetry condition. Element PLANE53 was a 8-node quadratic edge plane element implemented by the vector potential formulation. Considering the fact that the internal orthogonal field was very small, a linear analysis

was performed with a constant permeability which was taken from the experimental data shown in Figure 2-10. Actually the nonlinear analysis was also performed but no significant difference in the internal orthogonal field was observed. First the model program was calibrated so that at the absence of the toroid (simply assign the relative permeability of the ferrite to 1 so that it is equivalent to air), the field component along the axial direction created by the solenoid was 15.9 kA/m. The internal field along the axial direction of the toroid was then evaluated by changing the permeability to the measured permeability.

Figure 5-2 shows the distribution of magnetic field component along the axial direction of the toroid. The internal field had its maximum at the center of the toroid. The field component gradually decreased as the end of the toroid was approached. The non-uniform distribution of the internal field can be understood in terms of the concept of the postulated magnetic free poles which were induced by the external field and aggregated on the both ends of the toroid. The demagnetizing field created by these induced surface free poles was opposite to the external field. Due to the limited area of toroid ends, the demagnetizing field was stronger near the ends of the toroid and weaker near the center of the toroid. As a result, the internal field in the center was larger than the field near the ends. Only a slight difference in the field components at different radial positions was observed in the FEM simulation. Since the magnetic field component along the axial direction was not uniform, for the purpose of hysteresis modeling, spatial averaging was made on the field axial component inside the specimen to represent the internal orthogonal field as used in chapter 3. The averaged internal orthogonal field was 59 A/m, which was only 0.37% of the external applied orthogonal field.



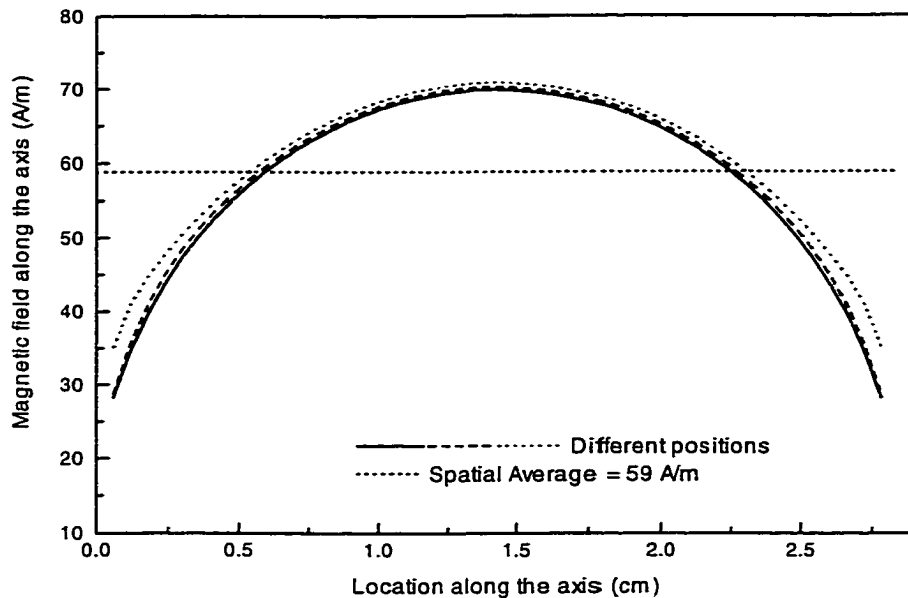


Figure 5-2 The orthogonal field inside the toroid along the axis.

### 5.2.3 Field distribution in the circular button ferrite inductor

The objective of this modeling was to study the interaction between two magnetic fields created by the excitation coils and orthogonal coils and to see how the orthogonal current changes the flux distribution in the device. As discussed in chapter 4, magnetic fields created by the excitation coils and the orthogonal bias coils were expected to cancel each other in two regions of circumferential paths and add to each other at the other two regions of circumferential paths. Another objective of this modeling was to visualize the cancellation and summation of two magnetic fields.

The finite element modeling was performed using both 2D simulation and 3D simulation. The 2D simulation was linear and was used to determine the magnetic flux distribution in the device. The 3D simulation was nonlinear and was used to evaluate the distribution of flux density so that the saturation can be graphically identified.

### 5.2.3.1 2D linear simulation

A 2D linear finite element modeling was performed also using PLANE53 element with assumption that there was no flux leakage out of the device, because of the high constant permeability of ferrite so that the flux leakage can be ignored in a linear FEM modeling. Both the excitation current sources and orthogonal current sources were modeled as uniform surface currents which were normal to the plane of the device at sides of both main paths and orthogonal paths.

Figure 5-3 shows the flux lines distribution in the circular button ferrite inductor without the presence of the orthogonal current. The flux lines showed a symmetric distribution. All four quarter paths had similar flux line distribution. There were only a few flux lines in the orthogonal path which implied a low induction distribution in the orthogonal path. However, with the presence of an orthogonal current, as shown in Figure 5-4, where the excitation magnetomotive force and the orthogonal magnetomotive force were identical, the distribution of the magnetic flux lines was profoundly changed. Due to the cancellation of two fluxes, there was almost no flux distribution in the first quarter path and the third quarter path. On the other hand, due to the summation of two fluxes, the flux line density in the second quarter path and the fourth quarter path was doubled. In the center of the device, due to the perpendicularity of two equivalent fields, the direction of vector sum of two fields was  $45^\circ$  from the horizontal direction. This was the orthogonal field region, only here the two magnetic fields were orthogonal to each other.

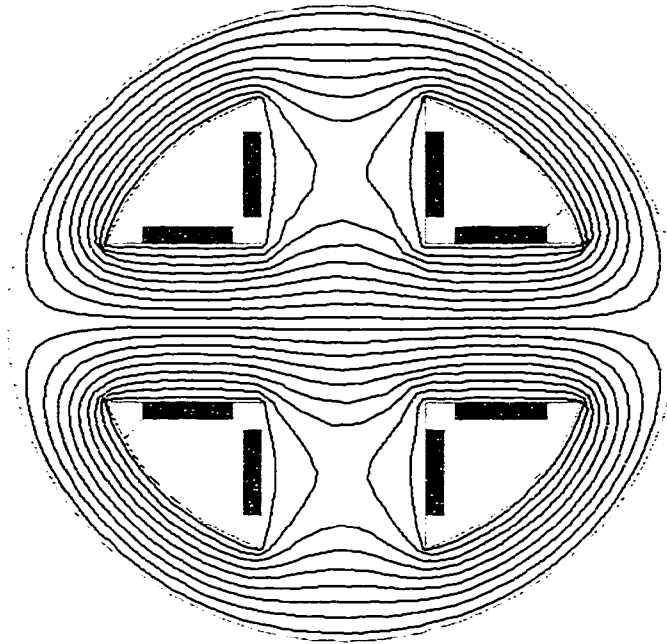


Figure 5-3 The distribution of flux lines in the circular button ferrite inductor without an orthogonal current.

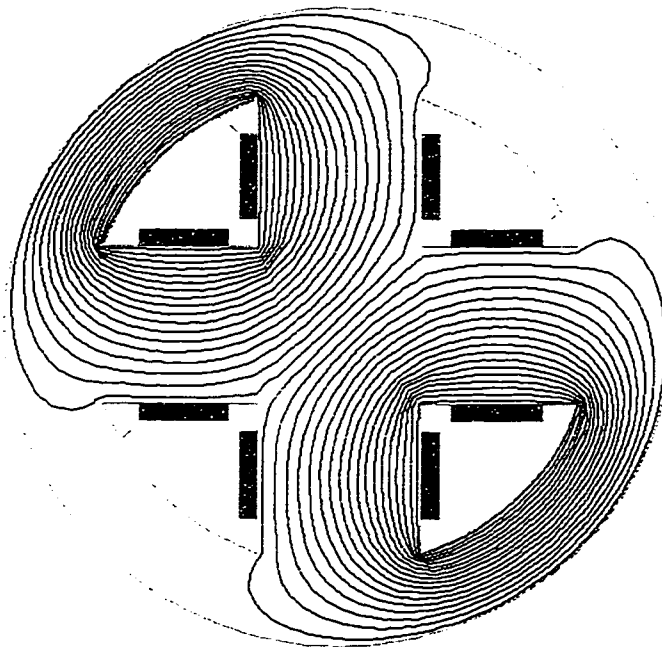


Figure 5-4 The distribution of flux lines of the circular button ferrite inductor with an orthogonal MMF that is identical to the main excitation MMF.

In this study, a series of 2D FEM simulations of the flux distribution in the device with different orthogonal magnetomotive force (MMF) was performed. In the center of the device, with increasing orthogonal MMF, the direction of flux lines was found to gradually rotate from the horizontal direction, corresponding to a zero orthogonal current, to the vertical direction corresponding to a very strong orthogonal current. On the other hand, the flux density in the first quarter path and the third quarter path was found to decrease first with increasing orthogonal current. After passing through the zero flux density as shown in Figure 5-4, which corresponds to the identical excitation MMF and orthogonal MMF, the flux density, which actually was in the other direction, was found to increase with increasing orthogonal MMF. However, the flux density in the first quarter path or the third quarter path was always less than the flux density in the second quarter path or the fourth quarter path.

#### *5.2.3.2 3D nonlinear simulation*

As discussed above, the flux density in the second quarter path or the fourth quarter path was always larger than the flux density in the first quarter path or the third quarter path. With increase of either magnetomotive force, these two regions will be magnetized to saturation first. On the other hand, if one MMF already magnetized the first quarter path and the third quarter path into saturation, the increase in another MMF will pull the magnetization out of saturation because the fluxes created by excitation coil and orthogonal coil canceled each other in the two paths. In the true linear FEM analysis in which magnetic materials were assumed to have infinite saturation magnetization, however, saturation can not be achieved. The objective of this nonlinear FEM modeling

was to graphically study the evolution of the saturation region under the action of changing main MMF and orthogonal MMF.

In this FEM modeling, as shown in Figure 5-5, the specimen was discretized using element SOLID98, a 10-node tetrahedral element implemented by the Generalized Scalar Potential formulation. Its tetrahedral shape and quadratic edges were believed to fit the geometry of the circular button ferrite inductor well. Its nonlinear capability made the nonlinear analysis possible.

In a nonlinear finite element modeling, the assumption that the device experiences no flux leakage is no longer appropriate because, with a strong enough magnetic field, the

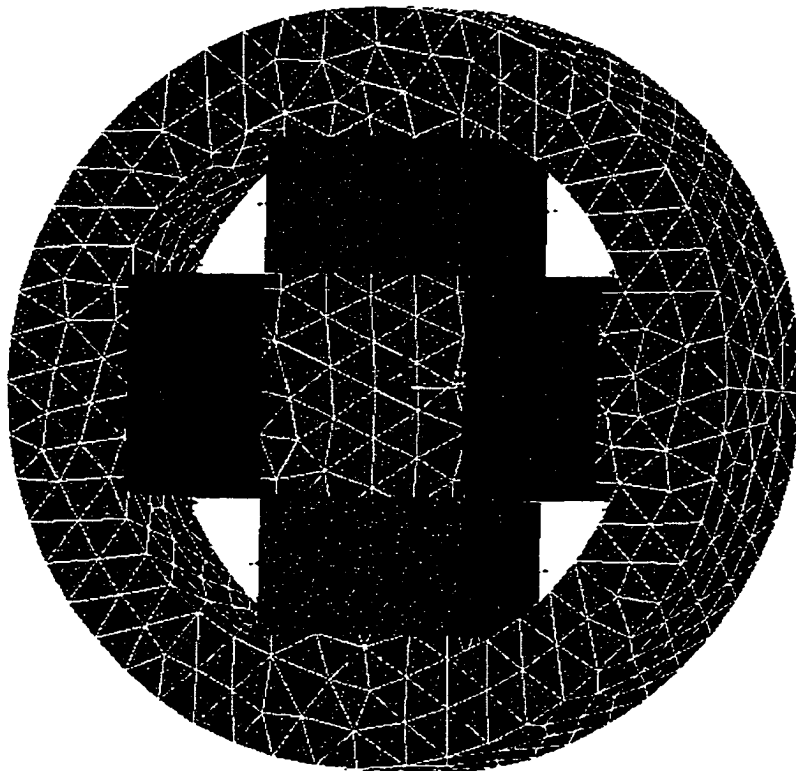


Figure 5-5 The finite element model of the circular button ferrite inductor with both excitation coils and orthogonal coils.

effective permeability could decrease to a small value which might be comparable with the permeability of air. The volume of the air which surrounded the specimen was also discretized using SOLID98 with a constant unit permeability. Outside of the surrounding air, the infinite boundary was modeled by another type of element, INFIN47, which was provided in the software to model an open boundary of a three-dimensional unbounded field problem. The excitation coils and orthogonal coils were modeled by current source element, SOURC36, which was provided in the FEM software to provide current source to 3D magnetic field problems. Figure 5-5 shows the meshed finite element model of the circular ferrite button with both excitation coils and orthogonal coils. The elements of surrounding air are not displayed in this figure. Although the whole device is displayed here, only half of the device was modeled in real calculation process to take advantage of the symmetry.

Figure 5-6 shows the distribution of flux density with an excitation MMF of 20 Ampere-turn and zero orthogonal current. All circumferential paths were near saturation. Figure 5-7 shows the distribution of flux density with an excitation magnetomotive force of 20 Ampere-turn, and an equal orthogonal MMF of 20 Ampere-turn. Compared with Figure 5-6, the second and fourth quarter circumferential paths were driven into deeper saturation due to the reinforcement of two magnetic fields, while the first and third quarter circumferential paths were pulled out of saturation into an intermediate magnetization level due to the cancellation of two magnetic fields. As discussed in chapter 4, it was the “out of saturation” condition that resulted in the increase in hysteresis loss of the circular button ferrite inductor.

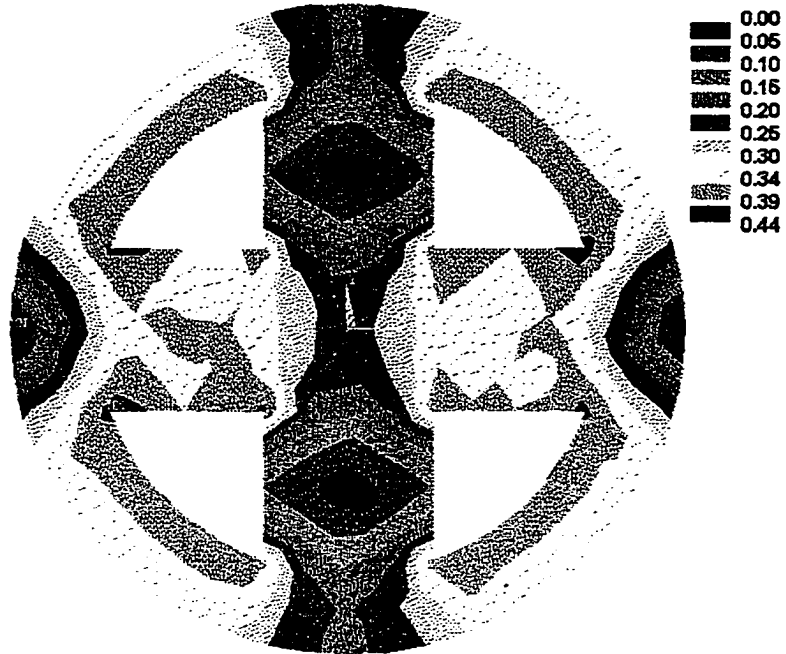


Figure 5-6 Distribution of magnetic induction without an orthogonal current.

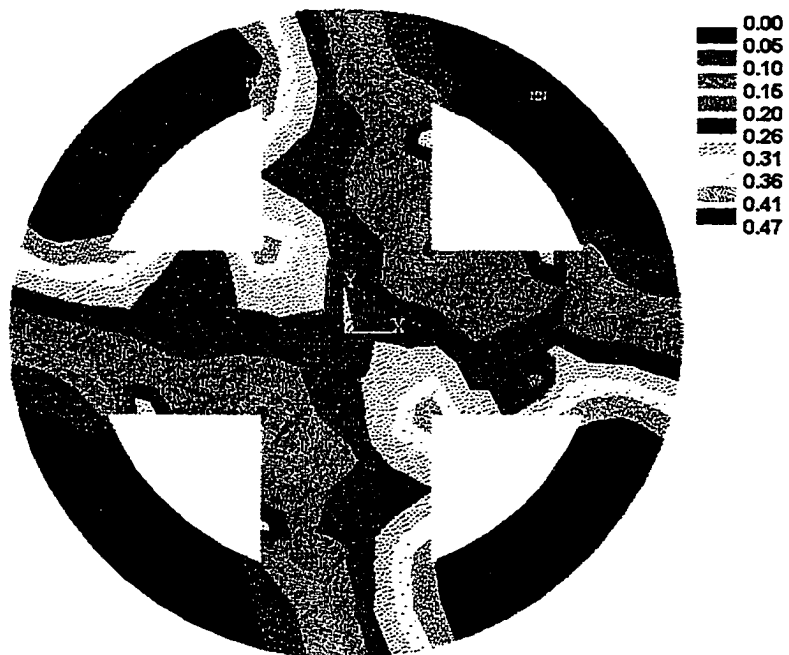


Figure 5-7 Distribution of magnetic induction with identical excitation current and orthogonal current.

#### 5.2.4 Field distribution in the prototype variable inductor

The method of finite element modeling used in this problem was the same as the techniques discussed above except for different geometry and magnetic parameters, which were taken from the product catalog of ferrite cores. Figure 5-8 shows the finite element model of the prototype variable inductor with excitation coils of 10 turns and orthogonal coils of 40 turns.

Figure 5-9 shows the flux density distribution only with an orthogonal magnetomotive force of 40 Ampere-turn. As expected, all edge paths were in saturation, and the two main paths remained in the low magnetization state. Figure 5-10 shows the flux density distribution with an orthogonal MMF of 40 Ampere-turn and an excitation MMF of 20 Ampere-turn. Without the orthogonal current, the excitation MMF of 20 Ampere-turn would be enough to saturate the main path. In the presence of the strong orthogonal MMF which magnetized all four quarter paths into deep saturation. However, the flux density in the main paths remained low. Because the saturation in the quarter

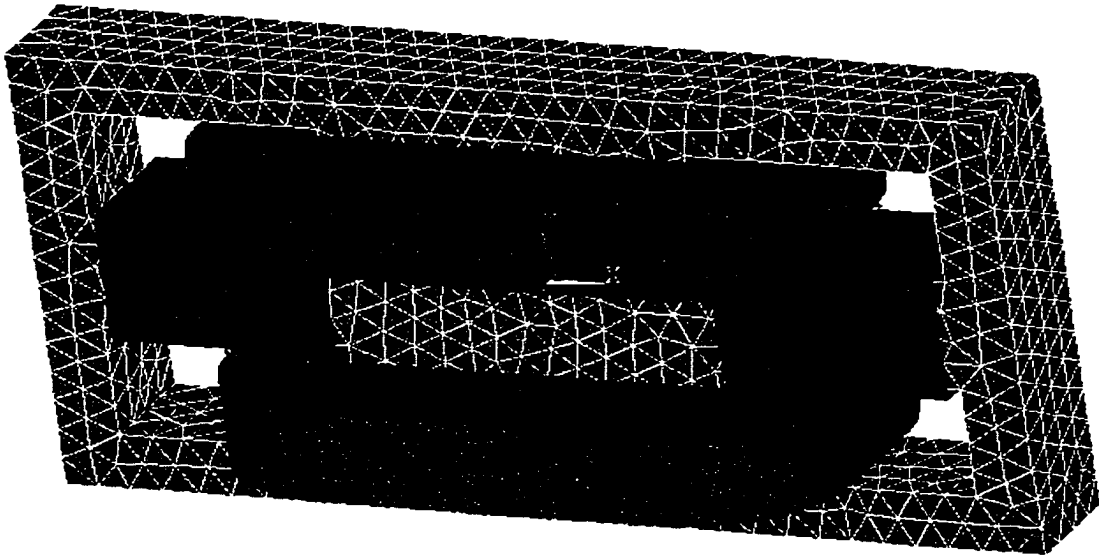


Figure 5-8 Finite element model of the prototype variable inductor.



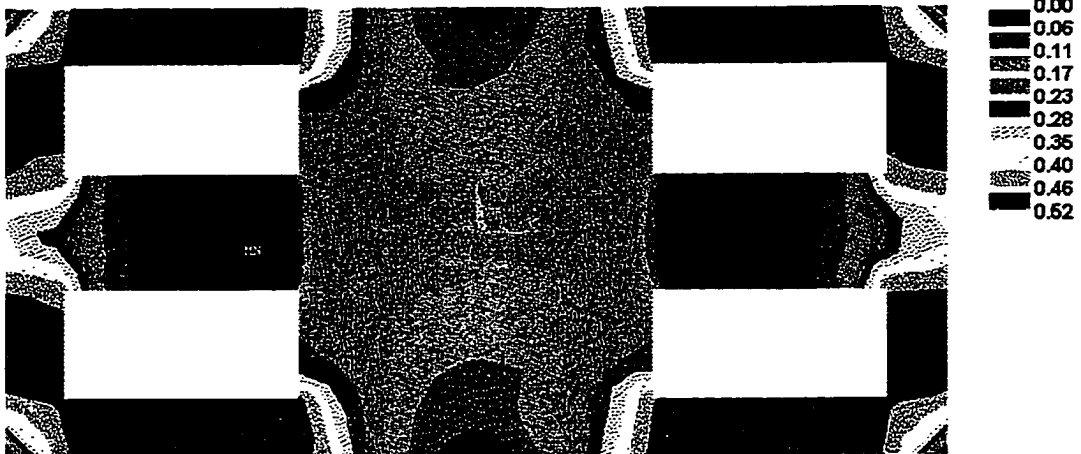


Figure 5-9 The distribution of magnetic induction of tester under only orthogonal current.

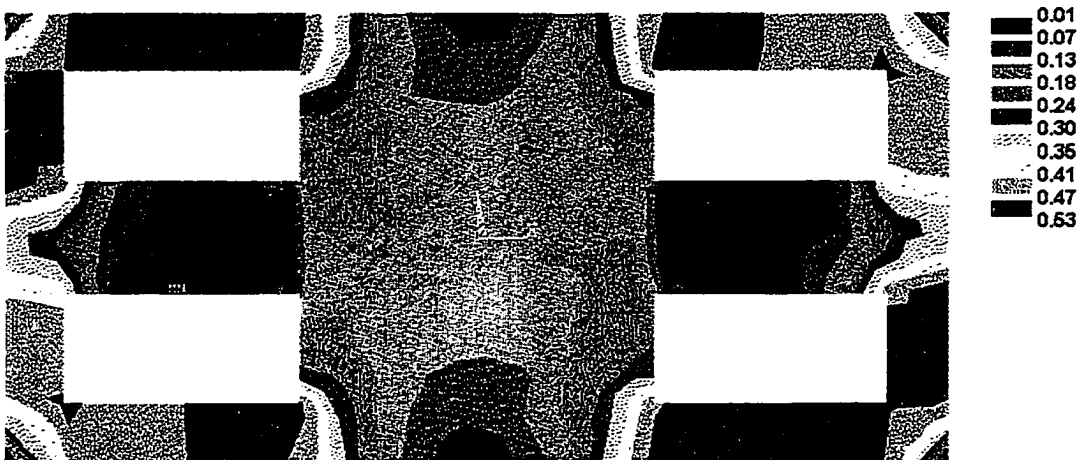


Figure 5-10 The distribution of magnetic induction under the action of both orthogonal current and excitation current.

paths effectively removed the magnetic material from the quarter paths, the strong demagnetizing effect reduced the magnetization to a very low value. On the other hand, in the regions where two fluxes canceled each other, the magnetization was slightly decreased but still near the saturation.

### 5.3 Inductance modeling of variable inductor

As discussed in chapter 4, experimental results showed that inductance of the circular button ferrite inductor and rectangular prototype variable inductor can be reduced by a factor of 10 by the orthogonal current. The objective of this modeling was to investigate whether the finite element modeling can model this behavior. If the finite element modeling can be shown to correctly predict the properties of these devices, it will provide a useful tool for future design of this type of inductor.

In this study, the linear 3D finite element analysis was not found to be able to simulate the change in inductance with increasing orthogonal current. In linear FEM analysis, since the two fields are independent of each other, a change in one MMF does not affect the distribution of magnetic field created by another MMF although the total field changes. As discussed in chapter 4, it was the saturation created by the orthogonal MMF that was believed to be responsible for the decrease in the inductance and the saturation is a typical nonlinear property of ferromagnetic materials. It was not surprising therefore that the linear finite element modeling failed to simulate the inductance change of the variable inductors.

#### 5.3.1 Modeling of inductance

For an FEM modeling using vector potential formulation, ANSYS can simulate terminal inductance of a strand coil because of the simple curl relationship between flux density  $\mathbf{B}$  and vector potential  $\mathbf{A}$ . However, for FEM modeling using Generalized Scalar Potential formulation, ANSYS was unable to simulate the terminal inductance of an

inductor. In this study, the inductance modeled by Generalized Scalar Potential formulation was modeled using ANSYS Parametric Design Language.

Since the distribution of flux density  $B$  was available after an FEM simulation, the summation of the line integrals of the normal component of the flux density  $B$  along many uniformly distributed straight lines on a cross section of interest should give the total flux pass through the cross-section. Once the flux is available, the terminal inductance can be obtained by multiplying the flux with the number of turns of excitation coil, and dividing the product, flux linkage, by the excitation current. Considering the fact that the measured inductance was the series inductance of the two excitation coils, the flux passing through each excitation coil was first evaluated and then the average flux was used to calculate the inductance of the inductor by multiplying the total turn number of the excitation coils and dividing by the main current.

There were two currents involved in the variable inductor, the excitation current and the orthogonal current. The flux was created of course by both currents. Only the main excitation current was used in the evaluation of the inductance since the inductance was actually measured at the main excitation coil. In order to simulate the inductance change with the orthogonal current, the inductance simulation was repeated at various orthogonal currents.

### 5.3.2 Inductance of the orthogonal mode variable inductor

Figure 5-11 shows the change in the modeled initial inductance, which was the flux linkage created by a small excitation current divided by the small excitation current, against the orthogonal current. The permeability and saturation input into the FEM

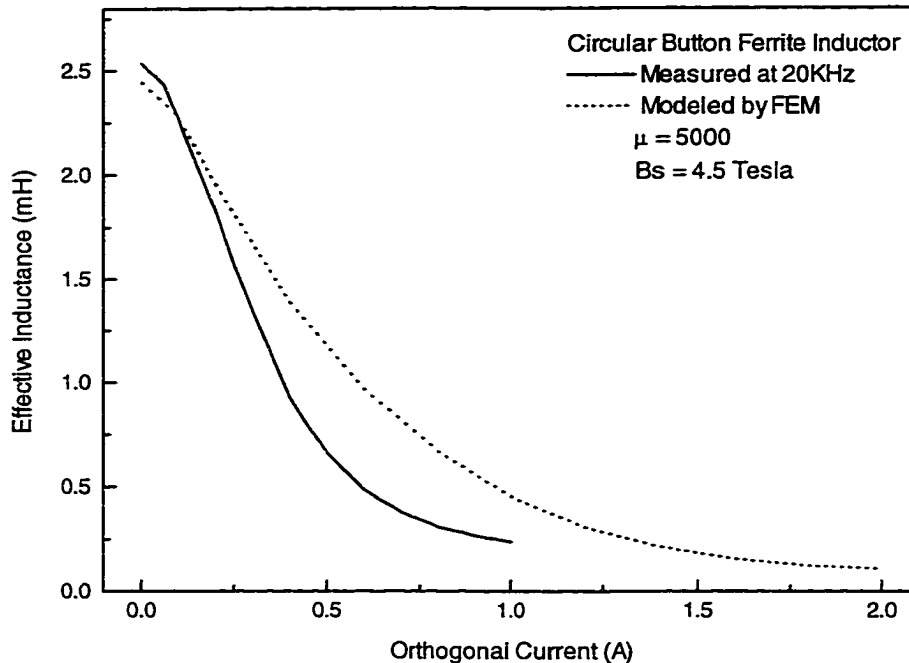


Figure 5-11 The modeled initial inductance of the circular button ferrite inductor under different orthogonal currents.

modeling were 5000 and 0.45 Tesla, respectively, which were obtained from the experimental data provided by the manufacturer of the circular button ferrite inductor. For the purpose of comparison, the inductance measured on the real circular button ferrite inductor is also plotted in the same figure.

Starting from an approximate same value of inductance, both measured and modeled inductance decreased as the orthogonal current was increased. With a strong enough orthogonal current, both measured and modeled inductance approached approximately the same inductance. However, the change rate of modeled inductance under the action of an orthogonal current was slower than that of measured inductance. The difference is believed to result from the fact that the FEM modeled inductance was actually the DC inductance without considering the frequency dependence of magnetic

materials and a simplified magnetization curve was used in the FEM modeling while the real ferrite exhibits hysteresis.

### 5.3.3 Inductance variation of the testing variable inductor

Figure 4-10 shows the measured inductance of the prototype variable inductor versus the excitation current under various orthogonal currents. The objective of this FEM inductance modeling was to study whether the nonlinear FEM can model the change in inductance against not only the orthogonal current but also against the main excitation current. The geometry parameters for the FEM modeling were taken from the product catalog of Magnetics, Inc., using the P-42515 "E" core and P-42516 "T" core. The input permeability and saturation were 2500 and 0.5 Tesla, respectively, which were also taken from the same catalog.

At the beginning of the inductance simulation, which used the given geometry of the testing inductor, the modeled initial inductance at zero orthogonal current was twice the experimental value. Based on the analysis of the data on the effective cross sectional area  $A_e$ , path length  $L_e$  and inductance factor  $A_L$ , provided by the manufacturer, it was believed that there was an air gap of total about 0.001 inch in the magnetic circuit, which might result from imperfect surface contact between different pieces of the ferrite core. It was this air gap of 0.001 inch that resulted in the difference between the measured inductance and modeled inductance. After including two air gaps of 0.0005 inch in the FEM model, the modeled initial inductance at zero orthogonal current was found to agree with the measured initial inductance.

Figure 5-12 shows the modeled initial inductance (small main current inductance) of the prototype variable inductor against the orthogonal current. For comparison, the measured inductance for the same inductor is also plotted in the figure. The modeled initial inductance at zero orthogonal current and large orthogonal current showed good agreement with measured initial inductance. However, the decrease in the modeled initial inductance with orthogonal current was slower than that observed in practice.

Figure 5-13 shows the modeled direct inductance, which was the flux linkage divided by the main current, against the main current at different values of orthogonal current. In the absence of an orthogonal current, the modeled inductance decreased with increasing main current as observed experimentally. This is believed to result from the saturation, which reduced the effective permeability, in the main flux path under the action of the main current. At an orthogonal current of 0.5A, the modeled inductance increased with increasing main current. Since the fluxes created by the two currents canceled each other in the first quarter path and the third quarter path, the orthogonal magnetomotive force reduced the magnetization in the two regions and therefore increased the effective permeability in the main flux circuit. The effective inductance therefore increased with increasing main current. At an orthogonal current of 1.0A, the modeled inductance showed only a slight increase as observed in experimental results. The strong orthogonal MMF magnetized all four quarter paths into deep saturation, the main MMF only had a slight effect on the deep saturation state. A slight increase in both modeled inductance and measured inductance was therefore observed.

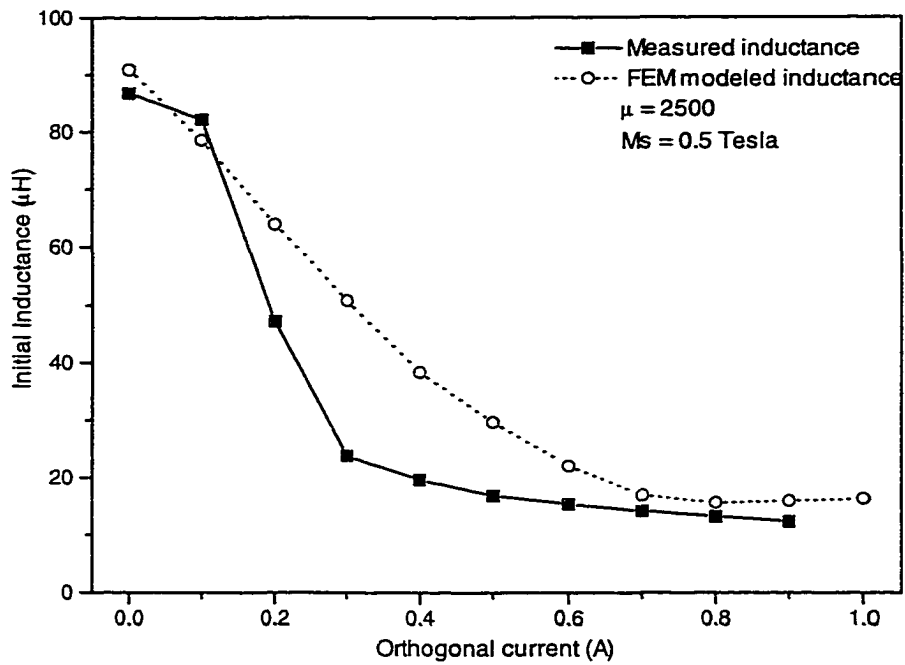


Figure 5-12 The modeled initial inductance of the prototype variable inductor against the orthogonal current.

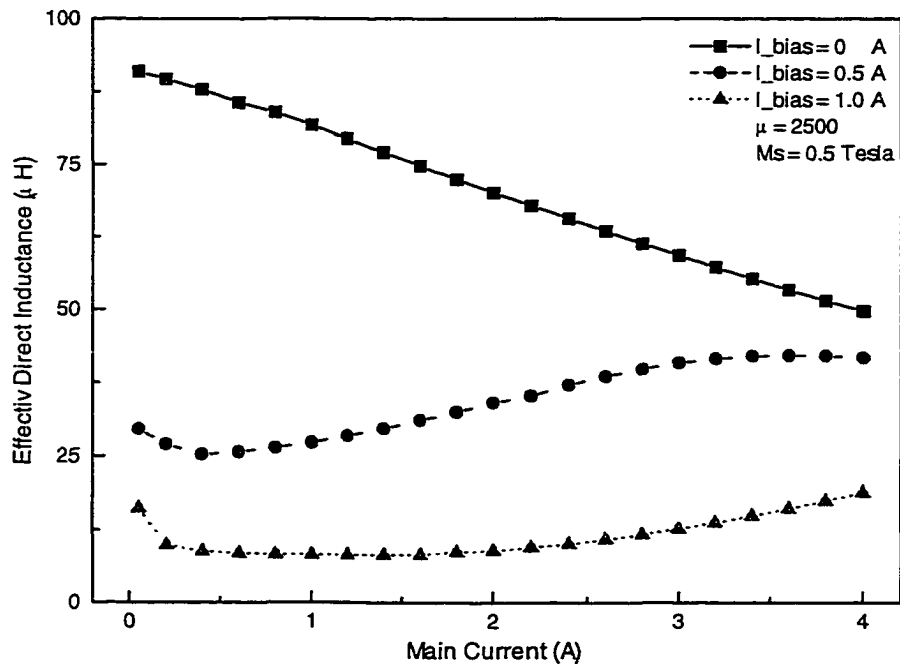


Figure 5-13 The modeled direct inductance of the prototype variable inductor against the main current at different orthogonal currents.

The inductance measurements at different main currents were actually made by measuring the inductance under different DC bias currents, which was the incremental inductance around a DC bias current. In this study, the incremental inductance was also modeled by dividing the increment of the flux linkage by the increment of the main current. Figure 5-14 shows the modeled incremental inductance against the main current at different orthogonal currents. At zero orthogonal current, as observed in Figure 4-10, the modeled inductance decreased with increasing main current. At an orthogonal current of 0.5A, as the main current increased, the inductance increased first, then decreased. At an orthogonal current of 1.0A, the modeled inductance had a constant inductance plateau as observed in experimental results.

However, the inductance at a main current of 4.0A at different orthogonal current did not agree with the experimental results. This was believed to be due to the fact that

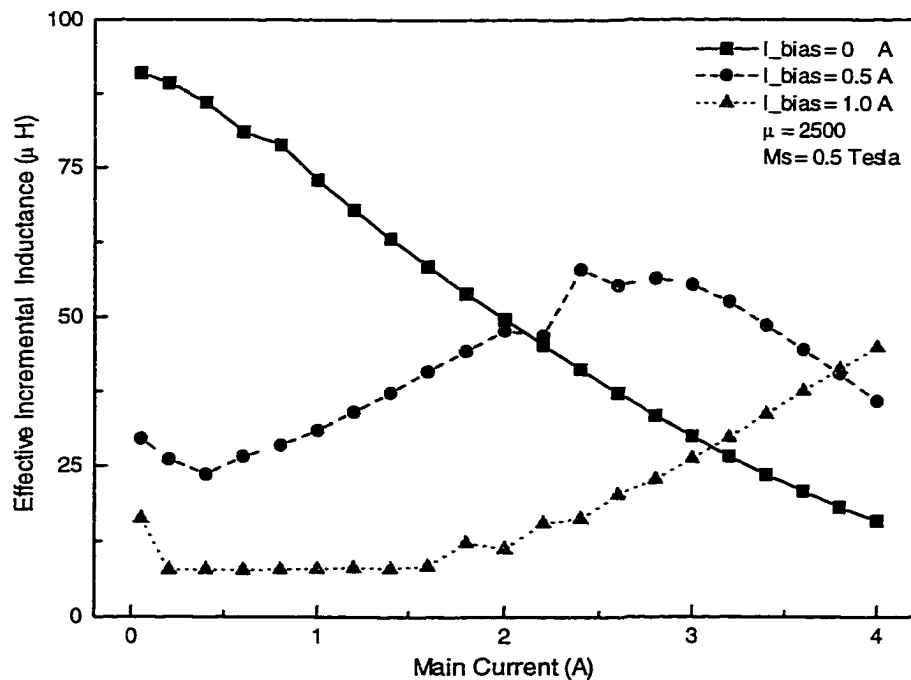


Figure 5-14 Effective incremental inductance against main current at different orthogonal current.



the real device was assembled using five separate pieces of ferrite core. The contact between different pieces was not perfect, probably resulting in air gaps and the associated reluctance affected the measured inductance. Additionally since the main flux had to go through 8 contact interfaces to complete a close path while the orthogonal flux only had to go through 2 contact interfaces, the contact reluctance had a stronger effect on main path than on the orthogonal path. Because of its random nature and very thin thickness, the contact air gaps were difficult to model in a finite element modeling.

#### **5.4 Conclusion**

Finite element modeling was extensively used as a numerical tool to analyze and solve problems involved in this study. Taking advantage of the axial symmetry, 2D linear FEM was used to evaluate the internal orthogonal field along the axial direction of a toroid. The FEM modeling indicated that the field inside specimen was not uniform and the spatially averaged field was only a small fraction of the external field. 2D linear FEM showed that the presence of an orthogonal MMF profoundly altered the flux distribution of the circular button ferrite inductor. With increasing orthogonal MMF, the direction of vector sum in the center of the device rotated from the horizontal direction to the vertical direction.

Based on a phenomenological model which can be derived from the quantum theory of paramagnetism, the modeled distribution of flux density using 3D nonlinear finite element modeling showed the expected saturation in the region where the two fluxes created by the excitation current and orthogonal current on the same direction. Using a programming method developed in this study using ANSYS Parametric Design Language, the inductance of a 3D magnetic device implemented by Generalized Scalar

Potential method can be modeled. The modeled inductance showed the experimentally observed variation under various main currents and orthogonal currents. The modeled results of initial inductance without an orthogonal current were also found to be consistent with the experimental results.

## 6. GENERAL CONCLUSION

In this study the orthogonal field effect and its applications have been systematically investigated experimentally, theoretically and numerically.

Hysteresis measurements on non-conducting ferrite, conducting polycrystalline silicon iron sheet and conducting amorphous Fe-Si-B ribbon showed that an orthogonal field rotated the hysteresis loop clockwise and reduced the enclosed area. As a result, the hysteresis loss and the effective permeability along the field direction decrease with increasing orthogonal field. The orthogonal field effect is a general effect of magnetic materials. The experimental results, including fixed field amplitude measurements and fixed induction amplitude measurements on ferrite devices, indicated that the orthogonal field reduced the hysteresis loss by increasing the component of the reversible domain rotation. The effect was more pronounced as both excitation field and orthogonal field were increased.

Derived from the domain wall motion of magnetization and based on isotropic Langevin-Weiss anhysteretic magnetization model, the Jiles-Atherton model has been used to successfully model the hysteresis of soft and hard magnetic materials. In this study, the extension of the one-dimensional isotropic model to quasi-two-dimensional magnetization has been investigated. The orthogonal field was considered as an anisotropy in affecting one-dimensional anhysteretic magnetization so that the well developed one-dimensional model can be used to model the orthogonal field effect. Although the modeled hysteresis loop successfully modeled the experimentally observed loop rotation under the action of an orthogonal field, the fact that the modeled hysteresis loop failed to show the observed decrease in hysteresis loss indicated that the dynamically

increased reversible domain rotation component should also be incorporated into the extended model. A dynamically variable reversibility coefficient, which models the change in reversibility coefficient  $c$  during the magnetization process and can be characterized by an irreversible field range, was proposed in this study to include the reversible domain rotation magnetization under the action of an orthogonal field. After incorporating the variable reversibility coefficient into the extended hysteresis model, the modeled hysteresis loops about the orthogonal field effect showed all experimentally observed features. Due to the strong demagnetizing effect, the internal orthogonal field inside a ferrite toroid along the axis direction was only a small fraction of the external orthogonal field. Due to the limited magnetic moments of magnetic materials, the coupled demagnetizing effect caused the internal orthogonal field dynamically increased with increasing excitation field. After incorporating the increased internal orthogonal field into the extended hysteresis model, the modeled hysteresis curves showed a good agreement with experimental results.

The inductance measurements on the circular button ferrite inductor showed that the measured small current inductance can be reduced by a factor of 10 by changing the orthogonal current. Measurements on the small field permeability of the same device were consistent with the results. However, hysteresis measurements on the circular button ferrite device showed an increase in hysteresis loss in the presence of an orthogonal field. It was the saturation created by the orthogonal field that is believed to give rise to the variable inductance and increased core loss. The saturation resulted from the orthogonal field in the circumferential path regions reduced the overall permeability of the device, and the inductance therefore decreased with increasing orthogonal field as a result. It was the cancellation of two magnetic fluxes created by both orthogonal field and excitation

field that pulled magnetization out of reversible saturation region into the irreversible magnetization region and resulted in the increase in hysteresis loss. Either a small excitation field and a strong orthogonal field could be used to improve the core loss. Based on the above experimental observation, and utilizing the selected saturation, a prototypic un-gapped ferrite variable inductor was proposed, in which a strong orthogonal magnetomotive force was applied to magnetize the circumferential path into deep saturation and to magnetically remove the circumferential paths so that a strong demagnetizing effect reduces the effective permeability significantly and increases the energy storage of the device. The inductance measurements on an assembled prototype rectangular button ferrite inductor based on the above design confirmed the expected behavior. The measured inductance not only was observed to decrease with increasing orthogonal current, but also with an appropriate orthogonal current, an inductance plateau, where the effective inductance only had small fluctuation within a designed working current range, was observed. The hysteresis measurements on an identical device showed that the core loss can be reduced to a small value with strong orthogonal current.

Finite element modeling was extensively used as a numerical tool to analyze and solve problems involved in this study. In this study 2D linear FEM modeling was used to evaluate the distribution of flux lines of the Circuit Board Embedded Ferrite Inductor, the internal orthogonal field along the axial direction of a toroid, and the interaction of two fluxes created by excitation coil and orthogonal coil in the circular button inductor. Using a phenomenological model which can be derived from the quantum theory of paramagnetism, the modeled distribution of flux density using 3D nonlinear finite element modeling showed the expected saturation in the region where the two fluxes created by the excitation current and orthogonal current were on the same direction.

Programmed by the ANSYS Parametric Design Language, the inductance of button ferrite inductors involved in this study was numerically evaluated using 3D nonlinear FEM modeling. The modeled inductance showed the experimentally observed variation under various excitation currents and orthogonal currents. The modeled results of initial inductance without an orthogonal current were also found to be consistent with the experimental results.

**APPENDIX****Nondestructive evaluation using magnetic techniques**

- [1] "Dependence of magnetic properties on crack size in steels",  
Y. Bi and D.C. Jiles,  
*IEEE Transactions on Magnetics*, Vol. 34, No. 4, p.2021, 1998.
- [2] "The Dependence of Magnetic Properties on Fatigue in A533B Nuclear Pressure Vessel Steels",  
Y. Bi, M. R. Govindaraju and D. C. Jiles,  
*IEEE Transactions on Magnetics*, Vol. 33, No. 5, p. 3928, 1997.
- [3] "Detection of Fatigue Crack propagation in Steel using Magnetic Measurements",  
Y. Bi and D.C. Jiles,  
*Review of Progress in Quantitative NDE*, Vol. 17, p. 1509, 1997.
- [4] "Magnetic Nondestructive Evaluation of Nuclear Pressure Vessel Steels for Fatigue Damage",  
Y. Bi, M. R. Govindaraju, S. B. Biner and D. C. Jiles,  
*Non-Destructive Evaluation and Materials Properties III*, eds., P.K. Liaw, O. Buck, R. J. Arsenault and R.E. Green, Jr., TMS, p. 115, 1996.

## Dependence of Magnetic Properties on Crack Size in Steels

Y. Bi and D.C. Jiles

Center for NDE, Iowa State University, Ames, IA 50011

**Abstract** — A crack induces a local inhomogeneity in the magnetic flux path in a material and any change in crack area results in change in the distribution of magnetic flux. From the results of measurements on A533B steel and Cr-Mo steels, not only were the magnetic properties found to change with crack area, but also a linear relationship between measured remanence and crack area was observed. A model equation has been developed which shows agreement with the observed relationship. On the other hand, the coercivity and its relationship to crack area were found to depend upon the sensor position relative to the crack. 3D finite element analysis of the leakage field above a crack also showed the position dependence. Therefore, using the remanence measurement method described here fatigue damage and crack area in steel components can be evaluated nondestructively.

**Index Terms** — Crack area measurement, finite element method, leakage field, nondestructive evaluation, steels.

### I. INTRODUCTION

The fatigue cracks or other pre-existing cracks could lead to sudden, sometimes catastrophic, failure of structural components. Crack detection and crack area evaluation therefore are critically important for some components that are subjected to cyclic stress. The nondestructive detection and evaluation of these cracks are highly desirable from the viewpoint of safe and economic operation of installed facilities such as power plants.

Magnetic techniques have been shown to be useful for crack detection in steel [1] and to be sensitive to the microstructural changes induced by cyclic stress [2, 3]. Once the crack is formed, the quantitative evaluation of crack area or crack length is important in order to estimate fatigue damage or to study the propagation of fatigue cracks.

Several techniques have been developed for evaluation of fatigue crack area, such as the electrical potential drop method [4] which is widely used in the study of propagation of fatigue cracks. The electrical potential drop method is based on the fact that the discontinuity induced by a crack disturbs the electrical field in a current-carrying body and the magnitude of the disturbance is determined by the size and shape of the crack. On the other hand, the discontinuity resulting from a crack also produces disturbance to the distribution of magnetic field and the magnitude of the disturbance is determined by the size and shape of the crack. Therefore, it should be possible to evaluate the crack area by magnetic measurements.

A quantitative logarithmic relationship between fatigue damage and coercivity was observed by Chen et al [5] in

load-controlled low-cycle fatigue tests. An approximately linear relationship between mechanical modulus of fatigue specimens and magnetic remanence was recently reported in strain-controlled fatigue tests[6]. However, it was difficult to quantitatively evaluate the fatigue crack area using magnetic techniques. In this paper a new method based on the measurement of remanence is presented to evaluate the crack area of a steel component with a limited cross sectional area.

### II. MATERIALS AND EXPERIMENTAL PROCEDURES

The materials involved in this study were service aged commercial steels: A533B nuclear pressure vessel steel and Cr-Mo piping steel. The materials were machined into an hour glass shape with a diameter of 6 mm at the center of the specimen. A slow diamond saw was used to create the crack so that the crack area could be well controlled and the effect of localized stress, which is usually associated with a fatigue crack tip, could be ignored. At a predetermined interval, the cutting was halted and magnetic hysteresis measurements were made at different positions around the crack. Other specimens of the materials were machined into a cylindrical shape with a diameter of 8 mm so that the surface sensor could be moved along the axis of the specimens and the changes in magnetic properties around the crack along the axis direction could be measured.

The magnetic measurements were made using shape-fitted surface sensors. In the sensors soft iron C-cores with a span of 25 mm were used to generate magnetic fields in the specimens and measure the magnetic flux. A Hall device mounted at the center of the sensor was used to measure the magnetic field on the surface of specimen.

The dependence of magnetic properties on crack area was analyzed numerically using finite element modeling. In this study, 3D nonlinear finite element analysis with 10-node tetrahedral element under the Generalized Scalar Potential formulation was performed to study the magnetic field distribution and numerically calculate the leakage field detected by the Hall probe. The magnetization curve that the finite element modeling needed to perform nonlinear analysis was taken from the experimental results on the A533B steel and Cr-Mo steel, respectively.

### III. RESULTS AND DISCUSSION

The effect of crack area on coercivity of both A533B steel and Cr-Mo steel measured at the very top of the crack opening is shown in Figure 1. The plot shows the fractional change in coercivity relative to baseline coercivity which was measured before the crack was formed. It was noted that the measured coercivity first increased with the area of crack. When the crack area was about the 60% of the specimen cross

Manuscript received October 17, 1997.

Y. Bi, 515-294-5612, fax 515-294-8727, biying@ameslab.gov;

D. C. Jiles, 515-294-9685, fax 515-294-8727.

This work was sponsored by National Science Foundation under grant number CMS-9532056



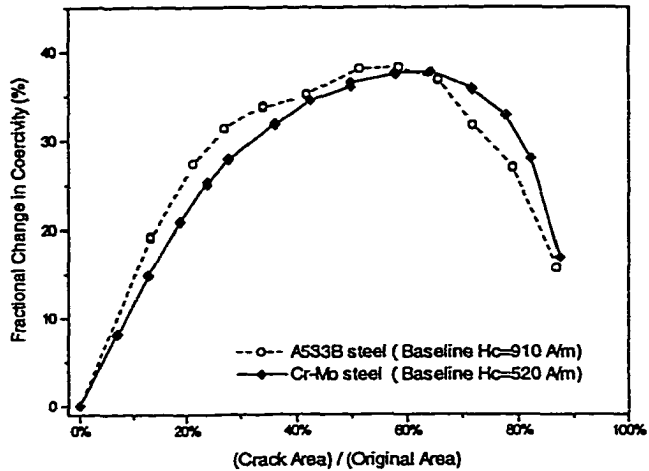


Figure 1 The effect of crack area on measured coercivity of A533B steel

sectional area, the measured coercivity showed a decrease with increasing crack area.

According to the configuration, the measured coercivity is the leakage field measured by the Hall probe when the magnetic flux in the magnetic circuit was zero. Therefore, the measured coercivity is determined by two factors. One is the coercivity of the specimen itself, another is the field leakage induced by the crack.

The crack forms a discontinuous interface for the magnetic flux. The crack changes the distribution of magnetic field and increases leakage field above the crack. Therefore, the leakage field increased with the crack area. This fact can be observed in the results of FEM calculations of the leakage field shown in Figure 2.

On the other hand, the crack causes the flux line to deviate from their original direction and reduces the magnetic flux density near the crack, which was observed in the 3D finite element analysis. Although most of the specimen was magnetized to saturation during a measurement, due to the deviation of the flux lines, material near the crack opening was not completely magnetized. The coercive force was measured instead. With the increase of crack area, the magnetic field in the material near the crack opening

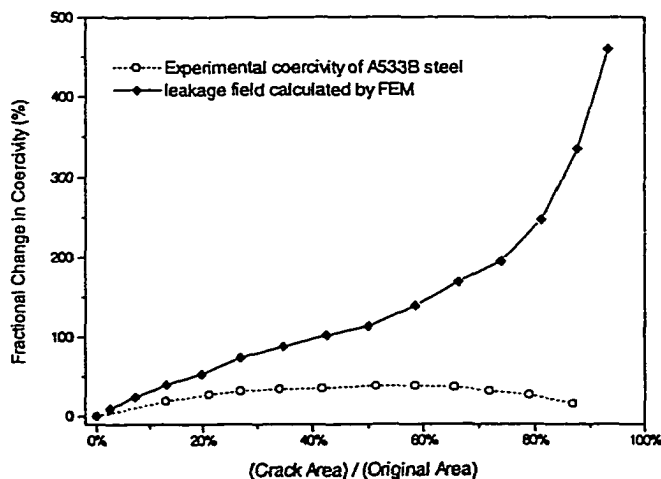


Figure 2 The effect of crack area on the leakage field calculated by finite element method

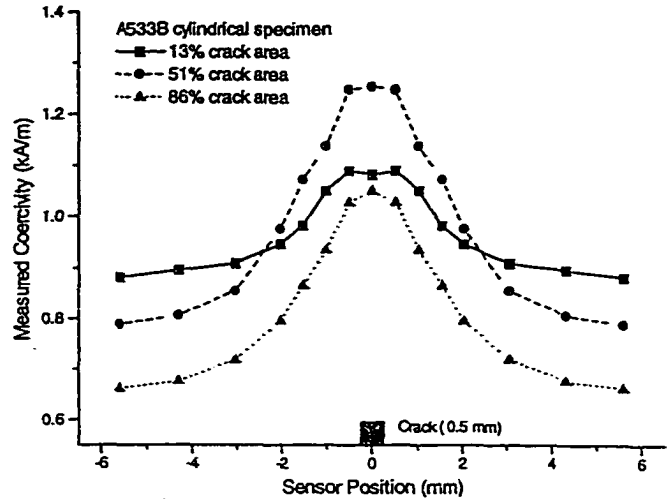


Figure 3 The measured coercivity around a crack in A533B steel

decreased, and the coercive force decreased.

When the crack area is small, the magnetic leakage field induced by the crack is a major factor affecting the measured coercivity. The measured coercivity was observed to increase with crack area. When the crack area is large, the coercive force decreased because of the inability to completely magnetize the part in the vicinity of the crack. Therefore, the measured coercivity decreased with increasing crack area after the crack area was more than 60% of the cross sectional area. From the viewpoint of nondestructive evaluation, this monotonic relationship for a small crack area is useful for early detection and evaluation of cracks.

The leakage field calculated using finite element modeling is also shown in Figure 2, where the experimental coercivity of A533B steel is shown for comparison. The leakage field showed a monotonic increase with the crack area. The difference between experimental coercivity and numerical leakage field is believed to be due to the fact that nonlinear finite element analysis performed in this study was based on the anhysteretic assumption, while the real specimens exhibited hysteresis. If hysteresis can be incorporated into finite element analysis, simulated coercivity is expected to decrease after the crack area exceeds a certain value.

Figure 3 shows the variation in measured coercivity at different positions relative to the crack along the axis of the specimen for different crack areas. The left halves of these curves were obtained by taking into account symmetry of the specimen. The results showed that the measured coercivity had its highest value at the very top of the crack, it then decreased rapidly with displacement from the crack position. Therefore, the measured or apparent coercivity is sensitive to crack location. The leakage field obtained by finite element analysis also showed the same general shape of curve when plotted against position.

The effect of a crack on the measured remanence is shown in Figure 4. After the crack was formed, an approximately linear relationship between crack area and measured remanence was observed and was less sensitive to crack position as long as the crack was under the C-core of the sensor.

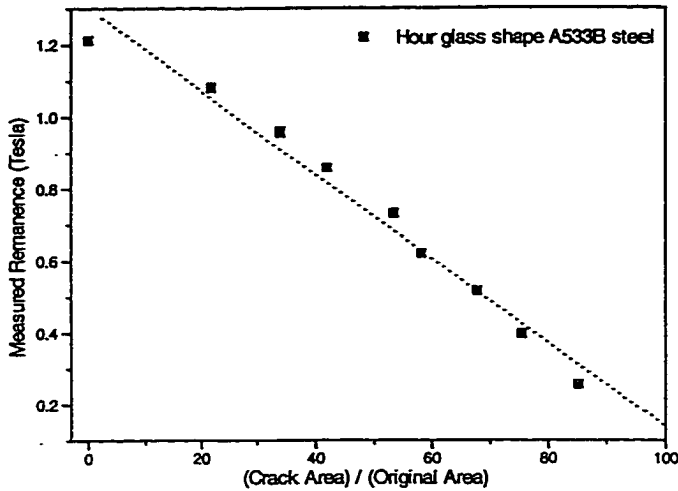


Figure 4 The effect of crack area on measured remanence in hour-glass shaped A533B specimens

The test material and sensor can be modeled as a closed magnetic circuit. The magnetic flux in the circuit was produced by the power coils on the C-core of the sensor. In magnetic measurements, the flux leakage was critical for coercivity measurement as discussed above. However, flux leakage is much less than the flux in the magnetic circuit. If the flux leakage is ignored for remanence measurements, the flux is the same at any cross section in the specimen. When magnetic hysteresis measurements were made, the specimens were magnetized to saturation. Due to the smaller cross-sectional area, the uncracked area has higher flux density and is magnetized to saturation first. After removing the external magnetic field, the remanent magnetic flux  $\Phi_0$  in the uncracked area  $S_R$  is equal to the flux  $\Phi'$  in any other cross-section of the specimen.

$$\Phi_0 = B_{r0}S_R = \Phi'$$

According to the configuration of the surface sensor used in this study, the measured remanence actually was the measured magnetic flux in the magnetic circuit when the applied magnetic field was zero, divided by the original area  $S_0$  of the specimen. The measured remanence  $B_{rm}$  therefore is:

$$B_{rm} = \frac{\Phi_0}{S_0} = \frac{B_{r0}S_R}{S_0} = \frac{S_0 - S_c}{S_0} B_{r0}$$

where  $B_{r0}$  is the remanence of the material without a crack present. This is a linear relation between crack area  $S_c$  and measured remanence. The relationships were observed directly in crack area controlled tests as shown in Figure 4 and were observed indirectly in previous fatigue tests [6].

According to the model, the linear relationship between the remanence and crack area is based the saturation assumption around the crack. Saturation of magnetization in the measured specimen is essential to this model. If magnetization is not saturated around the crack tip, the deviation from straight line behavior is expected and was observed in cylindrical specimens which had larger cross sectional area. Before a

crack was created, saturation first occurred at the interface between the C-core of the sensor and the specimen. Once the crack was formed, the measured remanence and crack area showed a linear relationship with the growth of crack because the inhomogeneity induced by the crack produced a high field concentration around the crack tip and this led to magnetic saturation in the uncracked area near the crack.

#### IV. CONCLUSIONS

Due to the local inhomogeneity induced by a crack, both magnetic field distribution and measured magnetic properties were found to change with the area of a crack. Determined by both leakage field and magnetic hysteresis, measured coercivity was sensitive to both crack position and area. The measured coercivity increased with crack area at first, but decreased with crack area once the crack area was more than 60% of the total cross sectional area. Determined by remanent flux in the specimen, the measured remanence was less sensitive to crack location. A linear relationship between measured remanence and crack area was observed and a model equation developed in this study which showed agreement with the linear relationship. Based on the anhysteretic assumption, 3D nonlinear finite element analysis about the leakage field above a crack showed a monotonic increase with the crack area. Because of its sensitivity to crack position, coercivity measurement can be used to detect a crack, while remanence measurement can be used to evaluate crack area based on the method presented here.

#### REFERENCES

- [1] D.C. Jiles, "Review of magnetic methods for NDE", *NDT International*, Vol 21, pp. 311, 1988.
- [2] M.S.C. Bose, "A study of fatigue in ferromagnetic materials using magnetic hysteresis technique", *NDT International*, 19, (2), pp. 83, 1986,.
- [3] M.K. Devine, D.C. Jiles, and S. Hariharan, "Effects of cyclic stress on the magnetic hysteresis parameters of polycrystalline iron" *Journal of Magnetism and Magnetic Materials*, 104, pp. 377, 1992.
- [4] A.A. Anctil, E.B. Kula and E. DiCesare, "Electrical potential technique for determining slow crack growth", in *Proceedings*, Vol 63, ASTM, Philadelphia, pp.799-808, 1963.
- [5] Z.J. Chen, D.C. Jiles, and J. Kameda, "Estimation of fatigue exposure from magnetic coercivity", *J. Appl. Phys.*, Vol. 75(10), pp. 6975, 1994.
- [6] Y. Bi, M.R. Govindaraju, and D.C. Jiles, "The Dependence of Magnetic Properties on Fatigue in A533B Nuclear Pressure Vessel Steels", *IEEE Trans. Magn.*, Vol. 33, No. 5, pp. 3928, 1997.

## The Dependence of Magnetic Properties on Fatigue in A533B Nuclear Pressure Vessel Steels

Y. Bi, M. R. Govindaraju, and D. C. Jiles  
Center for NDE, Iowa State University, Ames, IA 50011

**Abstract**—Cyclic loading causes cumulative microstructural changes in materials. The magnetic properties of A533B steel are determined by both initial microstructures and microstructural changes induced by fatigue damage. From the results of a series of strain-controlled fatigue tests, the magnetic properties were found to change systematically with fatigue damage throughout the fatigue life. A linear relationship between magnetic remanence and mechanical modulus was observed. The fatigue lifetimes were also dependent on the initial microstructure, and a relationship between these lifetimes and pre-fatigue magnetic properties such as coercivity was observed. Therefore this study has demonstrated that magnetic measurements can be exploited to evaluate the progress of fatigue damage in steel.

### I. INTRODUCTION

The evaluation of fatigue damage is critically important for some components which are subjected to severe operating stresses during their service lifetimes. In nuclear pressure vessel systems, the cyclic stress resulting from thermal expansion often creates a low-cycle fatigue condition. Therefore an evaluation technique which can monitor the progress of fatigue and predict the impending fatigue failure non-destructively is highly desirable for both safety and economy.

During fatigue there are continuous and cumulative microstructural changes in materials, such as the motion and redistribution of dislocations, formation of slip bands, nucleation and propagation of fatigue cracks[1]. The fatigue properties of a material, such as fatigue lifetime, are affected by the pre-existing microstructure. The magnetic properties of ferromagnetic materials are also sensitive to both initial microstructure and changes in microstructure produced by fatigue[2]. Bose[3] reported the variations in magnetic hysteresis properties with fatigue. Devine et al. [4] studied the effects of cyclic stress on the magnetic hysteresis parameters of polycrystalline iron and the detection of fatigue in structural steels by magnetic property measurements. Under low-cycle, load-controlled fatigue conditions, a simple logarithmic relationship between the coercivity and the number of stress cycles was observed by Chen et al [5]. With the results presented here, it is possible

Table I Chemical compositions for two A533B steels

	C	Mn	Cr	Si	Ni	Mo	Fe
Sample 1	0.22	1.45	0.06	0.22	0.56	0.50	Bal.
Sample 2	0.23	1.32	0.05	0.21	0.57	0.55	Bal.

to evaluate the accumulation of fatigue damage non-destructively using magnetic techniques.

Fatigue properties, such as fatigue lifetime, are closely related to the initial microstructure, such as grain size [6], and residual stress[7]. Magnetic properties of the material are also sensitive to microstructure and residual stress[8]. A relationship between fatigue lifetime and the initial magnetic properties was therefore expected. The objective of this study was to investigate this and also to study the relationship between mechanical property changes and magnetic property changes during fatigue under strain-controlled conditions.

### II. MATERIALS AND EXPERIMENTAL PROCEDURE

The materials involved in this study were service aged A533B nuclear pressure vessel steels, which were obtained from two different sources. They had similar chemical compositions as shown in Table I, but different microstructures, as shown in Figs.1 and 2. The fatigue specimens were machined into an "hour glass" shape with a diameter of 6.35 mm at the center of the specimen.

A series of strain-controlled low-cycle fatigue tests with 0.003 strain amplitude at a frequency of 2 Hz were conducted on the samples using a computer controlled 100KN servo-hydraulic MTS 880 system. Throughout the fatigue life at pre-determined intervals, fatigue cycling was halted under zero strain conditions. Magnetic measurements were made in-situ using a specially designed surface sensor

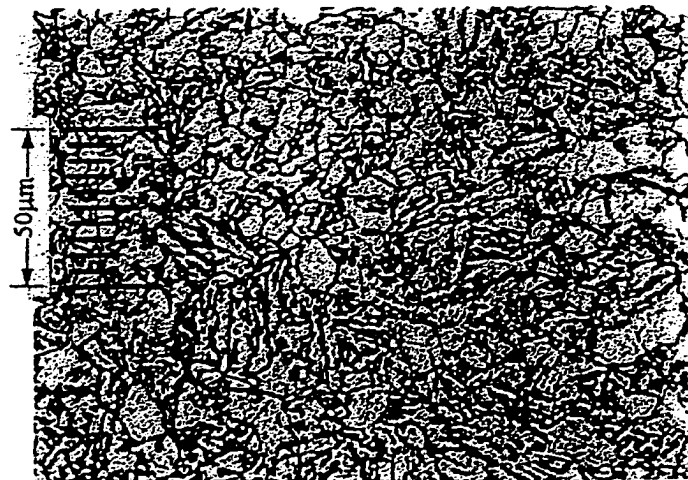


Fig. 1 Microstructure of sample 1.

Manuscript received January 30, 1997.

Y. Bi, 515-294-5612, fax 515-294-8727, biying@iastate.edu;

M. R. Govindaraju, 515-294-2395, fax 515-294-8727;

D. C. Jiles, 515-294-9685, fax 515-294-8727.

This research was sponsored by the US Nuclear Regulatory Commission under grant number of NRC-04-94-092 through the Center for NDE, Iowa State University, Ames, Iowa.

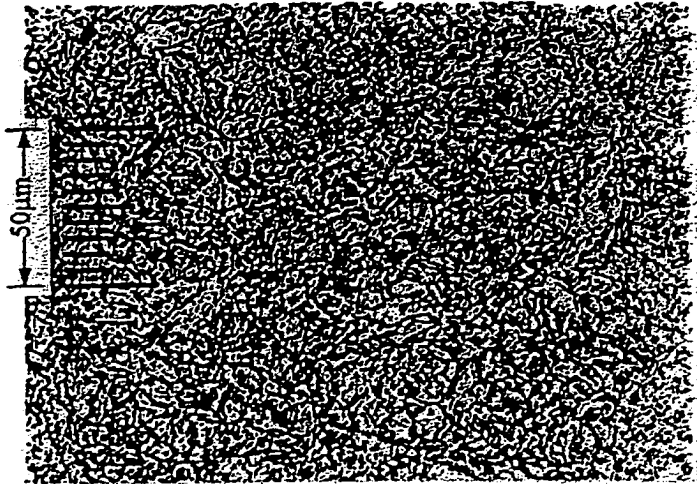


Fig. 2 Microstructure of sample 2.

Towards the end of fatigue life, the measurement interval was reduced so that the rapid changes in magnetic properties could be better observed.

### III. RESULTS AND DISCUSSIONS

Due to the microstructural difference, the two groups of steels exhibited significant differences in baseline magnetic properties, hardness and fatigue lifetime under the same strain-controlled fatigue conditions. The group of specimens with smaller grain size showed higher hardness, higher coercivity and shorter fatigue lifetime as shown in Table II.

The grain boundaries provide one type of pinning site. Pinning sites affect domain wall motion under the action of a magnetic field. The smaller grain size leads to larger grain boundary area, more pinning sites per unit volume, and hence a higher coercivity. The material with smaller grain size was also mechanically harder. Under stress-controlled fatigue, this higher hardness corresponds to a longer fatigue lifetime. However, under strain-controlled fatigue, the fatigue lifetime of smaller grain size was found to be significantly shorter than that of A533B steel with larger grain size, because higher stress is needed to reach the same strain on smaller grain size material.

A relationship between the baseline magnetic properties and their fatigue lifetime was observed on specimens machined from the first sample of A533B steel as shown in Fig. 3. Since these specimens had the same chemical compositions, the difference in baseline magnetic properties was attributed to the residual stress resulting from service aging, machining and polishing of the specimens. The residual stress affects the fatigue behavior of the samples [7] as well as their magnetic properties[8].

Since both baseline magnetic properties and fatigue lifetime are related to the microstructure in a complicated

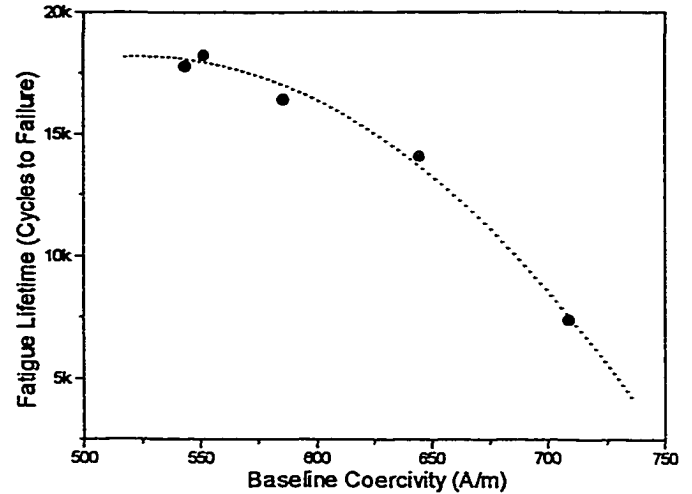


Fig. 3 Relation between the fatigue lifetime and baseline coercivity in one group of A533B steel.

way, an exact quantitative theoretical relationship between baseline coercivity and fatigue lifetime is not yet clear. In different groups of specimens, those with larger average coercivity had shorter average fatigue lifetime. Considering that fatigue lifetime can be affected by many factors, and also that surface conditions can significantly alter the fatigue lifetime, statistical deviations from the relationship from specimen to specimen were expected and were observed in this study.

A measurable mechanical parameter, the mechanical modulus which is the load needed to reach unit strain on per unit original area, was used to characterize the mechanical response of the specimen under the cyclic loading. Like the mechanical modulus, the magnetic properties were also found to change systematically with the dynamic microstructural changes induced by the fatigue cycling as shown in Fig. 4.

At the beginning of fatigue, during a process known as fatigue softening, the pre-existing dislocations in grains move to the grain boundaries. This decrease in dislocation density within the grains offers reduced resistance to further

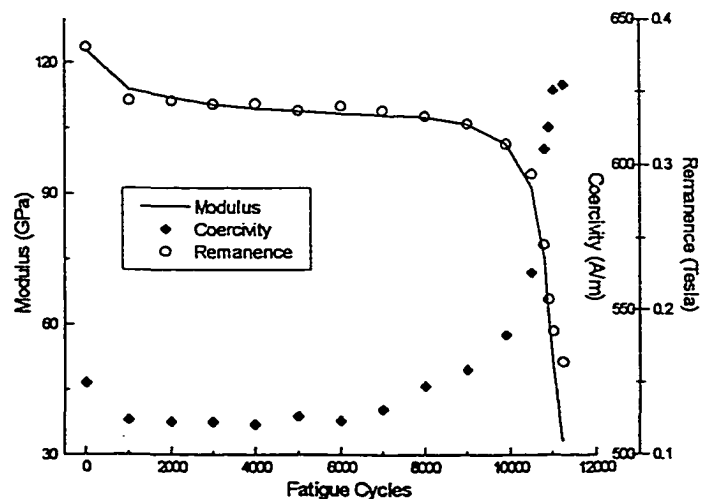


Fig. 4 Effect of fatigue damage on coercivity and remanence of A533B steel.

Table II The effect of microstructures on average magnetic properties, hardness and fatigue lifetime

	Grain size	Baseline Hc	Hardness	Lifetime
Sample 1	9 μm	590 A/m	RB83	14000 cycles
Sample 2	5 μm	710 A/m	RB91	3000 cycles

strain and decreased pinning site density for domain wall motion. Therefore, mechanical modulus, coercivity and remanence all decreased with strain cycling in the early stages of fatigue.

Corresponding to the stabilization of fatigue, the measured remanence also showed stabilization. It was noted that measured coercivity began to increase at about 70% of fatigue lifetime before modulus and remanence began to decrease. This was attributed to fatigue slip bands near the surface. Under cyclic loading, slip bands in the form of intrusions and extrusions were created near the surface. These slip bands, which are micro-discontinuity points, resulted in a magnetic leakage flux nearby. At the same time, these slip bands also acted as pinning sites to impede the domain wall motion near the surface. Therefore, the measured coercivity gradually increased with the build up of slip bands.

During the last stage of fatigue, because the propagation of the fatigue crack reduced the area bearing the applied load, the load needed to reach the same strain decreased. The measured modulus decreased with the propagation of the fatigue crack. On the other hand, the fatigue crack, which usually initiates at the surface and propagates from there, led to a planar discontinuity in the magnetic material. The discontinuity produced an increased leakage flux nearby. The measured coercivity, which is the measured magnetic field when the magnetic induction in the magnetic circuit is zero, increased after the propagation of a fatigue crack. On the other hand, the fatigue crack changed the distribution of the magnetic flux, causing demagnetization effects. Therefore the measured remanence decreased with the growth of the fatigue crack.

The observed relationship between the magnetic remanence and the mechanical modulus at all stages of fatigue life would seem to indicate a close relationship between the two mediated via the microstructural changes. In this study, an approximately linear relationship between mechanical modulus and magnetic remanence was found as

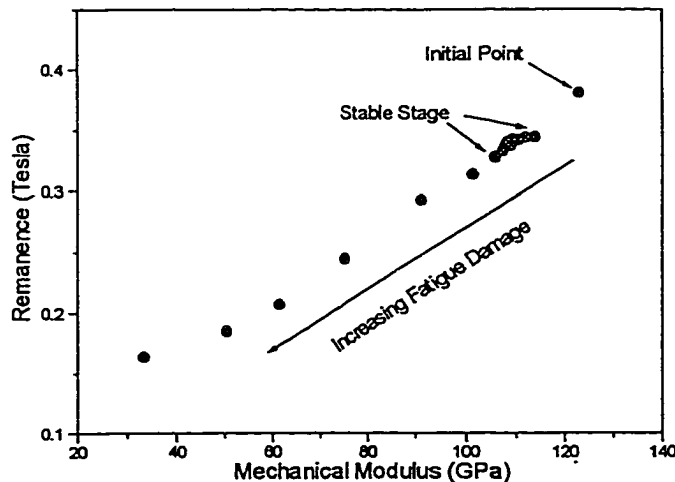


Fig. 5 Relation between mechanical modulus and magnetic remanence in strain-controlled fatigue on a specimen of A533B steel.

shown in Fig. 5.

#### IV. CONCLUSIONS

Since both fatigue lifetime and magnetic properties are affected by the pre-fatigue microstructures of steels, a relationship between fatigue lifetime and magnetic properties measured before fatigue may reasonably be expected. This was observed under strain-controlled fatigue on A533B steel.

The magnetic properties, such as coercivity and remanence, were found to change systematically with the continuous and cumulative microstructural changes induced by fatigue. An approximately linear relationship between mechanical modulus and remanence was observed in strain-controlled fatigue on A533B steel. The results of this study exhibited the feasibility and applicability of the magnetic inspection technique for NDE of fatigue damage.

#### REFERENCES

- [1] W.J. Harris, "The significance of fatigue", *Engineering Design Guides*, 14 (Design Council, Oxford University Press, 1976).
- [2] D.C. Jiles, "Review of magnetic methods for NDE", *NDT International*, 21 (1988), 311.
- [3] M. S. C. Bose, "A study of fatigue in ferromagnetic materials using magnetic hysteresis technique", *NDT International*, 19, (2), (1986), 83.
- [4] M.K. Devine, D.C. Jiles, and S. Hariharan, "Effects of cyclic stress on the magnetic hysteresis parameters of polycrystalline iron" *Journal of Magnetism and Magnetic Materials*, 104, (1992), 377.
- [5] Z. J. Chen, D. C. Jiles, and J. Kameda, "Estimation of fatigue exposure from magnetic coercivity", *J. Appl. Phys.*, 75(10), (1994).
- [6] A. W. Thompson and W. A. Backofen, *Acta Metall.*, vol. 19, pp. 597-606, 1971
- [7] J. O. Aïmen and P. H. Black, *Residual stresses and Fatigue in Metals*, McGraw-Hill Book company, New York, 1963.
- [8] D. C. Jiles, P. Garikepati, and D. D. Palmer. *Review of progress in Quantitative NDE*, 8B, 2081, 1989.

DETECTION OF FATIGUE CRACK PROPAGATION IN STEEL  
USING MAGNETIC MEASUREMENTS

Y. Bi and D. C. Jiles

Center for Nondestructive Evaluation  
Iowa State University  
Ames, IA 50011

INTRODUCTION

For structural components which are exposed to cyclic stresses, fatigue damage could lead to a catastrophic failure. In nuclear pressure vessel systems where A533B steel is widely used as structural material, cyclic thermal expansions often create a low-cycle fatigue condition. The evaluation of fatigue damage therefore is critically important and nondestructive evaluation of fatigue damage is highly desirable from the viewpoint of both safer and longer operation lifetime.

The mechanical properties of a material are determined by its microstructure. Under cyclic loading in materials there are continuous and cumulative microstructural changes, such as dislocation migration and redistribution [1]. The microstructural changes induced by fatigue cycling alter the mechanical response of a component to external cyclic loading. As the total number of stress cycles increases this leads to initiation and propagation of a fatigue crack. After the propagation of a fatigue crack, the increase in crack area reduces the actual area bearing the applied load and significantly changes the overall mechanical properties of the component until the final fatigue failure of the material.

On the other hand, the magnetic properties of steels are also determined by the microstructures of the materials, and are sensitive to the microstructural changes induced by the stress cycling [2]. The fatigue crack is a discontinuous boundary for magnetic flux. The propagating fatigue crack therefore changes the distribution of magnetic flux as well as the measured magnetic properties. It is possible to nondestructively evaluate the fatigue damage using magnetic measurements, since both microstructural changes induced by fatigue and fatigue crack propagation lead to changes in measured magnetic properties.

The variations in magnetic hysteresis properties with fatigue were reported earlier by Bose [3], and by Shah and Bose [4]. Devine et al. [5, 6] studied the effects of cyclic stress on the magnetic hysteresis parameters of polycrystalline iron and used this for detection of fatigue in structural steels through magnetic property measurements.

Govindaraju et al. [7] found significant magnetic property changes at the end of low-cycle fatigue when magnetic measurements were made under zero load condition. Chen et al. [8] found a simple logarithmic relationship between the coercivity and the number of stress cycles under low-cycle, load-controlled fatigue conditions, which could be used to determine the condition of the material or its proximity to fatigue failure.

Since both magnetic properties and mechanical properties are altered by the microstructural changes induced by fatigue cycling, a relationship between a mechanical property and a magnetic property is expected. In this study, from a series of fatigue tests on A533B nuclear pressure vessel steel and Cr-Mo piping steel, magnetic properties, such as coercivity, remanence, hysteresis loss and Barkhausen emissions, were found to change systematically with fatigue damage. Particularly, during the propagation of a fatigue crack, significant changes in magnetic properties were observed.

From the viewpoint of quantitative nondestructive evaluation, this relationship, particularly a monotonic one, is highly desirable. In this study, an approximately linear relationship between mechanical modulus and magnetic remanence was observed. Based on the results presented in this paper, the fatigue damage of steel components, as well as any ferromagnetic material, can be evaluated nondestructively using magnetic measurements, particularly, remanence measurements. A model equation, which was developed in this study based on the hysteresis of ferromagnetic material, also shows the linear relationship.

#### MATERIALS AND EXPERIMENTAL PROCEDURES

Two service aged commercial steels: A533B nuclear pressure vessel steel obtained from Oak Ridge National Laboratory and Cr-Mo piping steel obtained from General Atomics, were involved in this study. Their chemical compositions were shown in Table 1. The fatigue specimens were machined into an "hour-glass" shape with a diameter of 6.35 mm at the center of the specimen.

These fatigue specimens were subjected to low cycle fatigue using a computer controlled 100 KN servo-hydraulic MTS 880 system under strain-controlled mode with a strain amplitude of 0.3% at a frequency of 2 Hz. Mechanical parameters, such as load amplitude, were collected by the system automatically. Throughout the fatigue life at pre-determined intervals, fatigue cycling was halted under zero strain conditions. Magnetic measurements were made in-situ using a specially designed surface sensor which fitted the shape of the fatigue specimen. Towards the end of the sample fatigue life, the measurement interval was reduced so that any rapid changes in magnetic properties could be better observed.

In this study, a measurable mechanical parameter, mechanical modulus  $Y_m$ , the nominal stress needed to produce unit strain, was used to characterize the mechanical

Table 1 Chemical compositions of steels involved in this study.

	C	Cr	Mo	Si	Ni	Mn	Fe
A533B steel	0.223	0.06	0.50	0.22	0.56	1.45	Bal.
Cr-Mo Steel	0.0896	2.00	1.03	0.37	0.13	0.50	Bal.

Table 2 The effect of microstructures on mean magnetic properties, stable modulus, hardness and fatigue lifetime.

	Grain size	Baseline Hc	Baseline Br	Stable Modulus	Rockwell Hardness	Fatigue Lifetime
A533B Steel	5 $\mu$ m	7.4 Oe	0.37 T	103 GPa	B85	15 k
Cr-Mo steel	13 $\mu$ m	4.9 Oe	0.25 T	67.4 GPa	B60	16.2 k

response of the fatigue specimens under cyclic loading. The nominal stress was calculated by dividing the applied load by the original cross sectional area of the specimen.

FATIGUE TEST RESULTS AND DISCUSSION

Due to the difference in chemical compositions and grain size, the two steels showed significant differences in mechanical properties, such as Rockwell hardness and stable mechanical modulus during fatigue cycling; and baseline magnetic properties, such as remanence and coercivity, measured before subjected to fatigue cycling, as shown in Table 2. The Cr-Mo steel which had lower carbon concentration and larger grain size showed longer fatigue lifetime, lower mechanical properties and lower magnetic baseline properties than the A533B steel.

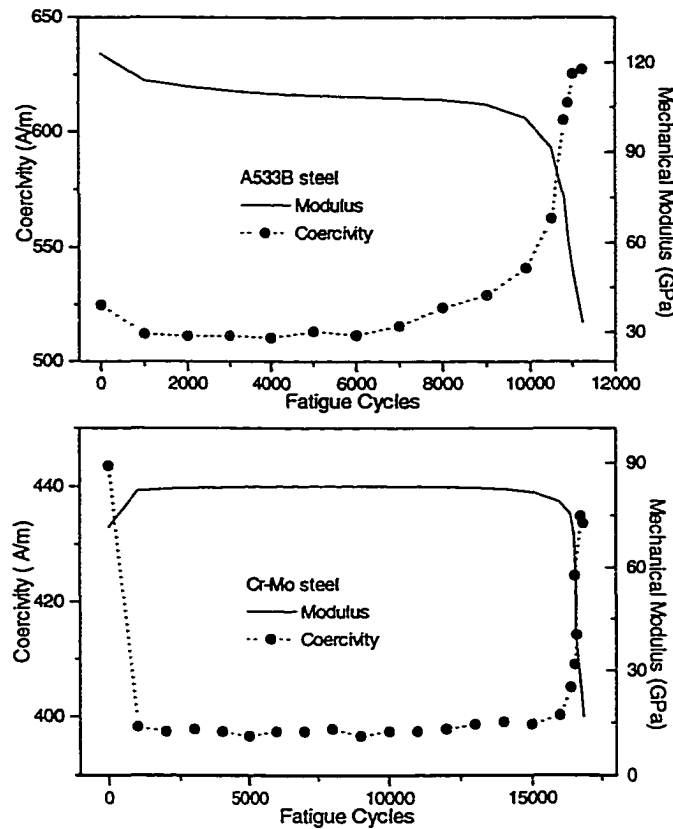


Figure 1 The effect of strain-controlled fatigue on coercivity in samples of A533B steel and Cr-Mo steel.



The material with high carbon concentration and large grain size was mechanically harder. This gave rise to a high stable mechanical modulus and Rockwell hardness in A533B steel. For magnetic domain walls, on the other hand, both carbide sites and grain boundaries acted as pinning sites to impede the domain wall motion under the action of a magnetic field. Lower carbon and larger grain size in Cr-Mo steel provided less pinning sites, leading to lower baseline magnetic properties, such as coercivity and remanence.

From the results of fatigue tests conducted in this study on both A533B steel and Cr-Mo steel, magnetic properties, such as coercivity and remanence, were found to change with fatigue damage throughout the whole fatigue life of the specimens as shown in Fig. 1 and 2. Specifically, towards the end of fatigue life, significant increase in coercivity and decrease in remanence were observed. After passing the initial stage of fatigue, the microstructure in the specimen reached a dynamic equilibrium condition for that material and under the given cyclic loading. Corresponding to the stable stage of fatigue, the magnetic properties, such as remanence and coercivity also showed a stabilization. With the increase in number of fatigue cycles, the formation and development of slip-bands at the surface of specimen lead to the nucleation of fatigue cracks. The final propagation of a fatigue crack significantly altered both mechanical properties and magnetic properties of

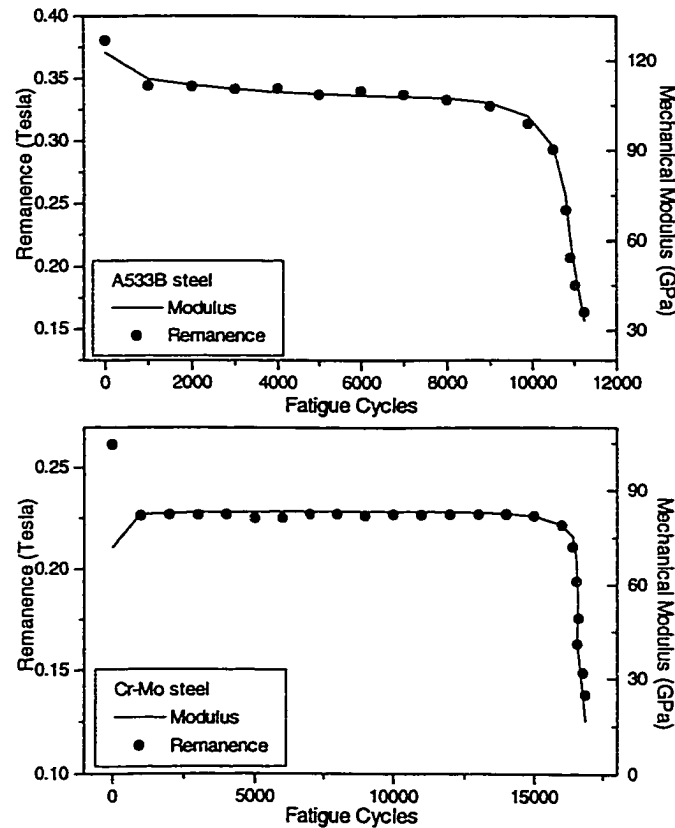


Figure 2 The effect of strain-controlled fatigue on remanence in samples of A533B steel and Cr-Mo steel.

the fatigue specimen. The growing crack reduced the actual area bearing the applied load, therefore, the mechanical modulus of the fatigue specimens showed a decrease. On the other hand, the fatigue crack provides a discontinuous interface to magnetic flux. The increased reluctance resulted in an increase in leakage flux near the fatigue crack, the measured coercivity, which is the measured magnetic field when the magnetic flux density in the magnetic circuit is zero, increased after the propagation of the fatigue crack. However, the increase in coercivity was found to be dependent on crack position. When the Hall probe, magnetic field sensor, was not close to the crack, less variation in coercivity was observed.

On the other hand, the remanence was found to decrease with the propagation of fatigue crack and was crack position independent. The propagating crack reduced the cross section area of the magnetic circuit and reduced the maximum magnetic flux in the magnetic circuit, therefore, the measured remanence decreased with the propagation of fatigue crack.

#### RELATIONSHIP BETWEEN MECHANICAL MODULUS AND REMANENCE

Since the presence of a fatigue crack altered both mechanical properties and magnetic properties of the fatigue specimen and the measured remanence followed closely the mechanical modulus, a monotonic relationship was expected between the mechanical modulus and the magnetic remanence after the propagation of the fatigue crack. From the viewpoint of nondestructive evaluation of fatigue damage, the relationship is very useful. In this study, an approximately linear relationship between mechanical modulus and magnetic remanence was observed.

The magnetic circuit can be modeled as shown in Figure 3. After the propagation of a fatigue crack, the increase of leakage field around the fatigue crack results in an increase in measured coercivity, but the leakage flux is very small compared with the flux in the sample. If the flux leakage is ignored for remanence measurement, the flux is the same at any cross section in the specimen. When magnetic hysteresis measurements were made, the specimens were magnetized to saturation. Due to the smaller cross-sectional area, the remaining area has higher flux density and is magnetized to saturation first. After removing the external magnetic field, the remanent magnetic flux on the remaining area ( $B_r \propto S_R$ ) is equal to the flux on any other cross-section of the specimen.

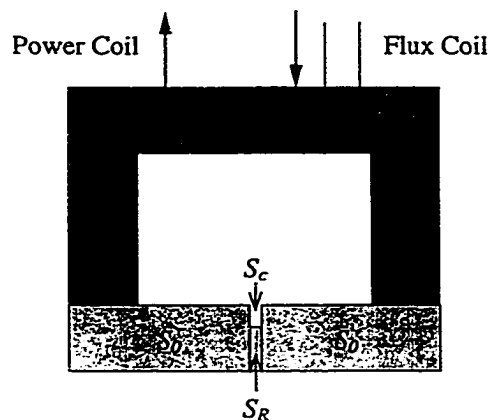


Figure 3 The model of the magnetic measurement.

$$\Phi_0 = B_{r0}S_R = \Phi' \tag{1}$$

According to the configuration of the surface sensor used in this study, the measured remanence actually was the measured magnetic flux in that magnetic circuit when applied magnetic field is zero divided by the original area  $S_0$  of the specimen. The measured remanence  $B_{rm}$  therefore is:

$$B_{rm} = \frac{\Phi_0}{S_0} = \frac{B_{r0}S_R}{S_0} = \frac{S_0 - S_c}{S_0} B_{r0} \tag{2}$$

The “mechanical modulus” was the measured load divided by the product of the original cross-sectional area and the applied strain. Due to the propagation of the fatigue crack, the area bearing the applied load actually decreased and this led to a decrease in the apparent modulus. Assuming that the modulus on the remaining area remained constant during fatigue crack propagation. The measured mechanical modulus  $Y_m$  is:

$$Y_m = \frac{L}{S_0 \epsilon} = \frac{Y_0 S_R \epsilon}{S_0 \epsilon} = \frac{S_R}{S_0} Y_0 = \frac{S_0 - S_c}{S_0} Y_0 \tag{3}$$

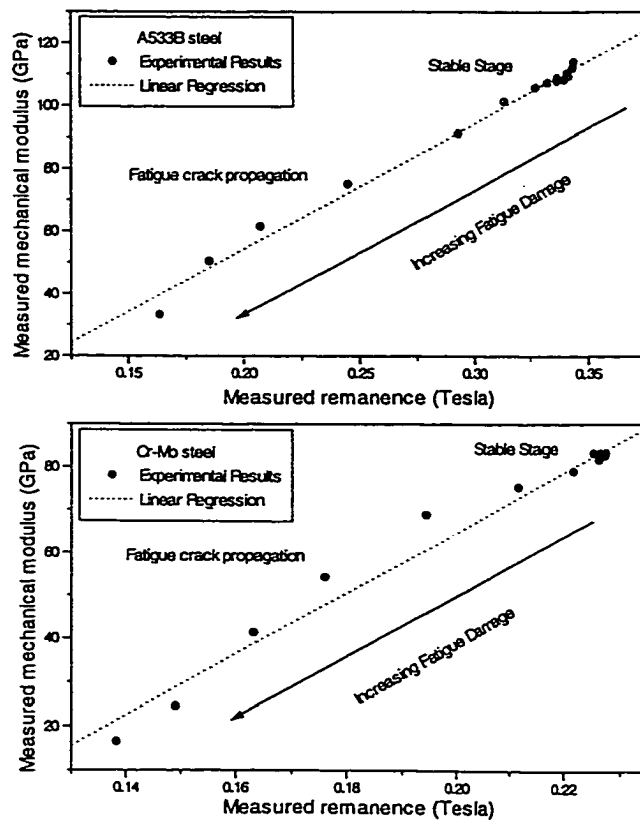


Figure 4 The linear relationship during fatigue crack propagation in strain-controlled fatigue on A533B steel and Cr-Mo steel.

Both mechanical modulus and magnetic remanence are proportional to the remaining area after the propagation of fatigue crack, and this therefore leads to a linear relationship between them:

$$Y_m = \frac{Y_0}{B_{r0}} B_{rm} \quad (4)$$

The above linear relationship between mechanical modulus and magnetic remanence was observed in this study on both A533B steel and Cr-Mo steel as shown in Figure 4. The deviation from the straight line is believed to be due to the fact that high stress concentration causes the change in the magnetic properties on the remaining area.

The left hand side of the model equation is modulus, the change in mechanical response of specimen resulted from fatigue damage. The right hand side of the model equation is a measurable magnetic property, remanence. Therefore, by using the above model equation, the fatigue damage of a material can be evaluated nondestructively through magnetic remanence measurement.

## CONCLUSIONS

Magnetic properties are sensitive to both microstructural changes induced by fatigue cycling and inhomogeneities due to fatigue cracks. Magnetic properties, such as coercivity and remanence, were found to change systematically with fatigue damage. Towards the end of fatigue lifetime, significant variations in measured magnetic properties were observed. An approximately linear relationship between mechanical modulus and magnetic remanence was observed. A model equation developed in this study also shows the linear relationship. The progress of fatigue damage can therefore be evaluated nondestructively using magnetic techniques, specifically using remanence measurement.

## ACKNOWLEDGMENTS

This work was sponsored by the US Nuclear Regulatory Commission under grant number of NRC-04-94-092 through the Center for NDE at Iowa State University.

## REFERENCES

1. W.J. Harris, *Engineering Design Guides*, 14 (Design Council, Oxford University Press, 1976).
2. D.C. Jiles, *NDT International*, 21, pp.311, 1988.
3. M.S.C. Bose, *NDT International*, 19(2), pp. 83, 1986.
4. M.B. Shaw and M.S.C. Bose, *Phys. Stat. Sol(a)*, 86, pp.275, 1984.
5. M.K. Devine, D.C.Jiles, and S. Hariharan, *Journal of Magnetism and Magnetic Materials*, 104, pp.377, 1992.
6. M.K. Devine, D.A. Kaminski, L.B. Sipahi and D.C. Jiles, *Journal of Materials Engineering and Performance*, 1(2), pp.249, 1992.
7. M.R. Govindaraju, A. Storm, D.C. Jiles and S.B. Biner, *Review of Progress in Quantitative NDE*, 12, pp.1893, 1993.
8. Z.J. Chen, D.C.Jiles, and J.Kameda, *Journal of Applied Physics*, 75(10), pp. 6975, 1994.

**MAGNETIC NONDESTRUCTIVE EVALUATION  
OF NUCLEAR PRESSURE VESSEL STEELS FOR FATIGUE DAMAGE**

Y. Bi, M. R. Govindaraju, S. B. Biner and D. C. Jiles  
Center for NDE, Iowa State University, Ames, IA 50011

Abstract

Fatigue damage in steel structural components affects their magnetic properties. In this study, a series of strain-controlled low cycle fatigue tests were conducted on samples prepared from A533B nuclear reactor pressure vessel steel. Magnetic hysteresis and Barkhausen measurements were made at predetermined intervals of fatigue life under zero strain, fixed compressive and tensile load conditions. The results indicate that magnetic hysteresis parameters, such as remanence, and Barkhausen signals show significant changes as the material approaches the end of its fatigue life.

Introduction

The integrity of critical components of power plants, such as pressure vessels which are exposed to severe operating stresses during their lifetime, is an area of prime concern at this time because of failure induced by cyclic loading. In nuclear pressure vessel systems, for example, cyclic stresses are induced by thermal expansion of the components resulting in low-cycle fatigue conditions. In order to ensure safe operation of these pressure vessels it is desirable to develop nondestructive evaluation techniques which can monitor the progress of fatigue damage.

The present investigation is a part of an on-going research program to study the change in magnetic properties as a result of fatigue damage in A533B steels, which are widely used as a structural material for nuclear pressure vessels. In previous work [1], it was shown that it is possible to detect the onset of fatigue failure in steels by measuring changes in the magnetic properties, such as Barkhausen emissions, coercivity and remanence.

As the magnetic hysteresis parameters and magnetic Barkhausen emissions are strongly influenced by the magnitude and the direction of the applied stress, the objective of the present study was to elucidate the effects of the stress-state on the magnetic signature of the fatigue damaged material. In this study, therefore, during the strain-control fatigue experiments, the magnetic measurements were made not only under zero strain conditions but also at constant tensile and compressive loads. The variations in magnetic properties during fatigue were measured by the Magnescope [2] and the Magneprobe [3]. The Magnescope measures the magnetic hysteresis parameters while the Magneprobe detects the Barkhausen signals which are the discontinuous changes of magnetization at the surface of the material under a varying applied magnetic field. Both of these instruments use specially designed surface sensors, or inspection heads, so that the magnetic properties of specimens can be measured in-situ.

Background

It is well known that fatigue failure is a cumulative process involving dislocation motion and redistribution, microcrack initiation and propagation [4]. The magnetic properties of ferromagnetic materials are very sensitive to these microstructural changes [5,6]. The characteristics of the magnetic parameters also depends on the composition and structure of the material, microstructural characteristics such as grain size, amount and distribution of inclusions, precipitates and the presence of residual stresses. It has been shown that the dislocations generated and the microcracks initiated during fatigue act as pinning sites which impede the motion of magnetic domain walls under the applied magnetic field, thereby influencing the bulk magnetic properties, such as coercivity and

remanence. At the end of the fatigue lifetime, the fatigue cracks, which impede magnetic flux and change the distribution of magnetic field, play a major role in determining the measured magnetic properties. Hence it is possible to develop an NDE technique based on magnetic property measurements for in-situ monitoring of fatigue damage in material.

The variations in magnetic hysteresis properties with the fatigue process were reported earlier by Bose [7], Shaw and Bose [8]. Devine et al. [9, 10] studied the effects of cyclic stress on the magnetic hysteresis parameters of polycrystalline iron and detection of fatigue in structural steels by the magnetic property measurements. Govindaraju et al. [11] found significant magnetic property changes at the end of low-cycle fatigue when magnetic measurements were made under zero load condition. Chen et al. [12] found a simple logarithmic relationship between the coercivity and the number of stress cycles under low-cycle, load-controlled fatigue conditions, which could be used to determine the condition of the material or its proximity to fatigue failure.

Barkhausen effect is the small discontinuous change in magnetic induction, which results in induced voltage in pick-up coil nearby, under varying magnetic field. They are attributed to the sudden irreversible motion of domain walls when they break away from pinning sites under the action of changing magnetic field. These pinning sites could be grain boundaries, dislocations, precipitates, inclusions, microcracks and other inhomogeneities.

It has been shown that Barkhausen emissions possess characteristics highly sensitive to the surface stresses and structure of a material [13]. Donzella and Granzotto recently reported some experimental results about the correlation between Barkhausen emissions and the fatigue life of steel specimens [14]. In earlier studies, Karjalainen and Moilanen [15, 16] have used the Barkhausen measurements to monitor progress of fatigue in steel.

Barkhausen emissions which have typical frequency ranges from 20-300 KHz, have a short penetration depth in steels. This means that the Barkhausen emissions give information only about the surface layer, which makes Barkhausen measurements suitable for determination of the formation of extrusions and intrusions due to slip at which fatigue crack nucleation takes place during the cyclic deformation. On the other hand, magnetic hysteresis measurements, which are performed under a

quasi-DC magnetic field, allowing deeper penetration, can give information of microstructure in the bulk of the material. The combination of these two measurements should result in improved in-situ monitoring of fatigue damage.

### Materials

The material involved in this study was ASTM A533B steel, which is widely used in nuclear pressure vessel systems. The chemical composition of the A533B steel is shown in Table I:

Table I. Chemical composition ( in weight percentage) of the A533B steel used in the study.

Fe	Mn	Ni	Mo	Cr	Si	C
Bal.	1.45	0.56	0.50	0.06	0.22	0.223

Two groups of fatigue specimens were machined from the A533B steel provided by Oak Ridge National Laboratory. One group, identified as Group A, was machined along the rolling direction of bulk material and had a yield strength of 442 MPa. Another group, identified as Group B, was machined perpendicular to the rolling direction and had a yield strength of 407 MPa.

### Experimental procedure

Initial magnetic measurements were taken on each fatigue sample machined from the A533B steel using the Magnescope and the Magneprobe before being subjected to fatigue cycling. Measurements taken using the Magnescope involved acquiring a single hysteresis loop and calculating the magnetic parameters such as coercivity, remanence and hysteresis loss. The Barkhausen signals measured using the Magneprobe were in terms of  $V_{rms}$  (root mean square voltage).  $V_{rms}$  is related to both the strength of the pinning sites and their resistance to domain wall movement and the number density of the pinning sites [3].

The fatigue tests were conducted on a computer controlled, 100KN, servo hydraulic MTS 880 system in strain-control mode. The fatigue specimens were subjected to low-cycle tension-compression fatigue at a constant strain amplitude of 0.003 at a frequency of 2 Hz. At pre-determined intervals of 1000 cycles, the fatigue cycling was halted in the zero-strain condition and the magnetic measurements were taken. Then, the load on the MTS system was

adjusted so that the stress on the fatigue specimen was +158MPa in tension and -158MPa compression, respectively. The magnetic measurements were taken again at each condition. At the end of fatigue life, the interval between measurements was reduced so that the rapid changes in magnetic properties which occurred during the final stage of fatigue life could be observed. The fatigue cycling was stopped when the load amplitude needed to attain the 0.003 strain decreased below 30% of the load amplitude of the first 5 cycles.

### Results and Discussion

#### Magnetic Imaging of as-received material

The point-to-point distribution in the magnetic hysteresis parameters of the "as received" material was determined and the variation in coercivity is shown in Figure 1. This shows the areas where the coercivity values were high thereby identifying the stress concentration regions. These plots will be useful in characterizing the material and locating areas which have high concentration of localized defects, such as high dislocation density and residual

stresses. In figure 1, the high coercivity regions can be associated with stresses generated during the cutting process.

#### Initial Magnetic Measurements

The initial magnetic measurements listed in Table II showed no significant difference in magnetic hysteresis parameters between specimens of Group A and Group B which were cut from the same A533B steel block. The Barkhausen emissions as expressed by the root-mean-square voltage  $V_{rms}$ , which are sensitive to the microstructures and represent an average value at the surface of the material, also showed no significant difference.

However, samples from group A had a longer average fatigue lifetime, about 17,000 cycles compared to those from group B which had about 13,000 cycles. This difference in fatigue life may be attributed to grain orientation with respect to the applied stress direction.

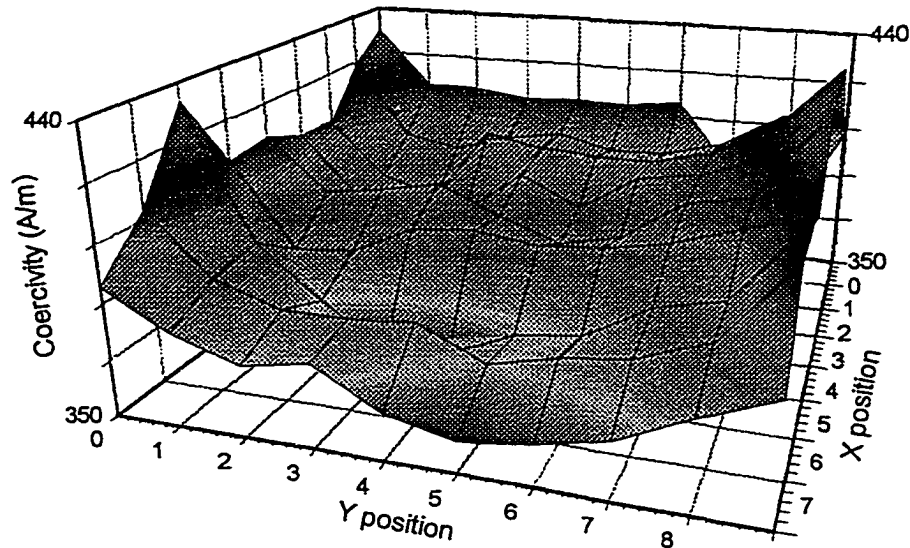


Figure 1. The variation of coercivity on the surface of as received material

Table II. Average baseline values of magnetic properties and corresponding average fatigue life time of as-received samples of A533B steel.

Samples	Coercivity (A/m)	Remanence (Tesla)	Hysteresis Loss (Joule/m <sup>3</sup> )	$V_{rms}$ (Volts)	Fatigue Lifetime (Cycles)
Group A	607	0.36	1095	0.221	16500
Group B	577	0.37	1040	0.222	13200

### Magnetic measurements on fatigue specimens

The magnetic measurements taken during fatigue showed that there were significant changes in magnetic properties, such as coercivity, remanence, hysteresis loss and Barkhausen signal emissions, both at the beginning and the end of fatigue life. Among all the parameters measured, remanence and Barkhausen signals were found to be very sensitive to the microstructural changes caused by fatigue. The variation of remanence with number of fatigue cycles is shown in Figure 2 and the variation of the Barkhausen signals with number of fatigue cycles on the same specimen is shown in Figure 3.

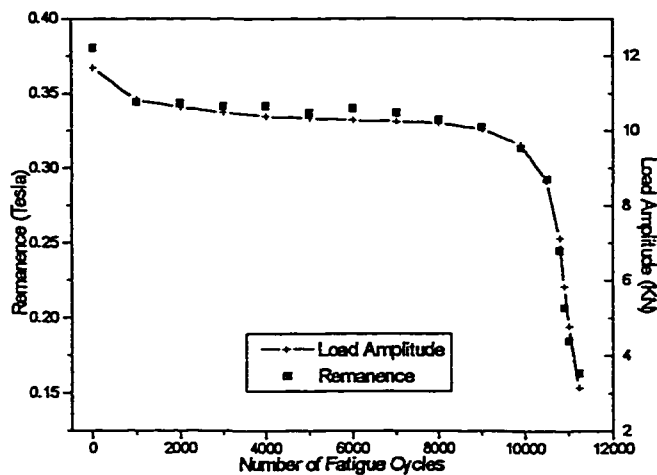


Figure 2. The effect of fatigue on remanence of group B sample (B5) of A533B Steel.

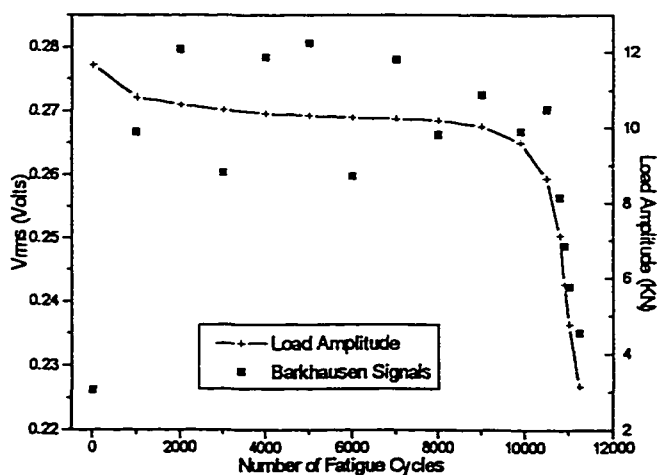


Figure 3. The effect of fatigue on Barkhausen signals of group B sample (B5) of A533B Steel.

The profile of load amplitude required to attain the predetermined strain amplitude, which is also shown in Figure 2, indicated a decrease in load amplitude in the initial stage of fatigue, followed by a stabilization of this load amplitude during the second stage, and finally a drop in the load amplitude during the third stage of fatigue. These data are a typical representative of the behavior of all samples tested. The decrease in the load amplitude in the initial stage of fatigue is caused by fatigue softening. The magnetic hysteresis results also showed an initial decrease in remanence as shown in Figure 2 and a variation in the Barkhausen signal  $V_{rms}$ , as shown in Figure 3. At the beginning of cyclic stress, the pre-existing dislocations in grains migrate initially to the grain boundaries and precipitates, leaving a larger dislocation-free area in the grains. Lower dislocation density results in a longer sweeping distance for domain wall motion, and hence larger Barkhausen emission.

During the second stage of fatigue, corresponding to the stabilization of the load amplitude, the measured remanence also showed stabilization.

The last stage of fatigue before final failure is characterized by the propagation of fatigue cracks. The propagating crack played a major role in affecting mechanical properties as well as the magnetic properties. As the fatigue cracks grows, the load bearing cross sectional area of the specimen decreases, and therefore the load needed to reach the predetermined strain amplitude decreased. At the same time, the fatigue crack impedes the magnetic flux, causing demagnetization effects, so that the measured remanence and the Barkhausen signals decreased in the final stage of fatigue.

The results obtained from the study indicated that at the end of fatigue life, the measured remanence decreased by more than 25% from its initial value. At the same time the Barkhausen signals also showed a decrease of about 10%. Considering that the remanence decreased with crack growth and propagation, it is proposed that the remanence can be used to monitor the progress of fatigue damage in steel components.

Since the remanence very closely followed the behavior of the load amplitude during the fatigue test, as shown in Figure 3, the load amplitude is plotted against remanence in Figure 4. This result might indicate that during low-cycle strain-controlled fatigue process, the microstructural variations associated with fatigue crack initiation and



propagation affects the relationship between strain and load amplitude (mechanical property) and remanence (magnetic property) in a similar way.

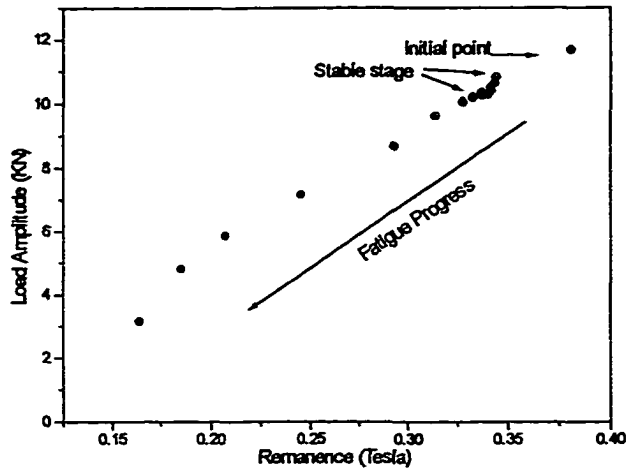


Figure 4. The correlation between the load amplitude and remanence

#### Effect of applied stress

Stress affects dislocation density in materials, hence, the measured magnetic properties of steels. There is evidence that certain magnetic hysteresis parameters are strongly influenced by the magnitude and the direction of the applied and residual stresses. In order to distinguish the variation in the magnetic properties due to the fatigue damage from variations due to applied or residual stresses, another series of fatigue experiments were conducted. During these experiments, magnetic measurements were taken not only at zero strain condition but also at fixed tensile and compressive stresses. The variation of remanence with the number of fatigue cycles under different stress types, viz., compressive and tensile, is shown in Figure 5.

It can be seen from Fig. 5 that remanence is influenced significantly by the type of applied stress. The application of compressive stress decreased the measured remanence value. The remanence measured under 158 MPa tensile stress was very close to measured under zero strain condition. This effect is simply due to the similarity in conditions under "zero strain" and 158MPa tensile stress. Because in order to make the system reach zero strain condition after several cycles, the system had to exert about 133 MPa tensile stress on the sample. This result of the study indicates that "in service stress" affects the measured magnetic properties during fatigue, but fatigue

damage can still be detected and separated from the effects of stress by magnetic measurements, provided magnetic measurements are made under the same stress levels.

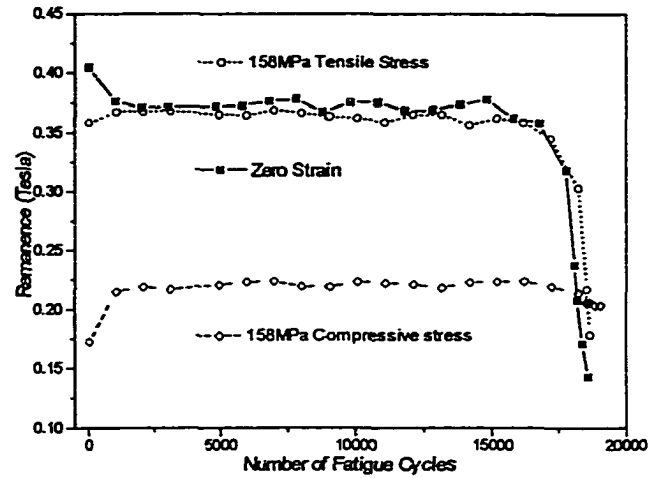


Figure 5. Stress effect on measured remanence of group A sample.

#### Conclusions

The present investigation involved conducting a series of strain-controlled low cycle fatigue tests on samples prepared from A533B nuclear reactor pressure vessel steels. The results indicate that the variations in magnetic properties, especially the remanence and Barkhausen signal amplitude are sensitive to the microstructural changes, such as fatigue crack initiation, growth and propagation that occur during the fatigue process. The results also indicate that "in service stress" affects the measured magnetic properties during fatigue, however, the change in magnetic properties due to fatigue still can be detected and could be separated from those due to effects of stress. The "magnetic imaging" of the components, which involves measuring the magnetic hysteresis parameters on the surface of the materials in a grid pattern and plotting them on 3-D plots or color graphics can identify regions of localized defects. This technique could be used to isolate regions of highly stressed or defective areas in the component.

### References

1. M.R. Govindaraju et al., "SEM analysis of fatigue induced microstructural changes and the resulting effect on magnetic properties of structural steels", Non-Destructive Evaluation and Materials Properties II, eds., P.K. Liaw, O. Buck, R. J. Arsenault and R.E. Green, Jr, TMS, (1994), 133-144.
2. A.R. Eichman et al., "New procedures for in situ measurement of the magnetic properties of materials; applications of the Magnescope", IEEE Trans. Mag. 28, (5), (1992), 2462.
3. A.P. Parakka, and D.C. Jiles, "Magneprobe: a portable system for detection and characterization of Barkhausen signals for nondestructive testing of ferromagnet material", Journal of Magnetism and Magnetic Materials, (1841), (1995), 140-144.
4. W.J. Harris, "The significance of fatigue", Engineering Design Guides, 14 (Design Council, Oxford University Press, 1976).
5. D.C. Jiles, "Review of magnetic methods for NDE", NDT International, 21 (1988), 311.
6. D.C. Jiles and D.L. Atherton, "Theory of Ferromagnetic Hysteresis", Journal of Magnetism and Magnetic Materials, 61, (1986), 48.
7. M.S.C. Bose, "A study of fatigue in ferromagnetic materials using magnetic hysteresis technique", NDT International, 19, (2), (1986), 83.
8. M.B. Shaw and M.S.C. Bose, "Magnetic NDT technique to evaluate fatigue damage", Phys. Stat. Sol(a), 86 (1984), 275.
9. M.K. Devine, D.C. Jiles, and S. Hariharan, "Effects of cyclic stress on the magnetic hysteresis parameters of polycrystalline iron" Journal of Magnetism and Magnetic Materials, 104, (1992), 377.
10. M.K. Devine et al., "Detection of fatigue in structure steels by magnetic properties measurements" Journal of Materials Engineering and Performance, 1(2), (1992), 249-254.
11. M.R. Govindaraju et al., "Evaluation of low cycle fatigue damage in steel structural components by a magnetic measurement technique", Review of Progress in Quantitative NDE, 12, (1993), 1893-1846.
12. Z.J. Chen, D.C. Jiles, and J. Kameda, "Estimation of fatigue exposure from magnetic coercivity", J. appl. Phys., 75(10), (1994).
13. K. Schröder, "Magnetic Barkhausen effect and its application", Nondestructive Test. Eval., 5 (1989), 3.
14. G. Donzella and S. Granzotto, "Some experimental results about the correlation between Barkhausen noise and the fatigue life of steel specimens", Journal of Magnetism and Magnetic Materials, 133 (1994), 613.
15. L.P. Karjalainen and M. Molianen, "Detection of plastic deformation during fatigue of mild steel by the measurement of Barkhausen noise", NDT International (1979), 51.
16. L.P. Karjalainen and M. Molianen, "Fatigue softening and hardening in mild steel detected from Barkhausen noise", IEEE Trans. on Magnetics, MAG-16, 3, (1980), 514.

### Acknowledgments

This research is supported by the US Nuclear Regulatory Commission under grant number of NRC-04-94-092 through the Center for NDE, Iowa State University, Ames, Iowa.

**REFERENCES**

- [1] D. C. Jiles, *Introduction to Magnetism and Magnetic Materials*, Chapman & Hall, London, 1991.
- [2] S. Chikazumi, *Physics of Magnetism*, Wiley, New York, 1964.
- [3] J.A. Ewing, *Magnetic Induction in Iron and other Metals*, 3rd edn., The Electrician Publishing Co., London, 1900, and *Proc. Roy. Soc.*, Vol. 33, p. 21, 1881.
- [4] E. Warbug, *Ann. Physik*, Vol. 13, p. 141, 1881.
- [5] G. Wiedemann, *Phil. Mag.* Vol. 1, p. 52, 1886.
- [6] J.C. Maxwell, *Electricity and Magnetism*, Oxford, Univ. Press, Oxford, 1873.
- [7] J. A. Ewing, *Phil. Mag.* Vol. 5, p. 205, 1890.
- [8] H. J. Williams, *Phys. Rev.* Vol. 52, p. 747, 1937.
- [9] L. Rayleigh, *Phil. Mag.*, Vol. 23, p. 225, 1887.
- [10] J.R. Brauer, *IEEE Transaction on Magnetics*, Vol. 11, p. 81, 1975.
- [11] J. Fischer and H. Moser, *Archiv. für Electrotechnik*, Vol. 42, p. 286, 1956.
- [12] F. C. Trutt, *IEEE Trans. Power App. Sys.* PAS-87, p. 665, 1968.
- [13] G.F.T. Widger, *Proc. Inst. Elect. Engg.*, Vol. 116, p. 156, 1969.
- [14] J. Rivas, *IEEE Transaction on Magnetics*, Vol. 17, p. 1498, 1981.
- [15] F. Preisach, *Zeit. für Physik*, Vol. 94, p. 277, 1935.
- [16] L. Néel, *J. de Phys. Rad.*, Vol. 11, p. 49, 1950.
- [17] L. Néel, *Advan. Phys.*, Vol. 4, p. 191, 1955.
- [18] D.H. Everett, W.I. Whitton, *Trans. Faraday Soc.*, Vol. 48, p. 749, 1952.
- [19] D.H. Everett, *Trans. Faraday Soc.*, Vol. 50, p. 1077, 1954.
- [20] D.H. Everett, *Trans. Faraday Soc.* Vol. 51, p. 1551, 1955.

- [21] I.D. Mayergoyz, *Mathematical Models of Hysteresis*, Springer-Verlag, New York, 1991.
- [22] A. Globus, *Comptes Rendus, Acad. Seances*, Vol. 255, p. 1709, 1962.
- [23] A. Globus and P. Duplex, *Phys. Stat. Sol.*, Vol. 31, p. 765, 1969.
- [24] D. C. Jiles and D. L. Atherton, *IEEE Transaction on Magnetics*, Vol. 19, p. 2183, 1983.
- [25] D. C. Jiles and D. L. Atherton, *Journal of Applied Physics*, Vol. 55, p. 2115, 1984.
- [26] D. C. Jiles and D. L. Atherton, *Journal of Magnetism and Magnetic Materials*, Vol. 61, p. 48, 1986.
- [27] D.C. Jiles and J.B. Thielke, *IEEE Transaction on Magnetics*, Vol. 25, p. 3928, 1989.
- [28] D.C. Jiles, J.B. Thielke and M.K. Devere, *IEEE Transaction on Magnetics*, Vol. 28, p. 27, 1992.
- [29] D.C. Jiles, *IEEE Transaction on Magnetics*, Vol. 29, p. 3490, 1993.
- [30] D.C. Jiles, *IEEE Transaction on Magnetics*, Vol. 30, p. 4326, 1994.
- [31] D.C. Jiles, *Journal of Applied Physics*, Vol. 76, p. 5849, 1994.
- [32] A. Ramesh, D.C. Jiles and J. Roderick, *IEEE Transaction on Magnetics*, Vol. 32, p. 4234, 1996.
- [33] A. Ramesh, D. C. Jiles and Y. Bi, *Journal of Applied Physics*, Vol. 81, p. 5585, 1997.
- [34] M.J. Sablik, H. Kwun, G.L. Burkhardt and D.C. Jiles, *Journal of Applied Physics*, Vol. 61, p. 3799, 1987.
- [35] M.J. Sablik, G.L. Burkhardt, H. Kwun and D.C. Jiles, *Journal of Applied Physics*, Vol. 63, p. 3930, 1988.
- [36] M.J. Sablik, S.W. Rubin, L.A. Riley, D.C. Jiles, D.A. Kaminski and S.B. Biner, *Journal of Applied Physics*, Vol. 74, p. 480, 1993.
- [37] R.L. Brandt, United States Patent, 553487, 1996.

- [38] I.B. Goldberg, J.H. Hanamoto, C.S. Hollingswirth and T.M. McKinney, United States Patent, 5450052, 1995.
- [39] R.W. Chantrell, A. Hoare, D. Melville, H.J. Lutke-Stetzkamp and S. Methfessel, *IEEE Transaction on Magnetics*, Vol. 25, p. 4216, 1989.
- [40] A. Aharoni, E.H. Frei, S. Shtrikman and D. Treves, *Bull. Res. Counc. Israel*, Vol. 6A, p.215, 1957.
- [41] E.C.Stoner and E.P.Wohlfarth, *Proc. Roy. Soc.*, Vol. 240, p. 599, 1948.
- [42] K. Elk and R. Hermann, *Journal of Magnetism and Magnetic Materials*, Vol. 117, p. 359, 1992.
- [43] K.Elk, *Journal of Magnetism and Magnetic Materials*, Vol. 157, p. 369, 1996.
- [44] K. Elk, *Phys. Stat. Sol. (b)*, Vol. 171, K103, 1992.
- [45] K.H. Schmodt and H. Huneus, *Techn. Messen*, Vol. 48, p. 375, 1981.
- [46] D.C. Jiles, *Journal of Physics, D: Applied Physics*, Vol. 28, p. 1537, 1995.
- [47] P. Langevin, *Annales de Chem. et. Phys.*, Vol. 5, p.70, 1905.
- [48] D.L. Atherton and M. Schonbachler, *IEEE Transaction on Magnetics*, Vol. 24, No. 1, p. 616, 1988.
- [49] D.C. Jiles and A.P.Parakka, "Ferrite substrates for miniaturization of power electronics", Interim report for Rockwell Collins, Avionics and Communication Division, 1996.
- [50] K. Preis, I. Bardi, O. Biro, C. Magele, W. Renhart, K.R. Richter and G. Vrisk, *IEEE Transaction on Magnetics*, Vol.27, No. 5, p.3798, 1991.
- [51] M. Gyimesi and J.D. Lavers, *IEEE Transaction on Magnetics*, Vol. 28, No. 4, p. 1924, 1992.
- [52] B.D. Cullity, *Introduction to Magnetic Materials*, Addison-Wessley, p. 100, 1972.

## VITA

NAME OF AUTHOR: Ying Bi

DATE AND PLACE OF BIRTH: October 1, 1960, Nanjing, China

### DEGREES AWARDED:

B.S. in Physics, Nanjing Normal University, China, 1982.

M.S. in Electrical Engineering, Institute of Electronics, The Academy of Science of China, 1988.

M.S. in Electrical Engineering, Iowa State University, 1997.

### HONORS AND AWARDS:

Tau Beta Pi, National Engineering Honor Society, 1996.

Sigma Xi, National Scientific Research Honor Society, full member, 1998.

Research Excellence Award, Iowa State University, 1997.

Student Travel Fellowship, 7th Joint MMM-Intermag Conference, Magnetics Society of the IEEE, 1998.

### PROFESSIONAL EXPERIENCE:

Research Assistant, Ames Laboratory and Center for Nondestructive Evaluation, Iowa State University, 1995-1998.

Teaching Assistant, Department of Electrical and Computer Engineering, Iowa State University, 1994-1995.

Lecturer and Lab Instructor, Physics Department, Nanjing Normal University, China, 1988-1994

### PROFESSIONAL PUBLICATIONS:

- [1] Y. Bi and D.C. Jiles, "Dependence of Magnetic Properties on Crack Size in Steels", *IEEE Transactions on Magnetics*, Vol. 34, p. 2021, 1998.
- [2] M. Pasquale, V. Basso, G. Bertotti, D.C. Jiles and Y. Bi, "Domain Wall Motion in Random Potential and Hysteresis Modeling", *Journal of Applied Physics*, Vol. 83, p. 6497, 1998.
- [3] Y. Bi, M. R. Govindaraju and D.C. Jiles, "The Dependence of Magnetic Properties on Fatigue in A533B Nuclear Pressure Vessel Steels", *IEEE Transactions on Magnetics*, Vol. 33, p. 3928, 1997.
- [4] Y. Bi and D.C. Jiles, "Detection of Fatigue Crack propagation in Steel using Magnetic Measurements", *Review of Progress in Quantitative NDE*, Vol. 17, p. 1509, 1997.
- [5] A. Ramesh, D. C. Jiles and Y. Bi, "Generalization of Hysteresis Modeling to Anisotropic Materials", *Journal of Applied Physics*, Vol. 81, p. 5585, 1997.
- [6] D. C. Jiles, Y. Bi and S. B. Biner, "Development of the Magnescope as an instrument for in situ evaluation of steel components of nuclear systems", Final contract report, Nuclear Regulatory Commission, grant number NRC-04-94-092, NUREG/CR-6557, February 1997.
- [7] Y. Bi, M. R. Govindaraju, S. B. Biner and D. C. Jiles "Magnetic Nondestructive Evaluation of Nuclear Pressure Vessel Steels for Fatigue Damage", *Non-Destructive Evaluation and Materials Properties III*, eds., P.K. Liaw, O. Buck, R. J. Arsenault and R.E. Green, Jr, TMS, p. 115, 1996.
- [8] M. J. Sablik, S. W. Rubin, D. C. Jiles, D. Kaminski and Y. Bi, "Finite Element Simulation of Magnetic Detection of Creep Damage at Seam Welds", *IEEE Transactions on Magnetics*, Vol. 52, p. 4290, 1996.